## *Developing Optical Tweezers, Spectroscopy and Microfluidics to Investigate High Volume Consumer Products*

LAWTON, PENELOPE,FLEUR

# Developing Optical Tweezers, Spectroscopy and Microfluidics to Investigate High Volume Consumer Products

**Penelope Fleur Lawton**

A Thesis presented for the degree of
Doctor of Philosophy

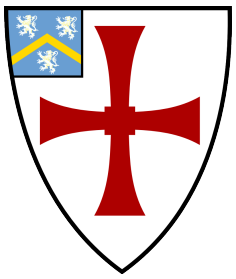

Centre for Advanced Instrumentation
Department of Physics
Durham University
England

January 2015

*Dedicated to*

My wonderful and constantly supportive parents, Christopher and Hilary Lawton

# Developing Optical Tweezers, Spectroscopy and Microfluidics to Investigate High Volume Consumer Products

**Penelope Lawton**

Submitted for the degree of Doctor of Philosophy
January 2015

## Abstract

As the use of consumer products grows, quality control becomes a more and more important aspect. In this thesis, three different high volume consumer products are investigated through the use of optical instrumentation; these are hair dye, dishwasher detergent and clothes detergent. A bespoke Raman tweezer system was built around microfluidic channels to investigate the reactions which occur in a dishwasher via flowing solutions past a trapped species made from acrylic, a common problem item in dishwashers. It was found that it is possible to predict some of the reaction processes via this method, although the particle build-up can lead to some instabilities in the system. An absorbance spectrometer system was also built around microfluidic channels to investigate the reactions which develop the colour of hair dye, to advance a current method by Proctor and Gamble. Another spectrometer system built to study the reflection and transmission of light by stained fabric was developed to quantify the performance of fabric detergents.

# Declaration

The work in this thesis is based on research carried out at the Centre for Advanced Instrumentation, University of Durham, England. No part of this thesis has been submitted elsewhere for any other degree or qualification and it is all my own work unless referenced to the contrary in the text.

**Conference publications:**

"Combining optical trapping in a microfluidic channel with simultaneous micro-Raman spectroscopy and motion detection", P. F. Lawton ; C. D. Saunter and J. M. Girkin, Proc. SPIE 8976, Microfluidics, BioMEMS, and Medical Microsystems XII, 89760V (March 6, 2014)

**In preparation:**

"Towards a high throughput microfluidic system for monitoring the reactions in hair dye via absorbance spectroscopy"

"Monitoring the reactions in a dishwasher via optical tweezers Raman spectroscopy and motion detection"

# Acknowledgements

First and foremost, thanks must of course go to my supervisor, John Girkin, for his guidance, insight, support and endless patience. Through his connections and expertise, I have had the opportunity to work on several projects during my PhD, and I am extremely grateful for having had the chance to gain this unique insight into finding practical solutions to real life problems. I look forward to continuing to work with John during the next two years. Thanks must also go to my secondary supervisor Gordon Love who referred me to this project, and to Paul Clark for all his help, not to mention perhaps being the only reason I haven't electrocuted myself in the past three years! I would also like to thank Chris Saunter for always being on hand to assist with his encyclopaedic knowledge of Python, and for his encouragement.

I would like to thank my various officemates over the years from room 127 and everyone in CfAI, for their encouragement, support, and preventing me from going insane by forcing me out of the lab on more than one occasion. I consider myself incredibly fortunate to have worked in a department with such intelligent, friendly and fun individuals; thank you for all the humour, coffee break discussions and trips to the Vic. I couldn't have done it without you all.

Outside CfAI, I would like to thank my friend Mona Wang; supportive and always kind, she has been an inspiration and a wonderful coffee buddy. Beyond the Department of Physics, I would like to thank Rebecca Allen, who during the ten plus years we have been friends has always supported me through everything I've done; her encouragement and positivity have kept me going in the most difficult

times.

I would also like to thank my colleagues from the P&G Newcastle Innovation centre and the SMC$^3$ team, who have provided insightful monthly seminars on all manner of the detailed chemistry involved in washing and cleaning, and have certainly given me more insight into what goes into my laundry detergent. In particular I would like to thank fellow PhD student Yuexian Hong, who has been endlessly patient with my chemistry questions. I would also like to thank Patrick McCall and Lindsey Godfrey from the P&G hair colour division in Germany for their helpfulness, guidance and support in what has proven to be an exciting collaboration into hair products. I would also like to acknowledge funding from both the UK Government Regional Development Fund, and from P&G Hair Care Products.

And finally I would like to thank my grandparents, June and Harry, for their support and encouragement, and my parents, Chris and Hilary, to whom this thesis is dedicated; I could not have been more lucky to have such supportive and loving parents who have always had faith in me and heroically put up with every grumble, every tearful phone call and every doubt I have had throughout my entire scientific career. Thank you for everything!

# Contents

**Abstract** iii

**Declaration** iv

**Acknowledgements** v

**1 Introduction** 1

**2 Theoretical Considerations for building a miniature dishwasher** 5

2.1 Optical Tweezers . . . . . 5

2.1.1 Theory of optical trapping . . . . . 5

2.1.2 Development and applications of Optical Tweezers . . . . . 10

2.2 Holographic Optical Tweezers . . . . . 11

2.2.1 Modifying the trapping beam through use of an SLM . . . . 11

2.3 Characterising the motion of optically trapped species . . . . . 14

2.3.1 Equipartition . . . . . 14

2.3.2 Monitoring particle position . . . . . 15

2.3.3 Autocorrelation and Power Spectral Analysis . . . . . 15

2.3.4 Stokes Drag . . . . . 18

2.4 Raman Spectroscopy . . . . . 19

2.4.1 An Introduction to Raman Scattering . . . . . 19

2.4.2 Classical and Quantum theories of Raman Scattering . . . . 21

2.4.3 Assigning Raman modes . . . . . 25

2.4.4 Raman Tweezing . . . . . 28

2.5 Surface Deposition . . . . . 30

2.5.1 Dishwasher solutions . . . . . 30
2.5.2 Polymorphs and Crystallization mechanisms of calcium carbonate . . . . . 31
2.6 Microfluidics . . . . . 33
2.6.1 Modelling flow rate in a microfluidic channel . . . . . 34
2.6.2 Pumping and heating in microfluidic channels . . . . . 35

**3 Methodology and Raman Tweezer Instrumentation 38**
3.1 Raman Tweezers . . . . . 38
3.1.1 Basic Tweezer setup . . . . . 38
3.2 Detecting the Raman emission . . . . . 41
3.3 Detecting the high frequency motion changes . . . . . 51
3.4 Flow visualization and dishwasher solutions . . . . . 57

**4 Results and Initial Discussions 64**
4.1 Raman investigations . . . . . 64
4.1.1 Characterising the Raman volume . . . . . 64
4.1.2 Investigating carbonate crystallisation on the channel surface 67
4.1.3 Raman spectroscopy of trapped material in flow . . . . . 68
4.1.4 Raman spectroscopy of the surface of trapped beads in a dishwasher environment . . . . . 73
4.2 Motion tracking in optical tweezers in a changing environment . . . 82
4.2.1 Practicalities of the use of a CMOS camera for tracking a changing bead . . . . . 82
4.2.2 Calibrating the system with distilled water and a simple carbonate formation reaction . . . . . 85
4.2.3 The change in the power spectrum for a simulated dishwasher solution . . . . . 88

**5 A Fast Spectroscopic Method for the Quantification of Laundry Detergent Performance 91**
5.1 Introduction and aims . . . . . 91

5.2 Theory . . . 93
5.3 Methodology and experimental setup . . . 95
5.4 Initial Results . . . 97
5.5 Using PCA to reduce the dimensionality of data . . . 102
5.6 Conclusions and Further Work . . . 106

**6 Towards a High Throughput Microfluidic System for Monitoring the Reactions in Hair Dye 108**
6.1 The Problem . . . 108
6.2 Theory of reaction kinetics and absorbance spectroscopy . . . 109
6.3 Chemistry of Hair Dye . . . 111
6.4 Confocal microscopy . . . 112
6.5 Experimental setup and details . . . 117
6.5.1 Simple replica setup . . . 117
6.5.2 Confocal setup . . . 118
6.5.3 Bubble rejection procedures . . . 121
6.6 Results and Discussions . . . 126
6.6.1 Rate constant calculation for the P&G 'replica' setup . . . 126
6.6.2 Rate constant calculation in the microfluidic channel . . . 128
6.7 Future work . . . 131

**7 Conclusions 133**

**Appendix 144**

**A Equipment specifications 144**
A.1 Spectral response of the LUPA 300 camera sensor . . . 144

# List of Figures

2.1 *Diagrams demonstrating (a) refraction of a Gaussian beam through a dielectric bead causing a strong restoring force $F_{net}$ towards the maximum intensity region of the beam, and (b) full three-dimensional trapping through the use of an objective lens to focus the light beam, creating a force $F_{net}$ which pushes the bead in the direction of beam propagation towards the beam focus (the bead is stably trapped slightly underneath the beam focus)* . . . . . 8

2.2 *Example of the typical optical train for holographic optical tweezers, and an example DOE and the corresponding intensity pattern at the focus* . . . . . 11

2.3 *Schematic (adapted from [1]) of the operation of a reflecting liquid crystal on silicon (LCoS) spatial light modulator. The liquid crystal states are controlled for each pixel through a DVI connection* . . . . 13

2.4 *A theoretical example plot of the power spectrum for species trapped in a strong optical trap (red) and a weak trap (blue)* . . . . . 17

2.5 *An example of the autocorrelation function for a species trapped in a strong optical trap (red) and a weak trap (blue)* . . . . . 18

2.6 *Jablonski diagram depicting the change in the energy of an incident photon on interaction with a molecule in the cases of elastic (Rayleigh) and inelastic (Raman-Stokes and Raman Anti-Stokes) scattering* . . . . . 20

2.7 *Figure adapted from [2] showing the difference between the Raman spectrum of topaz (red) and citrine (purple). Citrine is a natural quartz crystal which is often passed off as topaz, a considerably more expensive gem* . . . . . 21

2.8 *A schematic (adapted from [3]) demonstrating the emission of a photon with energy $\hbar\omega_f$ after the incident photon with energy $\hbar\omega_i$ causes a change of vibrational state from level $E_i$ to $E_f$* . . . . . 23

2.9 *Schematic of the Raman modes of common bonds in organic molecules* 26

2.10 *Schematic of vibrations in carbonates* . . . . . 27

2.11 *An experimentally obtained Raman spectrum of a single calcite crystal, showing the relative strengths of the peaks* . . . . . 28

2.12 *Schematic depicting possible orientations for optical trapping, Raman excitation and Raman detection in Raman tweezer instrumentation* . . . . . 29

2.13 *SEM images of the three polymorphs of calcium carbonate: (a) calcite [4], (b) aragonite [5] and (c) vaterite [6]* . . . . . 32

3.1 *Schematic of the optical trapping and Raman excitation setup. Inset: a close-up of the light paths of each laser through the microscope objective* . . . . . 39

3.2 *Photograph of the experimental setup, depicting: 1. Pipe feed to channel, 2. illumination light being focussed by a 10x microscope objective, 3. the microfluidic channel in a sample holder (providing a liquid-tight connection), 4. the 1.25 NA trapping/Raman objective, 5. Polychroic mirror reflecting 1064 nm and 532 nm light and allowing all other light to pass, 6. Steering mirror for illumination and Raman light, 7. Dichroic mirror passing $>$ 500 nm light to the Raman optics and $<$ 500 nm light to the camera, 8. Tube lens to focus light onto detector and shortpass filters to block residual laser light, 9. Sigma-Koki computer controlled microscope stage for precise stage position control* . . . . . 42

3.3 *The Raman spectrum of toluene flown through the microfluidic channel. Characteristic peaks are present at 521 $cm^{-1}$, 786.5 $cm^{-1}$, 1003.6 $cm^{-1}$, 1211 $cm^{-1}$, 1605 $cm^{-1}$ and 3057 $cm^{-1}$* . . . . . 43

3.4 *Map depicting the intensity of the strong 1086 $cm^{-1}$ carbonate peak at several positions around a sample calcite crystal, using an integration time of 10 seconds. The intensity is strongest in a square region approximately equal to the size of the crystal* . . . . . 44

3.5 *The background subtracted Raman spectrum of a trapped polymethylmethacrylate bead, taken over an integration time of 10 seconds* . . 45

3.6 *The representative Raman spectra of glass (left) and water (right), taken over an integration time of 5 seconds* . . . . . 46

3.7 *Graph showing the change in intensity of the 1001 $cm^{-1}$ peak in polystyrene over time as the water flow through the microfluidic channel is switched on and off. This change in intensity is in fact present over all Raman shifts and is due to the fluorescence of the flowing water* . . . . . 47

3.8 *An example of the background fitting procedure for a trapped 3 $\mu m$ diameter PMMA bead in water, showing the original spectrum, glass spectrum, the simulated 5th order polynomial fit to the fluorescence background and the final background corrected spectrum* . . . . . 48

3.9 *Image of a three micron bead trapped by an optical trap at 532 nm (lower trap) and 1064 nm (upper trap). The upper trap is modulated at a frequency of 30Hz and thus the bead jumps between the two traps. The 1064 nm beam is set at a higher power than the 532 nm beam to ensure the bead preferentially jumps to this trap* . . . . . 50

3.10 *Power spectra at different laser power output settings. Inset: linear relationship between laser power and corner frequency, $f_0$* . . . . . 52

3.11 *Histograms of the obtained particle positions (from the trap centre) for flow rates of 0.01 ml/h and 0.05 ml/h.* . . . . . 53

3.12 *Power spectra of a single 3 $\mu m$ diameter bead trapped at the same trapping power (300 mW) for different flow rates* . . . . . 54

3.13 *The Allan deviation calculated over a range of time intervals for different noise sources in the system* . . . . . 56

3.14 *The particle image velocimetry setup mounted above the trapping optics* . . . . . 58

3.15 *A map of the normalised velocity profile in a channel of width 500 $\mu m$ for laminar flow at low Reynolds number, and the accompanying fluorescent particle image. Arrows indicate the direction of the particle velocity and arrow length/colour indicates the magnitude of the velocity* . . . . . 59

3.16 *A simple diagram illustrating Poiseuille flow through a circular channel of length $L$ and diameter $h$. The red arrows depict the flow of fluid through the tube, which has a parabolic profile* . . . . . 60

3.17 *A map of the normalised velocity profile in a channel of width 500 $\mu m$ in the presence of air bubbles, and the accompanying fluorescent particle image. Arrows indicate the direction of the particle velocity and arrow length/colour indicates the magnitude of the velocity* . . . . . 61

3.18 *A map of the normalised velocity profile in a channel of width 500 $\mu m$ when the optical trap is switched on, and the accompanying fluorescent particle image. Arrows indicate the direction of the particle velocity and arrow length/colour indicates the magnitude of the velocity* . . . . . 62

4.1 *Top: The obtained interpolated z-axis image of the fluorescence of erythrocin B excited by the 532 nm focussed excitation beam. Bottom: The calculated intensity profile over each pixel at point $f$ obtained in each axis and the Gaussian least squares fit* . . . . . 65

4.2 *Raman images taken in 3 different axes of a trapped 3 $\mu m$ diameter PMMA bead. The pixel colour is mapped to the bar on the right which indicates the normalised intensity of the 2957 $cm^{-1}$ C-H stretching peak in PMMA* . . . . . 67

4.3 *A surface Raman spectrum taken for build-up around a PMMA bead in the microfluidic channel. (a) Surface spectrum of 181 $cm^{-1}$ peak in PMMA (b) Surface spectrum of 1086 $cm^{-1}$ peak in $CaCO_3$, (c) Overlaid spectra on a camera image of the build-up, and (d) An example of the background subtracted Raman spectral data. We can clearly see that the spherical particle is a PMMA bead rather than calcite from the Raman spectrum in this area* . . . . . 69

4.4 *The background subtracted Raman spectra of material trapped in the optical trap 10 minutes after reaction begins, along with the corresponding images of the trapped particulates. In the image on the left, the spectrum is dominated by the surfactant spectrum, whereas on the right, the spectrum is dominated by the calcium carbonate spectrum. Typically a mixture of the two compounds were usually obtained* . . . . . 70

4.5 *The Raman spectrum of trapped TWEEN 20 only between 50 $cm^{-1}$ and 3100 $cm^{-1}$, showing peaks at 849.4 $cm^{-1}$, 1150.4 $cm^{-1}$, 1295.1 $cm^{-1}$, 1468.3 $cm^{-1}$ and 2905.9 $cm^{-1}$. Inset: the structure of the basic TWEEN molecule* . . . . . 71

4.6 *3D surface plot demonstrating the background subtracted Raman spectrum of TWEEN 20 trapped in the optical trap over time between 2600 $cm^{-1}$ and 3100 $cm^{-1}$* . . . . . 72

4.7 *Top: 3D surface plot showing the change in Raman spectrum over time when distilled water is flown past a trapped bead. Bottom: plots of the intensities of the known peaks of PMMA and $CaCO_3$ over time* 74

4.8 *Top: 3D surface plot showing the change in the Raman spectrum over time for freshly made solution, over a time period of 20 minutes. Bottom: plots of the intensities of known peaks of PMMA and $CaCO_3$ over time. Inset: Camera images of the trapped bead at the start of the reaction (upper) and after (lower) the reaction has taken place* . . . . . 75

4.9 *Top: 3D surface plot showing the change in the Raman spectrum over time for solution mixed and then left for 8 hours before being introduced into the channel. Bottom: plots of the intensities of known peaks of PMMA and $CaCO_3$ over time. Inset: Camera images of the trapped bead at the start of the reaction (upper) and after (lower) the reaction has taken place* . . . . . 76

4.10 *Raman spectrum obtained from phase sensitive detection of a bead trapped between two optical traps; a modulated 1064nm beam and an unaltered 532nm beam, the latter of which acts as both an optical trap and a Raman excitation source* . . . . . 78

4.11 *Figures depicting the position counts of the centre of a bead moving in an optical trap in the x and y directions. The trap on the left is a trap formed by the 532 nm laser at an output power of 50 mW* . . 80

4.12 *Figures depicting the positions of beads trapped in the 532 nm and 1064 nm traps respectively* . . . . . 81

4.13 *Histograms obtained of the motion of a tracked 3 $\mu$m bead trapped between a continuous 532 nm laser beam and chopped 1064 nm laser beam. The chopper is rotating clockwise in the left image and anticlockwise in the right image, through turning the chopper through 180 degrees parallel to the optical table* . . . . . 82

4.14 *Image depicting an example of the use of thresholding in particle position detection by the smart camera for two trapped 3 $\mu$m diameter PMMA beads held 10 $\mu$m apart; the white area is the tracked area, and the red area is discounted from position measurements* . . . . . 83

4.15 *Image depicting buildup of calcium carbonate on the surface of two trapped 3 $\mu$m diameter PMMA beads after 20 minutes* . . . . . 84

4.16 *Left: Power spectra of a bead trapped in distilled water only over a period of 30 minutes at a flow rate of 0.5 ml/h, at an output power of 100 mW. Every nth spectrum is plotted for clarity. Right: change in calculated $f_c$ using a standard Lorentzian fit (blue), the fit from equation* . . . . . 86

4.17 *Power spectra of two beads trapped in separate optical traps, in a solution of beads mixed with calcium chloride and sodium carbonate only. There is more power in the second trap than the first; this is a consequence of using the SLM to produce the traps as some light may be directed into traps more than others* . . . . . 87

4.18 *Power spectra of two beads trapped in separate optical traps, in a solution of beads mixed with the solution described in Table 3.1, Chapter 3 (with calcium chloride, sodium carbonate, chelating agent and sulphonated polyacrylate). There is more power in the first trap than in the second, as the SLM has directed more light into this trap. Inset: the calculated corner frequencies* . . . . . 88

5.1 *Photographs of the 96 well plates. The image on the right shows the plate used for washing the samples, and on the left is the plate under which samples were analysed* . . . . . 92

5.2 *Microscope images at 10x magnification of thin weave elastane (left) and thick weave polyester dacron (right) fabrics. The light regions indicate areas where there is no fabric and thus light transmission is high. In white light imaging, pixel intensities which would be obtained from these areas would not be valid* . . . . . 93

5.3 *Confocal microscope images at 10x magnification of fluorescence under ultraviolet illumination. The image to the left is of clean washed fabric showing fluorescence of optical brighteners, and the image on the right depicts the fluorescence of dried motor oil on fabric* . . . . 94

5.4 *Schematic of fabric analysing instrument, with the 96 well plate integrated into the system* . . . . . 96

5.5 *Image of the fabric samples in the well plate coated with different stains: (a) soy sauce, (b) unbleached reference cloth, (c) old cloth, (d) fruit tea, (e) strong stewed tea, (f) Ribena, (g) weak tea, (h) olive oil and (i) orange squash* . . . . . 97

5.6 *Example of the spectra obtained in reflection when illuminated by each LED for a piece of fabric stained with olive oil, before (solid white line) and after washing (dotted line), and the corresponding LED bandwidths. Of note is the UV spectrum after washing, where the fluorescence of the optical brighteners under UV light can be seen* 99

5.7 *Results obtained as graphs of normalised maximum intensity vs input wavelength for tea, olive oil and soy sauce, where ∘ indicates washed fabric and △ indicates unwashed fabric. Results on the left are for reflected light and on the right are for transmitted light. Error bars are the standard error on the 5 values obtained for each measurement. The dotted lines indicate the transmitted and reflected intensities of light incident on clean, previously unwashed fabric, which was used as the normalisation factor* . . . . . 100

5.8 *Results obtained as graphs of normalised FWHM vs input wavelength for tea, olive oil and soy sauce, where ∘ indicates washed fabric and △ indicates unwashed fabric. Results on the left are for reflected light and on the right are for transmitted light. Error bars are the standard error on the 5 values obtained for each measurement. The dotted lines indicate the transmitted and reflected intensities of light incident on clean, previously unwashed fabric, which was used as the normalisation factor* . . . . . 101

5.9 *Graphs showing the weighting of the intensities for different stains (individuals) and different illumination wavelengths (variables) along the principal axes* . . . . . 104

5.10 *Graphs showing the weighting of the FWHMs for different stains (individuals) and different illumination wavelengths (variables) along the principal axes Dim1 and Dim2* . . . . . 105

6.1 *Figure showing the attenuation of light of initial intensity $I_0$ attenuated through a material with molar absorption coefficient $\epsilon$ and path length $l$* . . . . . 110

6.2 *(a) SEM image of a human hair showing the keratin layers of the cuticle (taken from [7]), (b) the structure of a human hair (taken from [8]), showing the cortex layer underneath the cuticle, which is the part of the hair responsible for its colour* . . . . . 112

6.3 *Image adapted from Micronit microfluidics of the flow channel cross section (not to scale)* . . . . . 113

6.4 *Images showing the problem of non-matching refractive indices when taking spectra of microfluidic channels (a) an empty channel, (b) channel filled with water, (c) channel with Illumina 5/- dye after 10 minutes* . . . . . 114

6.5 *An example (not to scale) of some of the possible aberrations encountered in the microfluidic channel, through the use of a) tightly focussed broadband light (chromatic aberration), b) the presence of bubbles (spherical aberration) or c) the presence of air (defocus)* . . 116

6.6 *Simple setup for investigating the absorbance spectrum of a 20 ml sample of hair dye. The alignment here is not critical as the idea is to focus the light onto the sample and collect light from a small area underneath* . . . . . 118

6.7 *Schematic of the experimental setup* . . . . . 119

6.8 *Photograph of the experimental setup* . . . . . 119

6.9 *A plot of the emission intensity of fluorescein when the white LED is replaced with a blue LED, against the position of the microfluidic channel in $\mu$m, and the corresponding fit in red, which was found to be a Lorentzian. The channel width may be determined from the full width half maximum of the fit.* . . . . . 120

6.10 *Images depicting examples of the possible camera images we can obtain. In (a), we have an ideal image. In (b), there is a bubble flowing through the channel and thus our obtained spectrum will be suboptimal. In (c) the chassis has not been mixed thoroughly enough and a blob of chassis is flowing past. In (d) the bubble flowing past is so large that we can't see the edges* . . . . . 123

6.11 *Figures showing pixel intensity (0-255) values against number of pixels, each corresponding to an example 5 second averaged spectrometer reading. 50 histograms are plotted for the 50 images taken by the camera in the 5 seconds, corresponding to 10 averaged spectrometer spectra. a) is an example of a good reading, b) is the typical histogram of imaging inside a bubble, and c) is the obtained spectrum when a small bubble is present (the spike at the low RGB values indicates a dark bubble edge being detected)* . . . . . 124

6.12 *Absorbance spectra over a 9 minute period (with readings at one minute intervals) for a sample of blonde hair dye (Wella Illumina 9/-)* . . . . . 125

6.13 *Absorbance spectra over a 9 minute period (with readings at one minute intervals) for a sample of brown hair dye (Wella Illumina 5/-)* . . . . . 126

6.14 *Typical spectrum of the white light LED used in this experiment* . . 127

6.15 *Rate constants for brown hair dye (left) and blonde hair dye (right). The red lines indicate the obtained results by our setup; the blue lines indicate P&G's results* . . . . . 128

6.16 *An example of a) Poor absorbance-wavelength plots obtained over time due to bubbles, b) A better example of the absorbance-wavelength relation over time showing the overall increase in absorbance. Results have been smoothed for clarity* . . . . . 129

6.17 *Plot of absorbance vs log time for a sample of brown hair dye (without bubbles) and the corresponding fits* . . . . . 129

6.18 *Rate constant plotted against wavelength for 8 samples of the same brown hair dye shade* . . . . . 130

A.1 *Spectral response of LUPA 300 sensor (taken from specifications at http://www.fastvideo.ru/info/sensor/cypress/lupa*$_3$*00.pdf)* . . . . . 144

# List of Tables

2.1 *Experimentally obtained Raman vibrational modes of calcite* . . . . 26

3.1 *Dishwashing formula for 5L water* . . . . . 63

# Chapter 1

# Introduction

In our day to day life, we are dependent on many chemical and physical processes, such as those used to clean clothes or dishes and in hair salon environments, which have been developed to make our lives easier. These processes may have inherent problems, and are subjected to rigorous testing in industry to ensure optimum efficiency and effectiveness, even more than in the past as people's lives become busier. The theme of this thesis is primarily based on looking at both development of existing testing methods, and finding solutions to problems encountered in everyday use through the use of miniaturised optical instrumentation, with potential for high-throughput screening.

Dishwashers have become a common household product, with approximately 40% of UK homes owning a dishwasher in 2010 [9]. The washing process occurs via spraying hot water and detergents onto soiled items, at temperatures between 55°C and 75°C depending on the make and country [10]. The dishes are then rinsed and the water drained, and the dishes are then dried using hot air. The cycle typically takes place over a time period of 1-2 hours. Even given the extra expense of heating the water, if fully loaded dishwashers are used at most once a day, along with economy programs, they save energy, money and water; in fact, a study in 2011 [11] found that for four European countries, households with a dishwasher used on average 50% less water and 28% less energy per cleaned item compared with houses that did not. However, there are also some problems which

accompany these benefits, which are not found in hand washing. For example, harsher chemicals are necessary in dishwasher cleaning fluids or powders, which are necessary to remove soils from dishes without the hand 'scrubbing' action used in hand washing. The alkaline nature in particular of dishwasher detergents causes a reaction between the detergent and metal ions found in hard water, causing the formation of magnesium and calcium carbonate. This precipitation crystallises on glasses and appears as a white cloudy film, and though non-toxic, it provides an annoyance for the consumer and necessitates the replacement of glass and plastic items, in some cases even prohibiting the use of dishwashers for plastic items, on which the effect is worst. This is also an annoyance in pipes, as the incrustation of calcium carbonate in water piping systems is an environmentally and economically damaging factor [12].

The crystallisation on the surface of items in the dishwasher is generally grouped into two categories; spotting, where white spots appear on glassware, and filming, which is a much more uniform cover across the surface of the material. Spotting occurs due to uneven drying on the surface of items, and is countered through the use of rinse-aid. This contains surfactants which use the Marangoni-Gibbs effect [13] to prevent droplets forming on surfaces; a surface tension gradient is created which causes water to drain from surfaces in thin sheets. This does not however solve the problem of filming, which is thought to be driven to an extent by the properties of the surface on which the filming occurs. For example, the effect is much more pronounced on curved surfaces, such as the cylindrical outside surface of drinking glasses, and on plastic materials such as polystyrene and acrylic rather than borosilicate glasses. Inhibitors and additives have been developed to try to control and prevent the problem of filming. However, some of these inhibitors may be environmentally unfriendly, especially given that some are typically phosphate-based, which is often not removed properly during water purification. This increases the populations of phosphate-dependent organisms, such as plants and algae, which in excess amounts reduces the oxygen content of water for aquatic life. The development of new inhibitors which have similar effects but

do not contain these chemicals is therefore an important industrial process.

It is therefore useful to be able to investigate such reactions on a miniaturised scale. The methods employed in this thesis involve the use of microscopic techniques to investigate everyday processes, examples of which are microfluidics, spectroscopy, confocal systems and optical tweezing. Specifically, we investigate the phenomenon of filming, and in later chapters we then focus on other everyday processes, namely clothes washing and hair dying. In these chapters particularly we investigate new microscopic and spectroscopic methods with a view to improve current monitoring methods used by Proctor and Gamble.

In this thesis, Chapter 2 details the theoretical considerations behind the phenomena of optical trapping and Raman spectroscopy, and explores some of the theory behind microfluidic systems and the problem of calcium carbonate deposition.

Chapter 3 goes on to describe the instrumentation developed for Raman tweezing and the methodologies used to simulate a dishwasher environment at a microscopic scale.

Chapter 4 describes the results obtained from the Raman tweezers setup and discusses the suitability of this system for technological screening of dishwasher solutions.

Chapter 5 describes a new method of monitoring the effectiveness of clothes detergents on dirty washing. This relatively simple method measures the reflected and transmitted light from 5 different coloured LEDs through small fabric samples stained with some common stains through well plates. Principal component analysis (PCA) is then used to compare the stains and find any relation between the obtained spectra, and the effect of oily stains on washing.

Chapter 6 notes the development of monitoring the reaction between hair dye and developers over time in thin microfluidic channels, with an outlook to developing a fully automated hair dye testing system. This advances a current method by Proctor and Gamble of monitoring hair dye development over time using absorbance spectroscopy with broadband light.

Chapter 7 concludes the thesis and summarises the work.

# Chapter 2

# Theoretical Considerations for building a miniature dishwasher

*This chapter details the theory behind the phenomena of optical tweezing and Raman spectroscopy, the mechanisms of calcium carbonate formation, and the use of instrumentation including SLMs and microfluidic channels.*

## 2.1 Optical Tweezers

### 2.1.1 Theory of optical trapping

In 1970, Arthur Ashkin was working at Bell Laboratories when he first reported the effects of optical scattering and gradient forces on micron sized particles [14], which led to stable trapping of particles [15]. This was later developed by Steven Chu in his work on cooling and trapping neutral atoms, which earned him the Nobel Prize in 1997 for the Magneto-Optical trap. Optical tweezers themselves are used for trapping larger objects in the nanometre to micrometre range in a tightly focussed laser beam.

Optical tweezers operate via light exerting a force on transparent dielectric particles. Light has momentum, and hence the force is due to the momentum of light being transferred to the particle, either through being absorbed or scattered. A

particle experiences several forces in a Gaussian $TEM_{00}$ profile beam due to absorption and scattering of light; gradient forces which act towards the point of greatest light intensity, and radiation pressure which acts along the direction of propagation of the beam. Elastic light scattering phenomena with particles are generally divided into two categories, which are:

- the case in which the size of the trapped particles is larger than the wavelength of the trapping light, also known as the Mie regime, and
- the case in which the particles are smaller than the wavelength of the trapping light known as the Rayleigh regime.

In the Rayleigh regime, the particle is treated as an induced point dipole in an inhomogeneous electromagnetic field. In this field it experiences both a force due to light scattering and a gradient force due to the light being focussed. The scattering force is directed along the direction of propagation of the light beam and is given by [16]:

$$F_{scattering} = \frac{I_0 \sigma n_m}{c} \tag{2.1.1}$$

where $n_m$ is the refractive index of the surrounding medium, $I_0$ is the intensity of the trapping beam and $c$ is the speed of light in a vacuum. The particle cross-section, $\sigma$, is given by:

$$\sigma = \frac{8}{3}\pi k^4 r^6 \left(\frac{m^2 - 1}{m^2 + 2}\right)^2 \tag{2.1.2}$$

where $r$ is the particle radius, $m$ is the ratio of particle refractive index to medium refractive index and $k$ is the light wavevector given by $2\pi/\lambda$, where $\lambda$ is the wavelength of the trapping laser.

The gradient force is due to the Lorentz force acting on the dipole induced by the electromagnetic field, given by:

$$F_{grad} = \frac{2\pi\alpha}{c n_m^2} \nabla I_0 \tag{2.1.3}$$

where $\alpha$ is the polarizability of the dielectric (assuming the particle is linear and thus polarization $\vec{p}$ is related to electric field $\vec{E}$ by $\vec{p} = \alpha\vec{E}$), given by:

$$\alpha = n_m^2 r^3 \left(\frac{m^2 - 1}{m^2 + 2}\right) \tag{2.1.4}$$

The gradient force is thus proportional to the gradient of the intensity, and acts as a restoring force to the centre of the beam waist when $m > 1$.

In the Mie regime, basic ray optics may be used to describe the forces acting on a trapped bead, as demonstrated in Figure 2.1. In the case of an unfocussed Gaussian beam, individual rays of light are refracted as they enter and exit a dielectric bead according to the relative refractive indices of the bead and medium. This change in direction of the light rays corresponds to a change in their original momentum. According to Newtons third law, this implies an equal and opposite change to the momentum of the bead, therefore the bead must experience a force. Given that the input beam has a Gaussian profile, the intensity of the beam is greater at the centre and so the force caused by the light momentum transfer from the centre of the beam will be greater than the force on the bead caused by the edges of the beam (that is, the Gaussian 'tail'), as shown in part (a) of Figure 2.1. The direction of the momentum and thereby the force vector is therefore towards the centre of the beam and so the bead is pushed to the centre. Thus, two-dimensional trapping is achieved.

However, the beads motion must be restricted axially (parallel to the direction of the beam) to obtain full three-dimensional optical trapping. To restrict the beads motion in three dimensions, a gradient must also be added to the beam in the axial direction. This is achieved through focussing the beam through a high numerical aperture microscope objective. The numerical aperture of the microscope objective indicates how tightly the beam is focussed; oil immersion objectives are usually used for this reason as they have a numerical aperture (NA) greater than 1, as the refractive index of the oil is closer to that of the glass objective (or of

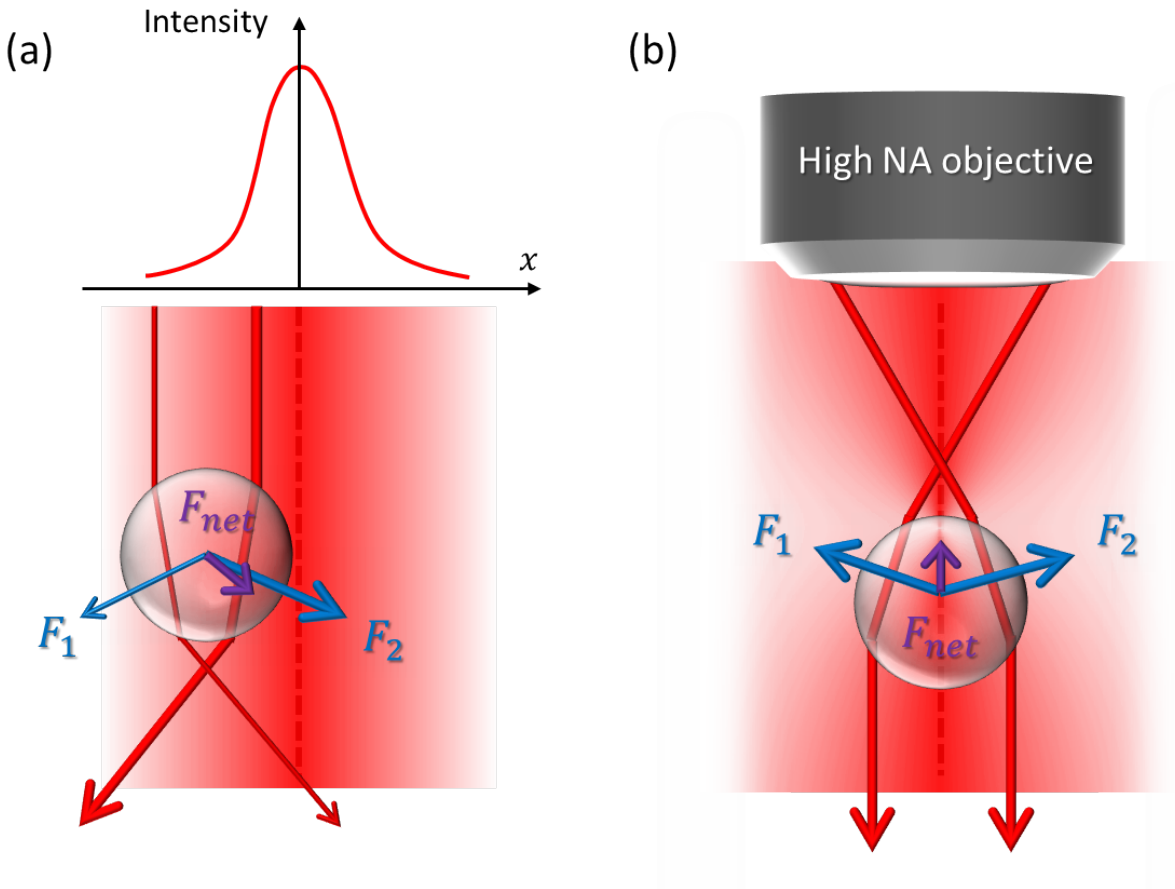


Figure 2.1: *Diagrams demonstrating (a) refraction of a Gaussian beam through a dielectric bead causing a strong restoring force $F_{net}$ towards the maximum intensity region of the beam, and (b) full three-dimensional trapping through the use of an objective lens to focus the light beam, creating a force $F_{net}$ which pushes the bead in the direction of beam propagation towards the beam focus (the bead is stably trapped slightly underneath the beam focus)*

water, which may also be used as an immersion medium) than that of air. The rays of light therefore are directed towards the beam focus, and are refracted such that they gain momentum parallel to the beam axis as well as towards the middle of the Gaussian beam, as shown in part (b) of Figure 2.1. The resultant force pushes the bead to create a stable trapping point just behind the beam focus; the bead is not trapped at the focus itself as the laser beam is also reflected from the surface of the bead, which causes a scattering force in the direction of the trapping beam's direction of propagation.

The restoring force towards the centre of the trap is linear with distance (for small deviations), and thus the optical trap can be modelled as a Hookean spring, of the form $\vec{F} = -k\vec{x}$. The spring constant, $k$, is called the trap stiffness and is an important factor in the calibration of optical traps. The potential energy stored when a trapped specimen is displaced by a distance $x$ is thus:

$$U = \frac{1}{2}kx^2 \tag{2.1.5}$$

The depth of the resulting potential energy well at the trapping focus is determined by the laser density at the focus (related to the laser power output and the numerical aperture of the objective lens used), the size of the beads being trapped, the material the bead is made from (in particular its refractive index) and the viscosity of the surrounding medium. A lower laser power means there will be fewer photons changing momentum as they pass through the bead, which implies a lower force, as shown in equations 2.1.1 and 2.1.3. Bead size also has an effect on the trapping force, and the relation of trapping force to bead size is nonlinear [17]. Larger beads experience more viscous drag but less of the bead is inside the laser beam area, so less force is exerted on the bead, which manifests itself as larger beads being easier to initially trap but easier to push out of the trap. The relationship between the bead size and trapping wavelength (and hence beam size) is also of importance; generally, the closer the size of a bead to the beam wavelength, the stronger the trap.

The relative refractive indices of both the particle being trapped and the medium the particle is trapped in similarly affects how strongly the particle is held in the trap. The medium of the particle to be trapped must have a higher refractive index than that of the surrounding medium, as this is what causes the light rays to deviate and hence what causes the trapping force. Any specimen trapped in an intensity gradient with a refractive index lower than that of the trapping medium, such as an air bubble in water, is directed away from the trapping focus. This in itself may be used to trap such particles if they are surrounded by a negative intensity gradient, in which case the particle is repelled in all directions towards a single point, rather than being attracted to a single central focus. [18].

### 2.1.2 Development and applications of Optical Tweezers

Over the past twenty years since Ashkin's first foray into trapping, the field of optical tweezers has greatly expanded. Given that optical tweezers may be used to trap most semi-transparent objects, they have numerous applications in the biological sciences. For example, by attaching beads to the end of DNA strands, it is possible to measure the elasticity of DNA [19]. Optical tweezers also have applications in probing molecular motors, such as kinesin and myosin [20].

Given that optical tweezers restrict the Brownian motion of species, they have many uses in microscopy. For example, fluorescence microscopy is easily combined with optical tweezers [21], and the trapping beam itself may be used to excite fluorescence, although due to photobleaching it is sometimes easier to use a separate excitation illumination system. Optical tweezers may also be used for identification, and have been combined with infrared spectroscopy [22] and, as is the case in this thesis, with Raman spectroscopy. If the species is coated with a coinage metal, such as gold, silver or copper, it is even possible to obtain surface enhanced Raman spectroscopy [23], which is useful given the small masses which can be trapped in tweezers, though not relevant in the context of this thesis due to the chemical processes used being sensitive to the surface properties of trapped species

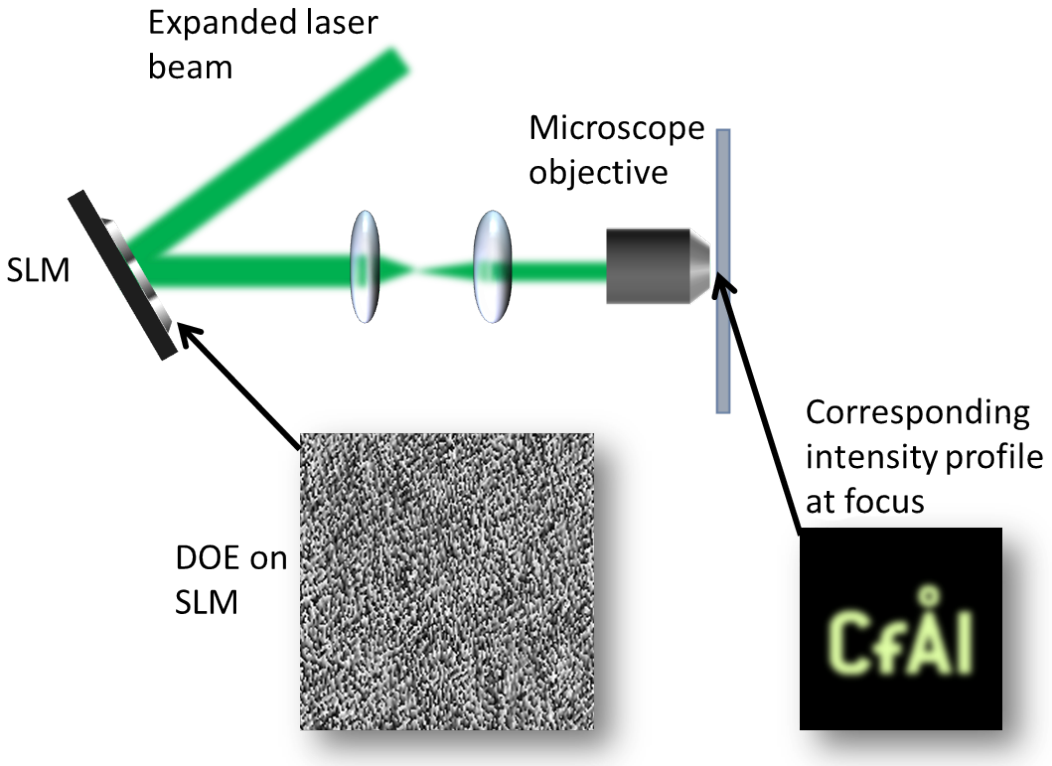


Figure 2.2: *Example of the typical optical train for holographic optical tweezers, and an example DOE and the corresponding intensity pattern at the focus*

which change once they are coated with the metal.

## 2.2 Holographic Optical Tweezers

### 2.2.1 Modifying the trapping beam through use of an SLM

By altering the shape of the Gaussian trapping beam, we can extend the utility of optical tweezing. Multiple traps were first attempted through the use of scanning mirrors to scan quickly between two traps. The use of diffractive optical elements (DOEs) was first demonstrated in 1998 [24] to create optical tweezer arrays. DOEs may also be used to exert control over a single trap; for example, by creating a blazed grating, we may control the trap's lateral position, and through creating a Fresnel lens phase we may control the trap's axial position. This is known as holographic optical tweezing.

Holographic optical tweezers use computer generated holograms, or diffractive optical elements, to alter the phase of light and thus adjust the intensity pattern of light at the trapping focus, allowing for more complex trapping scenarios, such as trapping several particles at once. Spatial light modulators, or SLMs, are key devices in manipulating the phase of incident light. SLM devices may be optically or electrically addressed. Optically addressed devices (OASLMs) produce patterns via a photosensor which detects incoherent light encoded with an image on the front or back surface of the SLM [25]. A photosensor detects the brightness of each pixel and replicates the image using liquid crystals. Electrically addressed SLMs (EASLMs), however, serve as more of an optical 'input device', linking imaging optics to electronics; some of the most common examples are deformable mirrors and liquid crystal devices. In deformable mirrors, a voltage is used to move a two dimensional array of mirrors, and the reflection of light from the mirrors causes a phase change; these are used extensively in adaptive optics [26] and are finding new uses in femtosecond pulse changing [27]. In liquid crystal displays, an applied voltage to an electrode causes the crystal to rotate by an angle which increases with the voltage. The rotation of the liquid crystal thereby causes a change in its effective refractive index, which causes a phase change to appropiately polarised light travelling through the liquid crystal. Thus, we may control the phase of our impinging light beam depending on which pixel it falls on. Liquid crystal displays may work in either transmission (which makes uses of thin-film transistors) or reflection, which uses a silicon backplane; an example cross section of a liquid crystal on silicon (LCoS) SLM is shown in Figure 2.3. Resolutions of up to 2048x1536 (QXGA) are possible [28].

Different patterns displayed on the SLM manifest as different intensity patterns of diffraction limited spots in the trapping plane (which become the trapping foci). For example, displaying a blazed grating on the SLM gives diffraction spots in the sample plane, and we may spatially filter out the zeroth order spot if necessary to obtain a trap we can move around by altering the frequency of the grating. The phase pattern necessary at a point $u, v$ on the SLM to move the trap from the

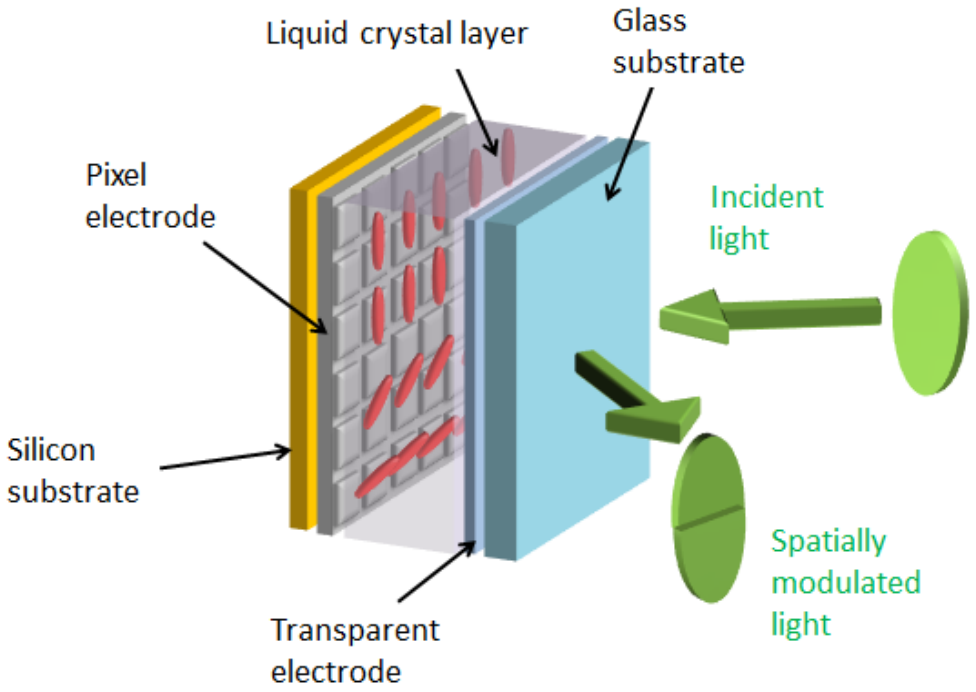


Figure 2.3: *Schematic (adapted from [1]) of the operation of a reflecting liquid crystal on silicon (LCoS) spatial light modulator. The liquid crystal states are controlled for each pixel through a DVI connection*

zeroth order focus to position $x, y, z$ is calculated from [29]:

$$\phi_{3D}(u,v) = \left[\frac{kux}{f} + \frac{kvy}{f} + \frac{kz(u^2+v^2)}{2f^2}\right] \mod 2\pi \tag{2.2.6}$$

where $k$ is the wavenumber $k = 2\pi/\lambda$, and $f$ is the focal length of the Fourier lens.

We may create multiple traps through the argument of the complex addition of these phases:

$$\phi_{total}(u,v) = \arg\left(\sum^{N} \exp(i\phi(u,v)_n)\right) \tag{2.2.7}$$

where $N$ is the number of traps.

It is also possible to use SLMs to correct beam aberrations in a trap and to create beams with optical angular momentum. The complex addition of Zernike modes with the desired hologram allows for correction of the focussed spot, a key element in the production of compacted holographic tweezer instruments [30]. Beams with

optical angular momentum, also called 'optical spanners', have been used to trap particles [31] [32].

For beams with helical phasefronts, the Poynting vector has an azimuthal component which produces orbital angular momentum parallel to the beam axis. The most common form of beam with helical phase is the Laguerre-Gaussian laser mode. These may be used to trap particles which are highly absorbing or reflecting, such as metal nanoparticles, or particles with a lower refractive index than the surrounding medium, for example microbubbles.

## 2.3 Characterising the motion of optically trapped species

### 2.3.1 Equipartition

In 1827, Robert Brown found that pollen grains suspended in water underwent motion in the fluid [33], which became known as Brownian motion. The mechanism by which this occurred was later studied by Einstein [34], who used statistical mechanics to model the phenomenon. Particles suspended in a liquid move randomly due to collisions with the moving molecules in the liquid. This is highly relevant in the case of an optically trapped bead in thermal equilibrium; the motion of such a bead may be modelled as oscillations in a harmonic potential with spring constant $k$ (see equation 2.1.5). We may model the variance of the residual Brownian motion, $\langle x^2 \rangle$ of the bead via the equipartition of energy, which states that each degree of freedom in a harmonic potential has $1/2k_BT$ of energy:

$$\frac{1}{2}k_BT = \frac{1}{2}k\langle x^2 \rangle \tag{2.3.8}$$

where $k_B$ is the Boltzmann constant and $T$ is the absolute temperature. We may therefore obtain the spring constant, $k$, which is related to the trap strength, if we know the temperature and the variance of the particle position, which may

be measured using cameras and particle tracking; this is expanded upon in later sections.

However, in practice this is not the best method for obtaining the trap strength, due to the possibility of unwanted vibrations increasing the value of $\langle x^2 \rangle$ and thus underestimating the value of $k$. A more rigorous method of analysing the bead motion is to take into account all the frequencies of the bead's motion, allowing for identification of drift and noise contributions.

### 2.3.2 Monitoring particle position

To characterise the motion of particles, it is necessary to be able to track them accurately. In this work, a smart camera developed by Durham Smart Imaging [35] was used to monitor particle positions. This uses an on-board centroiding algorithm to calculate the positions of particles according to a thresholding value set by the user. When illumination light is focussed onto a sample, focussed transparent particles appear as bright spots surrounded by a dark area. We can therefore make use of a centre of mass algorithm on the image in which background pixels are eliminated and thus the $x$ and $y$ coordinates of each particle are found using:

$$x = \frac{\Sigma(x_i A_i)}{\Sigma(A_i)} \quad y = \frac{\Sigma(y_i A_i)}{\Sigma(A_i)} \tag{2.3.9}$$

where $x_i$ is the distance of a pixel from a predefined area of the image (in pixels) and $A_i$ is the brightness of that pixel. Positions may be saved to disk and later analysed.

### 2.3.3 Autocorrelation and Power Spectral Analysis

The frequency content of a trapped particle's motion may be related to the strength of the optical trap. As the stiffness of an optical trap increases, the higher frequency components of a trapped particle's motion tend to dominate more. These frequencies typically go up to a few kHz.

The Langevin equation for a harmonically trapped particle is [36]:

$$m\ddot{x} + \gamma_0\dot{x} + kx = F(t) \tag{2.3.10}$$

Where $m\ddot{x}$ is the inertial term and disappears for micron sized objects, $\gamma$ is the drag force from Stokes' law ($\gamma_0 = 6\pi\eta r$), $kx$ is the trapping force and $F(t)$ is the fluctuating Brownian force for which $\langle F(t)\rangle = 0$, which may be expressed as $F(t) = \sqrt{2k_BT\gamma_0}\eta(t)$, $\eta(t)$ describing a random Gaussian process.

Given that the system is heavily overdamped, the inertial forces experienced by the bead are negligible compared to viscous and trap forces. We may therefore drop the inertial term to obtain:

$$\dot{x} + 2\pi f_c x(t) = (2D)^{1/2}\eta(t) \tag{2.3.11}$$

where $f_c$ is the 'corner frequency', an important parameter which will be discussed in detail, and $D = k_BT/\gamma_0$

After a time $\tau$, this may be Fourier transformed into the frequency domain to obtain:

$$\tilde{x} = \int_{-\tau/2}^{\tau/2} e^{i2\pi ft}x(t)dt = \frac{(2D)^{1/2}\tilde{\eta}}{2\pi(f_c - if)} \tag{2.3.12}$$

and the power spectrum $S$ at frequency $f$ is thus given by:

$$S = \frac{|\tilde{x}|^2}{\tau} = \frac{D/2\pi^2}{f_c^2 - f^2} \tag{2.3.13}$$

This function is characteristic of the Lorentzian function, as can be seen in a theoretically calculated plot in Figure 2.4; we observe a fixed power spectrum until a certain frequency at which there is a rapid decrease; this is known as the corner frequency, $f_c$, which is closely related to the trap stiffness. By fitting a Lorentzian to an experimentally obtained spectrum, we may thus determine $f_c$,

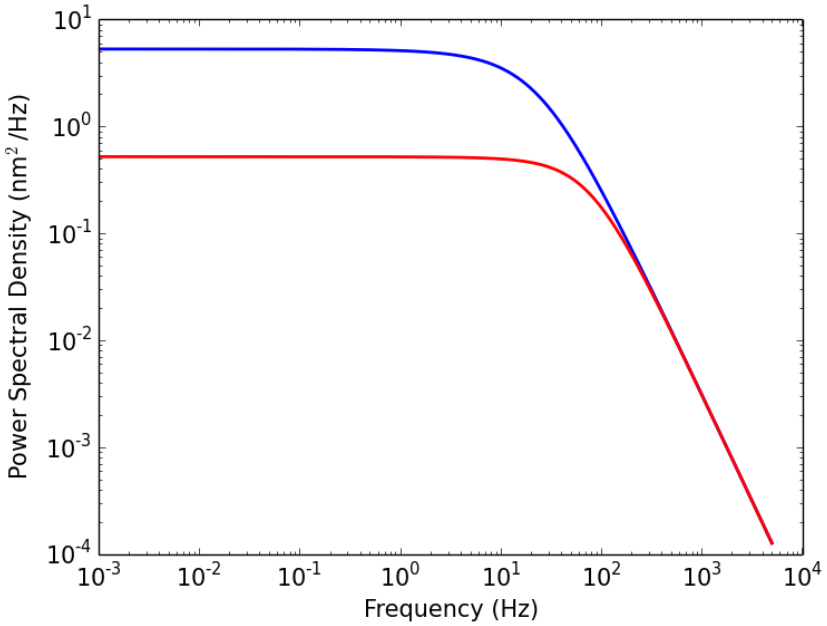


Figure 2.4: *A theoretical example plot of the power spectrum for species trapped in a strong optical trap (red) and a weak trap (blue)*

and then the trap stiffness $k$ via:

$$k = 2\pi\gamma f_c \tag{2.3.14}$$

The power spectrum is one of the more reliable ways in which to calibrate an optical trapping system since analysis of the frequency domain provides information about sources of noise. For example, external vibrations arising from people working in the laboratory may contribute to lower frequency noise, or a vibration at 50 Hz or 100 Hz may originate from a mains-powered piece of equipment in the vicinity, such as cooling fans.

The autocorrelation function of a bead's motion relates the motion of a bead in an optical trap to itself. If $N$ measurements of a particle's motion in an optical trap are taken over time, the particle autocorrelation is given by:

$$A_j = \frac{\Sigma_{n=0}^{N} x_n x_{n-j}}{(\Sigma_{n=0}^{N} x_n)^2} \tag{2.3.15}$$

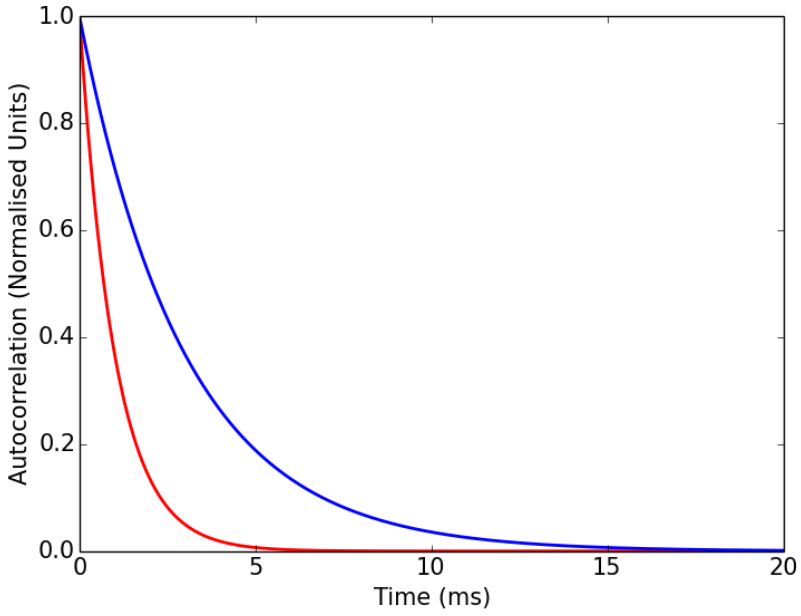


Figure 2.5: *An example of the autocorrelation function for a species trapped in a strong optical trap (red) and a weak trap (blue)*

where $A_j$ is the $j^{th}$ reading.

The autocorrelation is related to particle relaxation time $\tau$ by:

$$A(t) = e^{-t/\tau} \tag{2.3.16}$$

In physical terms, $\tau$ may be thought of as the time it takes for a trapped specimen to return to the trap centre after being displaced; a more stiffly trapped particle will have a smaller value of $\tau$.

### 2.3.4 Stokes Drag

It is possible to use the viscosity of the trapping medium to measure optical trap strength. In this scenario, we move the sample stage (and hence the fluid trapping medium) at a constant velocity $v_s$. The force is calculated from Stokes' law [37]:

$$\vec{F_d} = 6\pi\mu r\vec{v_s} \tag{2.3.17}$$

where $\mu$ is dynamic viscosity and $r$ is the bead radius. This force causes a displacement of the bead from the trap centre, $x$. If the trap is modelled as a harmonic oscillator, the trap stiffness may therefore be given by:

$$k = \frac{\vec{F_d}}{\vec{x}} \tag{2.3.18}$$

This method of moving a bead in a fluid medium may also be used to measure the trapping force. If the bead is accelerated until it breaks free from the trap, the trap force is equal to the drag force required for the bead to be freed [38].

## 2.4 Raman Spectroscopy

### 2.4.1 An Introduction to Raman Scattering

Predictions of the inelastic scattering of light had been made as far back at 1923 [39], and were first observed in 1928 by Sir C.V. Raman. Raman used sunlight passed through a narrow band photographic filter to create monochromatic light which was focussed onto a sample. A lens was placed at 90 degrees to the input beam to collect the scattered radiation which was passed through a crossed filter, (a filter which blocks the pass band of the first filter and allows all other light through) onto a photographic plate. It was found that some light passed through the crossed filter; it had been inelastically scattered. The discovery of the change of the energy of incident photons impinging on a sample earned him the 1930 Nobel prize.

When light is incident on a material, it may be scattered, absorbed, or pass through. The vast majority of light impinging on a molecule undergoes Rayleigh scattering, which is an elastic effect and proportional to $\lambda^{-4}$. The incident photon raises the energy of the molecule to a virtual excited state, which is extremely short lived ($10^{-14}$ s) and subsequently, the molecule decays to the ground state. The photon which is then emitted by the molecular state transition has the same energy as this transition. Thereby the scattered photons have the same wavelength

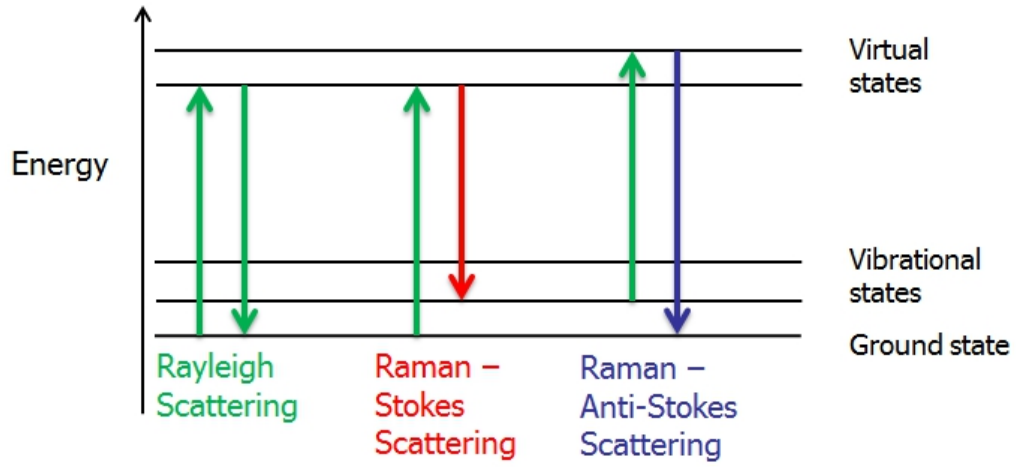


Figure 2.6: *Jablonski diagram depicting the change in the energy of an incident photon on interaction with a molecule in the cases of elastic (Rayleigh) and inelastic (Raman-Stokes and Raman Anti-Stokes) scattering*

as the original impinging photon.

In Raman scattering, the photon either gains or loses energy in the process and therefore the wavelength respectively either decreases (Raman anti-Stokes scattering) or increases (Raman Stokes scattering), as demonstrated in Figure 2.6. This is much rarer than Rayleigh scattering, and occurs to approximately every $10^7$ incident photons.

The Raman shift is typically given as a wavenumber, and is calculated as:

$$\Delta\omega_{shift} = \left(\frac{1}{\lambda_{exc}} - \frac{1}{\lambda_{em}}\right) \tag{2.4.19}$$

where $\Delta\omega_{shift}$ is the Raman shift (usually given in units of inverse centimetres), $\lambda_{exc}$ is the excitation wavelength and $\lambda_{em}$ is the Raman spectrum wavelength. The scattered radiation from the sample may be collected and a spectrum formed. This spectrum allows us to distinguish between materials, which may look similar, for example in Figure 2.7, which shows an application of Raman spectroscopy in gem identification. Raman spectroscopy is also used in mineral identification, and since it has strong peaks for organic molecules, Raman microspectroscopy is often used

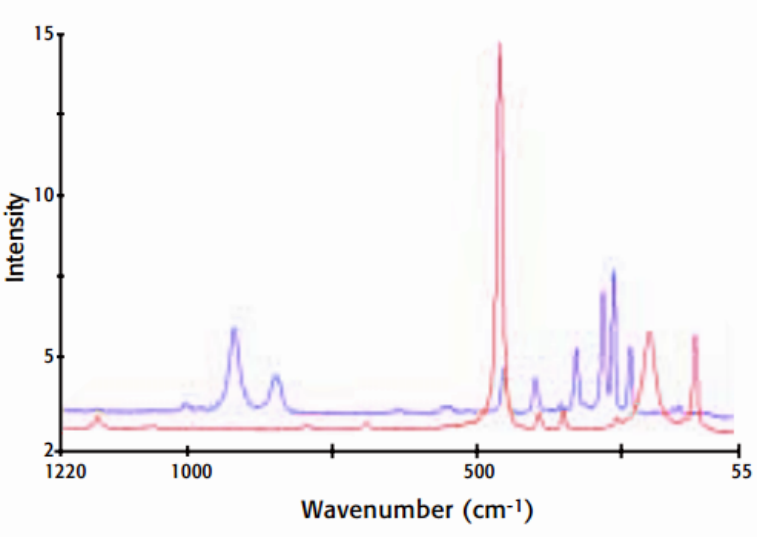


Figure 2.7: *Figure adapted from [2] showing the difference between the Raman spectrum of topaz (red) and citrine (purple). Citrine is a natural quartz crystal which is often passed off as topaz, a considerably more expensive gem*

in the biological sciences.

### 2.4.2 Classical and Quantum theories of Raman Scattering

In the classical theory of Raman scattering, the electric field of the light wave interacts with the electrical charges in the material being excited. For a single molecule interacting with an electric field $\vec{E}$ induced by electromagnetic radiation of angular frequency $\omega_0$, the induced dipole moment $\vec{P}$ is given by:

$$\vec{P} = \boldsymbol{\alpha}\vec{E}_0 \cos(\omega_0 t) \tag{2.4.20}$$

where $\boldsymbol{\alpha}$ is the polarizability of the molecule, and is a scalar for isotropic molecules and a tensor for non-isotropic molecules, which is the case for nearly all molecules. For small vibrational amplitudes, the polarizability is related to the vibrational coordinate $q_n$ by the equation:

$$\boldsymbol{\alpha} = \boldsymbol{\alpha_0} + \left(\frac{\partial \boldsymbol{\alpha}}{\partial q_n}\right)_{q=0} q_n \, (+...) \tag{2.4.21}$$

The coordinate $q_n$ is related to the vibrational frequency by:

$$q_n = q_0 cos(\omega_n t) \tag{2.4.22}$$

where $q_0$ is the normal coordinate of the initial position. Substituting this and the definition of $\boldsymbol{\alpha}$ into the equation for $\vec{P}$, we obtain:

$$\vec{P} = \boldsymbol{\alpha_0}\vec{E}_0 \cos(\omega_0 t) + \left(\frac{\partial \boldsymbol{\alpha}}{\partial q_n}\right)_0 \vec{E}_0 q_0 \cos(\omega_n t)\cos(\omega_0 t). \tag{2.4.23}$$

This through a trigonometric identity may be converted to:

$$\begin{aligned}\vec{P} &= \boldsymbol{\alpha_0}\vec{E}_0 \cos(\omega_0 t) \\ &+ q_0/2 \left(\frac{\partial \boldsymbol{\alpha}}{\partial q_n}\right)_0 \vec{E}_0 \left(\cos(\omega_0 + \omega_n)t + \cos(\omega_0 - \omega_n)t\right)\end{aligned} \tag{2.4.24}$$

This equation describes both the Rayleigh and Raman scattering. The first term contains the frequency $\omega_0$, the incident radiation frequency, and thus describes the elastic Rayleigh component. The second term also contains the frequencies $\omega_0 - \omega_n$ (the Stokes line) and $\omega_0 + \omega_n$ (the anti-Stokes line), with which the dipole may oscillate. It is the derivative of the polarizability $\boldsymbol{\alpha_0}$ which thus dictates the properties of the Raman scattering, and if this is equal to zero there will be no Raman modes.

However, these equations fail to account for the differing intensities of the Stokes and anti-Stokes lines; in fact they are predicted to be of the same intensities whereas the anti-Stokes lines are generally much weaker. A quantum theory of Raman scattering is necessary to describe this, where molecular vibrations are quantized. The scattering is therefore described via phonons, which are excited by the incident photons. Whether they are created and annihilated depends on the probability of finding the system already in an excited vibrational state.

The polarizability tensor in the quantum mechanical treatment is now an expectation value given by [40]:

$$\langle \alpha_{ij} \rangle_{ab} = \langle \psi_b | \alpha_{ij} | \psi_a \rangle \tag{2.4.25}$$

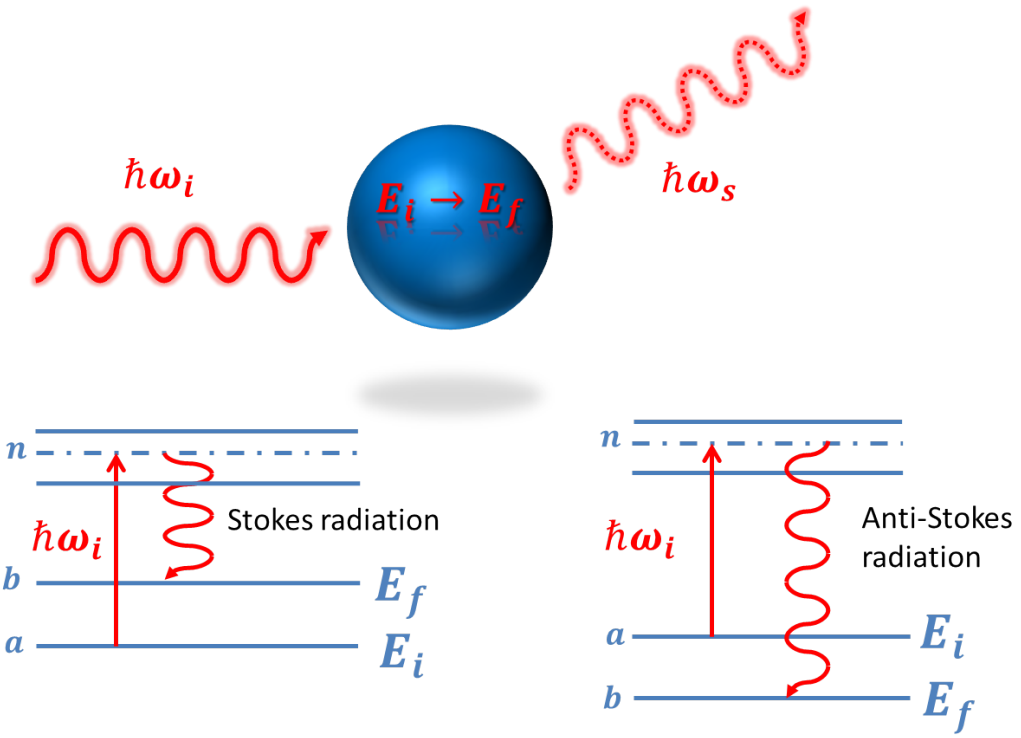


Figure 2.8: *A schematic (adapted from [3]) demonstrating the emission of a photon with energy $\hbar\omega_f$ after the incident photon with energy $\hbar\omega_i$ causes a change of vibrational state from level $E_i$ to $E_f$*

where $|\psi_a\rangle$ represents the energy eigenfunction of the level $a$ and $|\psi_b\rangle$ represents the energy eigenfunction of level $b$, as shown in Figure 2.8. Substituting this into equation 2.4.25, we obtain:

$$\langle\alpha_{ij}\rangle_{ab} = \alpha_{ij}^0\langle\psi_b|\psi_a\rangle + \sum_n \left(\frac{\partial\alpha_{ij}}{\partial q_n}\right)_0 \langle\psi_b|q_n|\psi_a\rangle \tag{2.4.26}$$

These energy eigenfunctions may be separated into a product; for example, for the initial state eigenfunction:

$$\psi_a = \prod_{n=1}^{Q} \phi_{a,n}(q_n, \nu_n^a) \tag{2.4.27}$$

where the number of normal modes $Q$ is given by $Q = 3N - 5$ for linear molecules and $Q = 3N - 6$ for nonlinear molecules, where $N$ is the number of atoms in the molecule, and $v_n$ is the vibrational quantum number. We then find that the first term becomes:

$$\langle\phi_{b,n}(q_n, \nu_n^b)|\phi_{a,n}(q_n, \nu_n^a)\rangle \tag{2.4.28}$$

and is a constant for $\nu_n^i = \nu_n^f$. This describes the Rayleigh scattering contribution. The second term is responsible for the Raman scattering contribution, and is zero for non-degenerate vibrations or if $\nu_n^a = \nu_n^b$. If $\nu_n^a = \nu_n^b \pm 1$, the integral is equal to $(\nu_n^a + 1)^{1/2}$. The intensity of the peaks is then attributed to the derivative $\frac{\partial\alpha_{ij}}{\partial q_n}$.

The intensity of the Raman line is determined by the population density in the initial level $E_i$, $N_i(E_i)$, the intensity of the excitation laser $I_0$ and the Raman scattering cross section $\sigma_{i\to f}$:

$$I_{Raman} = N_i(E_i)\sigma_{i\to f} I_0 \tag{2.4.29}$$

At thermal equilibrium, the population density follows the Boltzmann distribution:

$$N_i(E_i) = \frac{N}{Z} g_i e^{-E_i/kT} \tag{2.4.30}$$

with $N = \sum N_i$. $Z$ is the partition function, which depends on $g_i$ (the statistical weight factors). Stokes lines depend upon a transition which may begin at the

ground state while anti-Stokes lines depend on a transition where a molecule must begin in an excited state, and given that the population density in excited states is lower, the intensity of the anti-Stokes lines must be lower by a factor of $e^{-\hbar\omega_v/kT}$

The scattering cross section of the Raman spectrum allows us to measure the scattering efficiency of the Raman interaction. This is related to the polarizability; from the polarizability tensor given earlier, we may define the scattering cross section as [41]:

$$\sigma_{i\to f} = \frac{8\pi\omega_S^4}{9\hbar c^4}\left|\sum_j \frac{\langle\alpha_{ij}\rangle\vec{e_L}\langle\alpha_{jf}\rangle\vec{e_S}}{\omega_{ij}-\omega_L-i\gamma_j} + \frac{\langle\alpha_{ji}\rangle\vec{e_L}\langle\alpha_{ij}\rangle\vec{e_S}}{\omega jf-\omega_L-i\gamma_j}\right|^2 \tag{2.4.31}$$

where $\vec{e_L}$ and $\vec{e_S}$ are unit vectors of the polarisation of the incident laser beam and scattered light. The scattering cross section is therefore inversely proportional to the 4th power of the incident light wavelength; thus shorter wavelength light leads to a stronger Raman spectrum, although this can also excite fluorescence. Typically, a value of the scattering cross section may be $\sim 10^{-30}\,\mathrm{cm^2sr^{-1}}$, a very small value as opposed to fluorescence, which has typical cross sections of $\sim 10^{-18}\,\mathrm{cm^2sr^{-1}}$.

### 2.4.3 Assigning Raman modes

It is important to be able to identify and assign Raman peaks to corresponding Raman modes. The complex vibrations of a molecule may be described as the superposition of simple vibrations called the normal modes of vibration. The number of normal modes in a linear molecule with $N$ atoms is $3N-5$, and in a nonlinear molecule is $3N-6$, resulting from the translation of the whole molecule and the rotation of the molecule. The symmetry of these modes is determined by Group Theory. Some of the most common modes found in Raman spectroscopy are shown in Figure 2.9.

The Raman shift depends on the energy spacing of molecular modes, but not all of these modes are Raman active; as has been discussed, there must be a

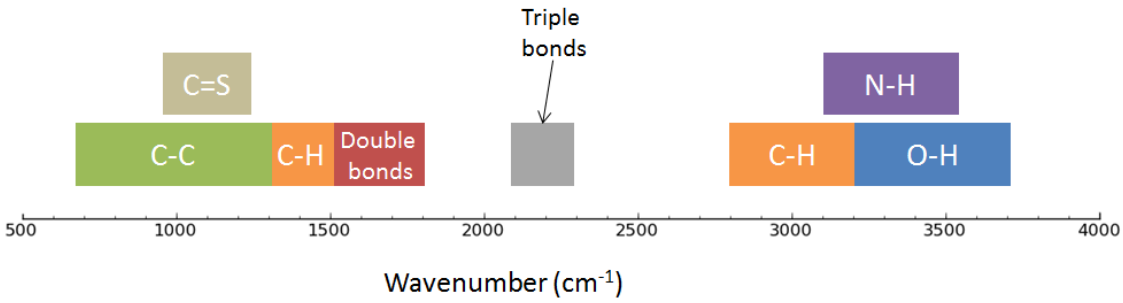


Figure 2.9: *Schematic of the Raman modes of common bonds in organic molecules*

Table 2.1: *Experimentally obtained Raman vibrational modes of calcite*

| Symmetry | Assignment | Raman shift ($cm^{-1}$) | | | |
|---|---|---|---|---|---|
| | | [42] | [43] | [44] | This study |
| $E_g + A_{1g}$ | Addition | 1748 | 1749 | 1754 | 1745 |
| $E_g$ | Asymmetric stretching | 1435 | 1437 | 1437 | 1437 |
| $A_{1g}$ | Symmetric stretching | 1085 | 1087 | 1092 | 1086 |
| $E_g$ | Asymmetric bending | 711 | 715 | 716 | 710 |
| $E_g$ | External rotation | 281 | 285 | 288 | 283 |
| $E_g$ | External translation | 155 | 162 | 162 | 161 |

change in polarizability $\alpha$. Raman spectroscopy tends to thus be best for polar molecules, which are molecules in which the bond moments do not cancel. The Raman modes for calcium carbonate, which is the focus of this thesis, are well defined, and shown in Table 2.1; schematics of the corresponding bond vibrations are shown in Figure 2.10. The strongest peak is the internal $CO_3$ stretching peak, which may be seen in the experimentally obtained (in this work) Raman spectrum in Figure 2.11. This peak, along with both the peaks due to asymmetric bending and stretching, are common to carbonates and are found in all the polymorphs, albeit shifted slightly. The external peaks are dependent on both the properties of the bond with the external atom and the structure of the polymorph.

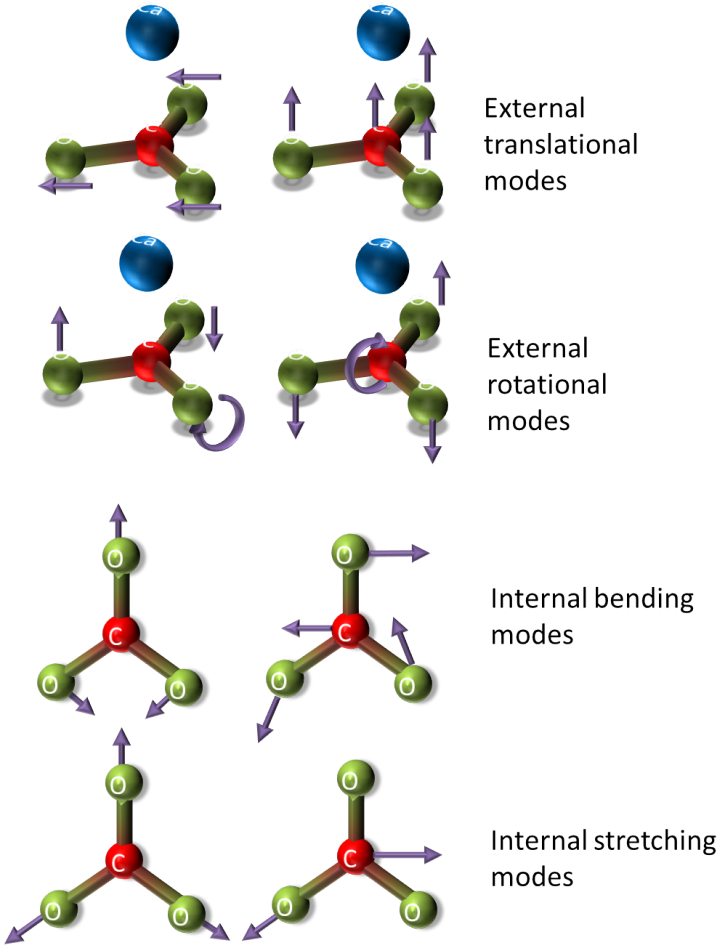


Figure 2.10: *Schematic of vibrations in carbonates*

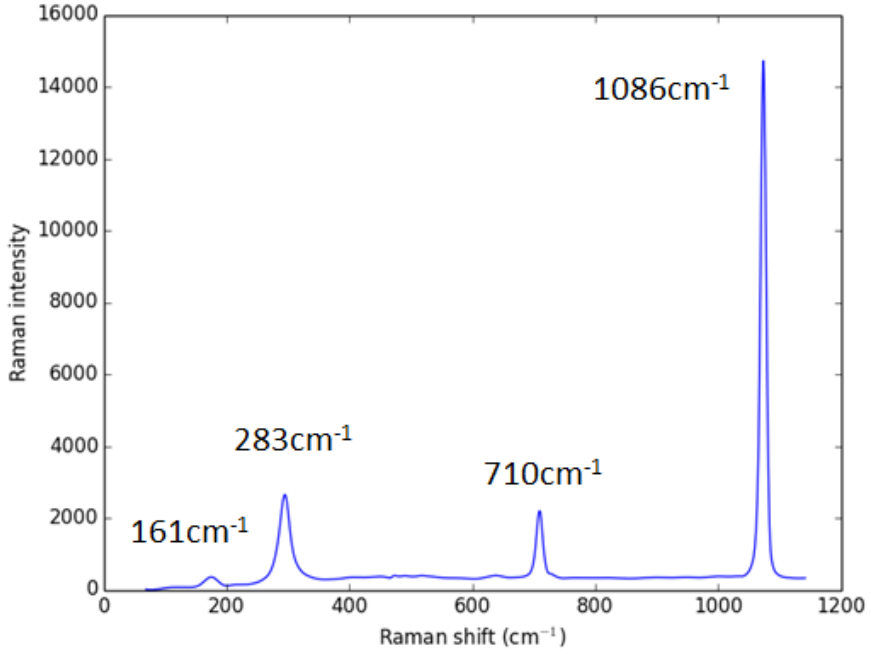


Figure 2.11: *An experimentally obtained Raman spectrum of a single calcite crystal, showing the relative strengths of the peaks*

### 2.4.4 Raman Tweezing

Raman spectroscopy is a powerful analytical tool, providing specific chemical fingerprints. Despite being a weak signal, it still finds many applications in the physical sciences as it does not decay over time, is non-invasive and easy to implement. For the analysis of colloidal suspensions, however, it is useful to be able to combine Raman spectroscopy with an immobilisation technique. An extremely non-invasive technique which can accomplish this is optical tweezing. This protects surfaces from any changes which could take place from chemical or physical immobilisation. Holding a particle in place over a period of time also allows a greater amount of signal averaging and hence an improved signal to noise ratio.

The combination of optical tweezers and Raman spectroscopy (or 'Raman tweezers') was first used by Carls et. al. on microdroplets [45]. The main uses of Raman tweezers are generally in the biological sciences, where the immobilisation of living specimens allows for faster Raman identification, and also reduces the need for cell

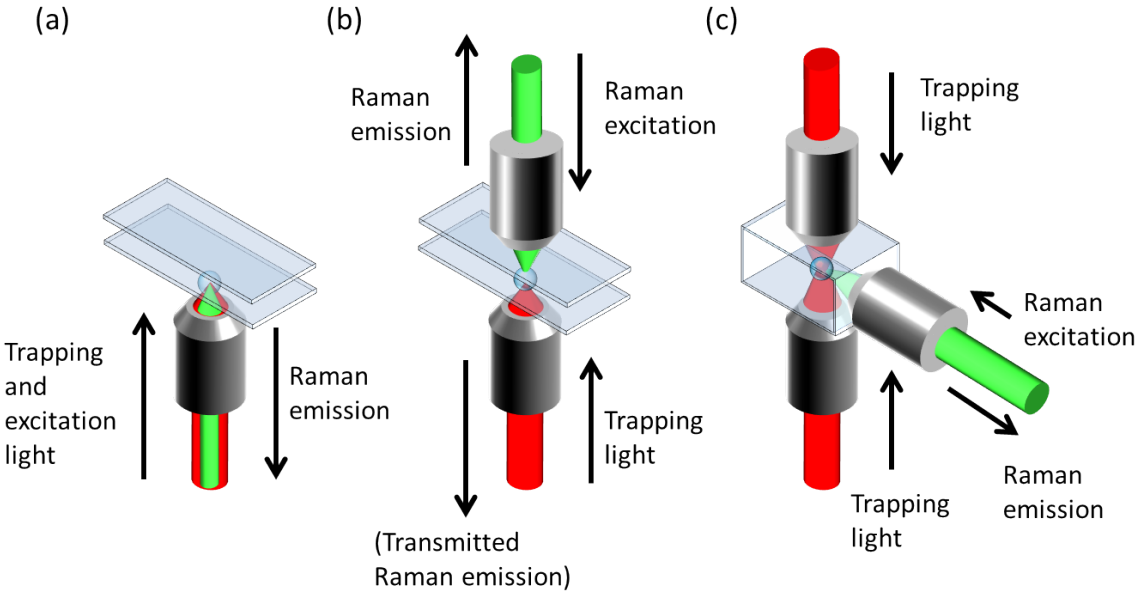


Figure 2.12: *Schematic depicting possible orientations for optical trapping, Raman excitation and Raman detection in Raman tweezer instrumentation*

labelling [46]. For example, they may be used to investigate trapped red and white blood cells [47], eukaryotic cells [48], and in distinguishing the type and growth phases of bacterial cells [49]. A limitation in the trapping of living specimens is the power of the trapping and/or Raman lasers; too much power or trapping for too long can cause heating and destroy the trapped cell.

Raman tweezers may also be used in chemical analysis, for example in polymerization reactions. Polystyrene is generally produced via emulsion polymerisation of styrene monomers, and it is useful for chemists to be able to probe the rate of this reaction and the effects of different concentrations of reactions [50]; through monitoring certain peaks in the spectrum over time, it is possible to obtain time dependent information on the reaction process. Raman tweezing has also been used in atmospheric chemistry, where it is useful to investigate individual microparticles. This has been achieved with capric acid droplets surrounded by ammonia gas [51]; spectra have been obtained which allow analysis of the growth of an ammonium salt layer around the droplets.

Raman tweezer setups generally consist of an optical tweezer setup with a Raman microscope incorporated. The same laser for trapping may be used for exciting the Raman spectrum, which is implemented in the simplest setups; however, it is also possible to trap a particle with one laser and use another laser to excite the spectrum. This means a higher power, longer wavelength laser can be used for trapping which leads to less heating, and lower power shorter wavelength lasers can be used for excitation, as the Raman intensity scales with the fourth power of the excitation frequency (as shown in equations 2.4.29 and 2.4.31 earlier). Figure 2.12 shows the possible orientations that may be used with dual laser Raman tweezer setups; Figure 2.12 a) demonstrates the example when the trapping and excitation beams both travel through the same objective, and the reflected Raman light from the specimen is collected through this objective. Alternatively, the excitation light may be directed from a different objective, as in Figure 2.12 (b), and the light is usually collected from the above objective for optimum collection efficiency. It is also possible to trap a bead with two counterpropagating laser beams, as shown in Figure 2.12 (c), which are generally more stable than single beam traps, although have the added complication of requiring very precise alignment; in this case we may excite the sample from the side and collect the light from the same objective. In this work, we use configuration (a) due to contraints from the dimensions of the microfluidic channel.

## 2.5 Surface Deposition

### 2.5.1 Dishwasher solutions

In a dishwasher, the presence of calcium or magnesium ions causes the phenomenon of 'hard water'. Dishwasher cleaning agents often contain sodium carbonate which is used to create an alkaline environment and remove grease. However, this reacts with the calcium and magnesium to produce metal carbonates. These precipitate out into the solution, contributing to filming on dishes.

Dishwasher fluids therefore contain several other chemicals to attempt to inhibit

or control this. One such group of chemicals are sulphonated polymers used to prevent precipitation via suspending any calcium carbonate formed. Also used are complexing agents, such as sodium tri-poly phosphate and methyl glycine diacetic acid, or MGDA and many others. These bind to calcium and magnesium ions, thus preventing them from reacting with any carbonate ions in the water and slowing down the formation of calcium carbonate.

There are also inhibitors which may be added to dishwasher detergents to inhibit the development of calcium carbonate. One such inhibitor is 1-hydroxyethane 1,1-diphosphonic acid (etidronic acid), or HEDP, which is phosphate based; however, this may lead to eutrophication (the promotion of algae growth, leading to fewer resources for other organisms) in aquatic ecosystems if used excessively.

Non-ionic surfactants are used to lower the surface tension of the water to encourage water to dry uniformly on surfaces. They also help remove fatty soils. Fillers such as sodium sulphate are also used in powdered formulations, though these do not contribute to the washing or filming.

### 2.5.2 Polymorphs and Crystallization mechanisms of calcium carbonate

Calcium carbonate, one of the most common forms of minerals, has been subject to much research. Solid calcium carbonate has several different phases found in nature; amorphous calcium carbonate, two hydrated forms (hexahydrate and monohydrate), and three crystal polymorphs. The amorphous and hydrated forms are unstable and generally transform into calcite; the latter two are stable if kept at low temperatures. SEM images of the crystal forms are shown in Figure 2.13. The most common of these is calcite, with a hexagonal crystal structure. Less common is aragonite, with an orthorhombic rod-like structure, and finally vaterite, which is the least common and forms spheroidal crystallites. These polymorphs may be created artificially in a laboratory setting [52], although they also occur naturally.

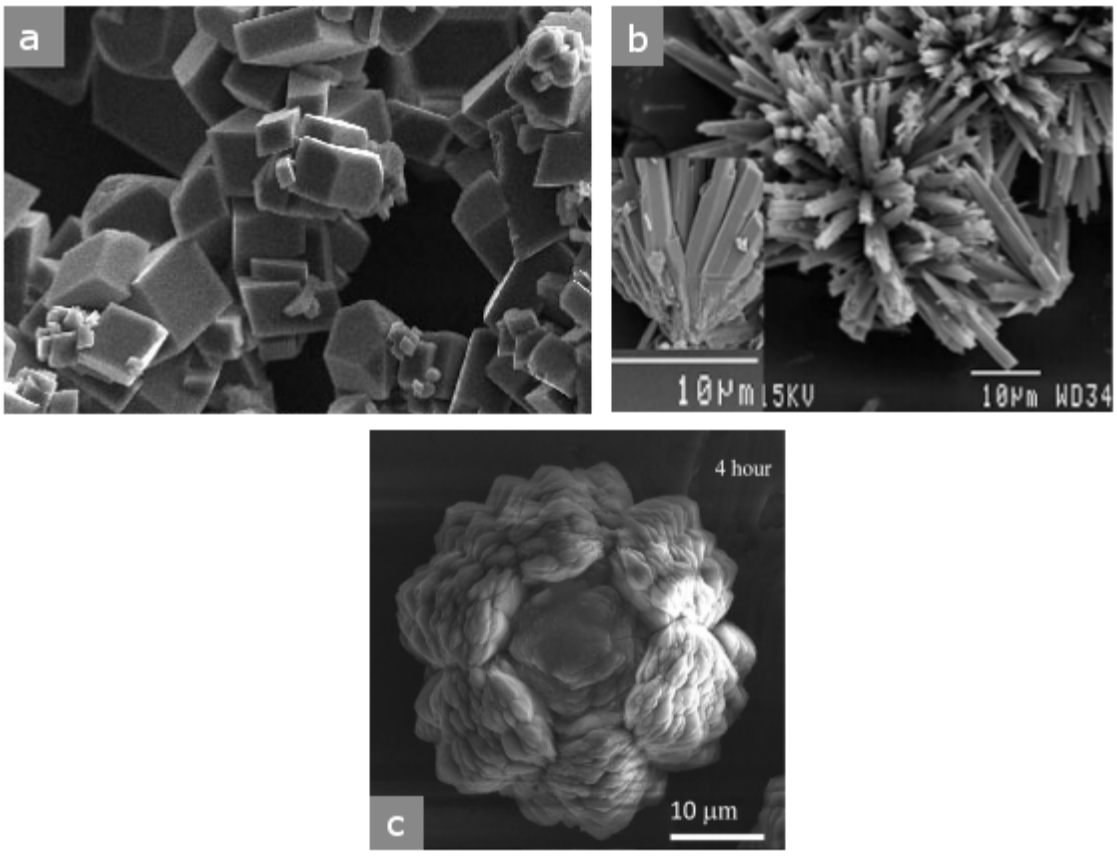


Figure 2.13: *SEM images of the three polymorphs of calcium carbonate: (a) calcite [4], (b) aragonite [5] and (c) vaterite [6]*

Amorphous calcium carbonate (ACC) precipitate has a disordered structure and is unstable, and as a precipitate appears as spherical particles with a diameter in the range 50-400 nm [53]. At room temperature in a supersaturated solution, precipitates are formed spontaneously; these progress through unstable, metastable and stable stages, with ACC being formed in the unstable region. This rapidly converts into a more stable polymorph. It may convert into calcite directly, or via a two stage process of forming vaterite which then transforms into calcite through recrystallizing; this quickly converts to vaterite and calcite.

Calcite is the most stable polymorph of calcium carbonate and aside from being created in dishwashers, it forms naturally in caverns as stalactites and stalagmites, and is found in marine organisms. Calcite also has interesting optical properties as it is strongly birefringent. The thermal and chemical conditions which lead to the formation of these polymorphs have been studied extensively [54]. Temperature is a factor in calcium carbonate crystallisation. At low temperatures calcite is the most stable polymorph that forms; with increasing temperature the formation of aragonite is observed at 40 °C and at higher temperatures dominates. The transformation of calcite to aragonite may be quite complicated, as vaterite may also be formed in the metastable stage. Therefore at the higher temperatures in dishwashers where calcium carbonate is formed, we may expect a mixture of polymorphs to appear. It is also possible that the surface properties of the materials in a dishwasher play a part in the polymorphs which adsorb to them.

## 2.6 Microfluidics

Microfluidic platforms consist of liquid handling structures of the order of micrometres in cross-section. These have become extremely valuable devices in the last few years for several reasons. Firstly, they use low liquid volumes meaning there is less waste. They also give a high degree of control of chemical reactions. The rate of flow in a microfluidic device may be controlled by altering the size of the channel and the input flow rate, which may be delivered through a number of

methods.

### 2.6.1 Modelling flow rate in a microfluidic channel

The flow in a microfluidic channel may be predicted using simple fluid mechanics. The idea of internal friction in fluids was first conceived in 1851 by George Gabriel Stokes [55] and later defined as the Reynolds number by Osborne Reynolds [56]. The Reynolds number is a dimensionless quantity defined as the ratio of inertial forces to viscous forces, and may be used to determine if flow in a system is laminar, that is, the flow propagates via thin sheets, in which case the Reynolds number is less than unity, or turbulent flow, where the flow is dominated by inertial fluid forces and tends to produce instabilities.

The Reynolds number of a fluid flowing through a uniform tube is defined as:

$$Re = \frac{\rho \overline{v} D_H}{\mu} = \frac{Q D_H}{\nu A} \tag{2.6.32}$$

where $\rho$ is the density of the fluid (kg/m$^3$), $\overline{v}$ is the mean fluid velocity (m/s), $D_H$ is the hydraulic diameter of the tube (m), $\mu$ is the dynamic viscosity of the fluid (kg/(m·s)), $Q$ is the volumetric flow rate (m$^3$/s), $\nu$ is the kinematic viscosity of the fluid (m$^2$/s) and $A$ is the tube cross sectional area (m$^2$). The hydraulic diameter $D_H$ varies depending on the shape of the channel cross-section. For a rectangular channel, $D_H = 4A/P$ where $P$ is the 'wetted perimeter' of the channel, that is, the perimeter of the channel which the fluid is in contact with.

We may model the speed of the fluid flow through the channel from this if we know the syringe pump flow rate and the microfluidic channel dimensions. The 500 $\mu$m wide flow channels used described in Chapter 3, for instance, have a cross sectional area of $2.3 \times 10^{-8}$ m$^2$, and for a fluid flow rate of 0.07 $\mu$L/hr and channel of internal volume 1 $\mu$L (as used in this work), the Reynolds number is calculated to be 0.08, which indicates non turbulent flow. This is necessary as turbulent flow could cause a bead to fall out of a trap; in fact, this was found to be the maximum flow rate

at which beads remained trapped, which is further explored in Chapter 4 of this thesis.

### 2.6.2 Pumping and heating in microfluidic channels

The use of microfluidic channels stems from the ability to transport a fluid volume through them. There are several ways in which to do this, which are classified as either displacement or dynamic pumping methods. Displacement methods work via the creation of a pressure difference between the two ends of the channel via the exertion of forces on the fluid. Dynamic methods involve adding energy to the working fluid and thus changing its momentum or pressure directly.

One of the most common and simple displacement pumping methods is syringe pumping, which involve the use of a mechanical stepper motor to drive the motion of the syringe piston, which is attached to the channel through tubing. Given that the movement is linear, we have a wide range of control over the speed of flow via changing either the speed at which the piston is driven or by changing the size of the syringe. Syringe pumps are commonly used because they are easy to set up and more recent pumps have high flow stabilities. The amount of dispensed liquid is easy to calculate after the experiment has taken place and they are capable of high flow pressures. However, there are some drawbacks. The stepper motor motion is oscillatory, and this is more evident at lower flow rates. Another method of displacement flow is peristaltic pumping, which involves squeezing flexible tubing carrying the fluid via the use of a motor. These are easy to set up and any amount of fluid can be dispensed; they also allow recirculation of fluid. However, there are strong pulses in the flow rate due to the squeezing actions involved, and the tubing can age and reduce reliability. Gas pressure driven pumping [57] and gravity driven flow [58] have also been used to good effect.

Another method of pumping is electro-osmotic pumping. Electro-osmotic pumping is popular in cases where constant pulse-free flows are required, as there are no moving parts. This type of pumping works via movement of uncharged liquid

relative to a stationary charged surface due to an externally electrically applied field [59]. As such, the flow rate and direction of flow are highly controllable through changing the applied electric field. However, this type of pumping may be a disadvantage if there are chemical reactions taking place with ions, as it may affect the reaction. In this work, we use syringe pumping, owing to the large range of possible flow rates, the speed at which solutions may be introduced to the microfluidic channel, and the fact that samples are unaffected by this flow method aside from being moved through the channel.

For certain microfluidic chemical reactions to take place, it may be necessary to introduce controlled heating into the channel. There are several methods for microfluidic heating [60]. One of the simplest methods is to heat the liquid externally, for example on a hot plate prior to the liquid entering the channel. However, this method may not be suitable if the reaction needs to be visualised while heating happens in situ. Integrated and semi-integrated heating methods provide greater on-chip temperature control. One such method is the use of heaters placed directly onto (that is, in thermal contact with) the microfluidic chip. Peltier heaters may be used to give constant heating across the channel; two may be used on the same chip to produce a temperature gradient. A more in situ method of heating is to use nearby 'heater' channels with hot liquid flowing through. This may be achieved through initiating an exothermic reaction in the heater channels, such as that between water and sulphuric acid, and conversely cooling may be achieved through an endothermic reaction such as that between air and acetone [61]. It is also possible to directly heat the liquid via electromagnetic radiation. This has been achieved with microwaves [62].

In this work, an on-channel method of heating is utilised by means of a power resistor kept in thermal contact with the channel and a thermistor in thermal contact with the channel, which is used to limit the maximum temperature of the resistor. This is used as it is a stationary method and provides a high degree of external control over the temperature. It is also a relatively fast method, as the

resistor itself heats to the required temperature in a matter of seconds (although a timescale of a few minutes is necessary to heat the channel to temperature), and is easy to incorporate into the setup. Samples are heated before entering the channel through the use of a hot plate as it was found that liquids in the channel itself take a while to heat to temperature; the resistor is therefore used as more to maintain the temperature of samples rather than heat to temperature for maximum time efficiency.

# Chapter 3

# Methodology and Raman Tweezer Instrumentation

*This chapter describes the development of the bespoke Raman Tweezer system built for the investigation of dishwasher solutions, and details the instrument calibrations and experimental methodologies employed.*

## 3.1 Raman Tweezers

### 3.1.1 Basic Tweezer setup

A bespoke Raman tweezing setup was built as shown in Figures 3.1 and 3.2. A 1 W maximum power adjustable output 1064 nm Nd:YAG laser (Model DTL-322, Laser Export Co.) was used for optical trapping. The beam was expanded onto a phase only reflective Holoeye PLUTO spatial light modulator ($SLM_{1064}$) with a resolution of 1920x1080 pixels (FHD) via a Galilean telescope lens arrangement ($L_1$ and $L_2$), resized by a Keplerian telescope arrangement ($L_3$ and $L_4$) reflected by the dichroic mirror ($DM_1$) which reflected light above 1000 nm and transmitted all other wavelengths to join the 532 nm laser beam. The 532 nm laser was a 50 mW output power frequency doubled Nd:YAG laser (Model LD-WL206, Changchun New Industries) and was used for excitation of Raman spectra at a power of a few milliwatts at the sample. The 532 nm laser was aligned in such a way that it could

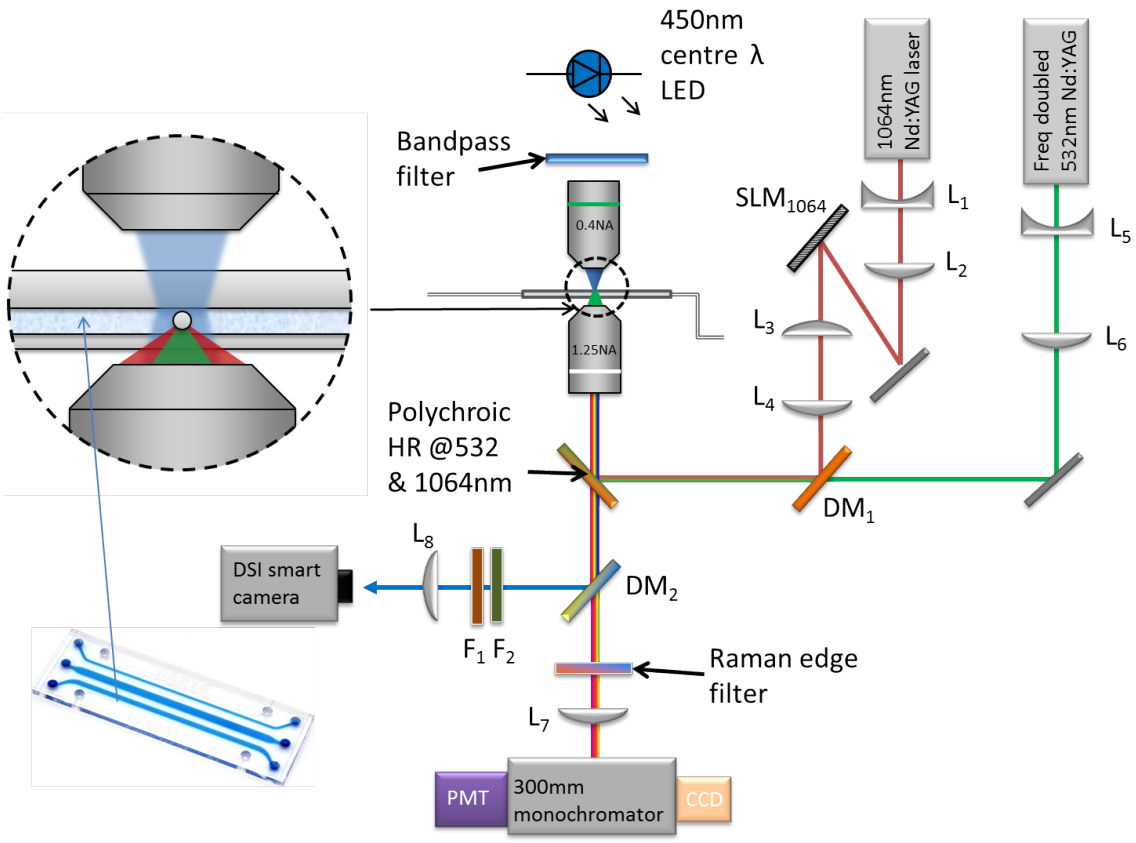


Figure 3.1: *Schematic of the optical trapping and Raman excitation setup. Inset: a close-up of the light paths of each laser through the microscope objective*

also be used for trapping, and was expanded by another Galilean telescope lens arrangement ($L_5$ and $L_6$) and aligned along the same path as the 1064 nm laser through dichroic mirror $DM_1$ which transmitted the 532 nm light.

Both beams were then steered vertically to overfill the back aperture of a 100x infinity corrected oil immersion Nikon microscope objective with a numerical aperture NA=1.25 using a custom made polychroic mirror (Chroma) designed to reflect both 532 nm and 1064 nm light and transmit all other wavelengths. The back-scattered light from the objective passed through the polychroic and was reflected off a steering mirror onto a dichroic ($DM_2$) which reflected light at wavelengths below 500 nm and transmitted all other light. The transmitted light passed through a 532 nm Raman edge filter (Laser 2000) and was focussed by lens $L_7$ onto a 200 $\mu$m diameter 0.22 NA patch fibre (Thorlabs) which was carried through the

fibre to the monochromator entrance slit. The monochromator was an Omni-$\lambda$300 monochromator (Zolix) with a triple grating turret (with gratings of 2400 lines/mm, 1200 lines/mm and 600 lines/mm), with continuously adjustable entrance/exit slit widths from 0-3 mm and a focal length of 300 mm. The grating dispersed light was collected by an open electrode 1024×256 pixel linear array CCD (GPL-3011-OE, Gilden Photonics) cooled to -55 °C from which images were obtained and full vertical binning was used to build the spectrum.

Given that the system both tracks particle position and takes Raman spectra, it is important to optimise the illumination light but prevent the wavelength of this light interfering with the very small levels of Raman light we wish to collect; it is also helpful when trapping to be able to see the trapped specimen in real time to check that the specimen is still trapped. The spectral response of the camera sensor is shown in the appendix, showing that the sensor still detects light at lower wavelengths; the light source however must be bright enough to still be detected. The illumination light was a 1W blue LED with a centre wavelength of 450 nm. This was focussed onto the sample by means of a small optical system, in which the light was focussed by a 25 mm focal length lens after the LED, through a $(470 \pm 10)$ nm bandpass filter and into a 10x 0.25 NA objective lens. The light transmitted through the sample passed through the polychroic mirror (PM) and was reflected by the dichroic mirror ($DM_2$), hence blocking this light from passing to the fibre, and focussed through a tube lens ($L_8$) onto a CMOS smart camera built by Durham Smart Imaging [63]. Two filters ($F_1$ and $F_2$) were used to block any 1064 nm and 532 nm light which had passed through both the polychroic and dichroic.

Particles were trapped in a thin-bottomed (145 $\mu$m bottom thickness) microfluidic flow slide (Micronit Microfluidics), as shown in the schematic in Figure 6.3 (Chapter 6). The microreactor had a total internal volume of 1 $\mu$L and a channel length of 42 mm. These were attached via PTFE tubing to a syringe pump (NE-300 Just Infusion Syringe Pump, New Era pumps systems), capable of various flow

rates depending on the size of syringe used. Typical flow rates from 0.01 ml/h to 0.1 ml/h were used. While there was some flow oscillation at these low flow rates, it was usually not enough to displace particles from their trapped positions sufficiently for them to escape the trap, and constant enough that over the timescales where readings were taken there would not be a noticeable change.

## 3.2 Detecting the Raman emission

Two different detection methods were used for obtaining Raman spectra; a Thorlabs PMT002 photomultiplier, and a CCD camera from Gilden Photonics. We used the CCD in most cases in this work as it was possible to gain more spectral information in a shorter amount of time. The Raman spectrometer system was calibrated using toluene, a common Raman standard as it has several strong Raman peaks. From Figure 3.3, we can see that the spectrum has the characteristic peaks we would expect [64]. This spectrum may be used to calibrate other spectra to the correct Raman shift values, and may also be used to calculate the scattering cross section comparing to known values of the differential scattering cross section for toluene. This is given by:

$$N\frac{d\sigma}{d\Omega} = \frac{I_R}{F} = \frac{k'hc^4\nu_s^4}{8\pi^2(\nu_p - \nu_s)(1 - \exp(\frac{-h(\nu_p-\nu_s}{kT}))} \tag{3.2.1}$$

where $F$ is the intensity of the pump beam, $I_R$ is the output Stokes intensities, $N$ is the scattering molecular number, $k'$ is a constant for a given material and $\nu_s$ and $\nu_p$ are the Stokes and pump frequencies respectively. For toluene, the differential cross section is given as $1.1 \times 10^{-8}\,\mathrm{cm}^{-1}\mathrm{sr}^{-1}$ at a pump wavelength 694.3 nm for the peak at $1002\,\mathrm{cm}^{-1}$ [65]. At a pump wavelength of 532 nm this value is $3.41 \times 10^{-8}\,\mathrm{cm}^{-1}\mathrm{sr}^{-1}$.

In this thesis, it is necessary to be able to correctly identify the Raman spectrum of calcium carbonate. Spectra were compared to that of a sample of calcite crystals (Sigma C6767). Figure 3.4 shows the results of Raman detection of a reference calcite cube. This was achieved through flowing water mixed with the calcite powder

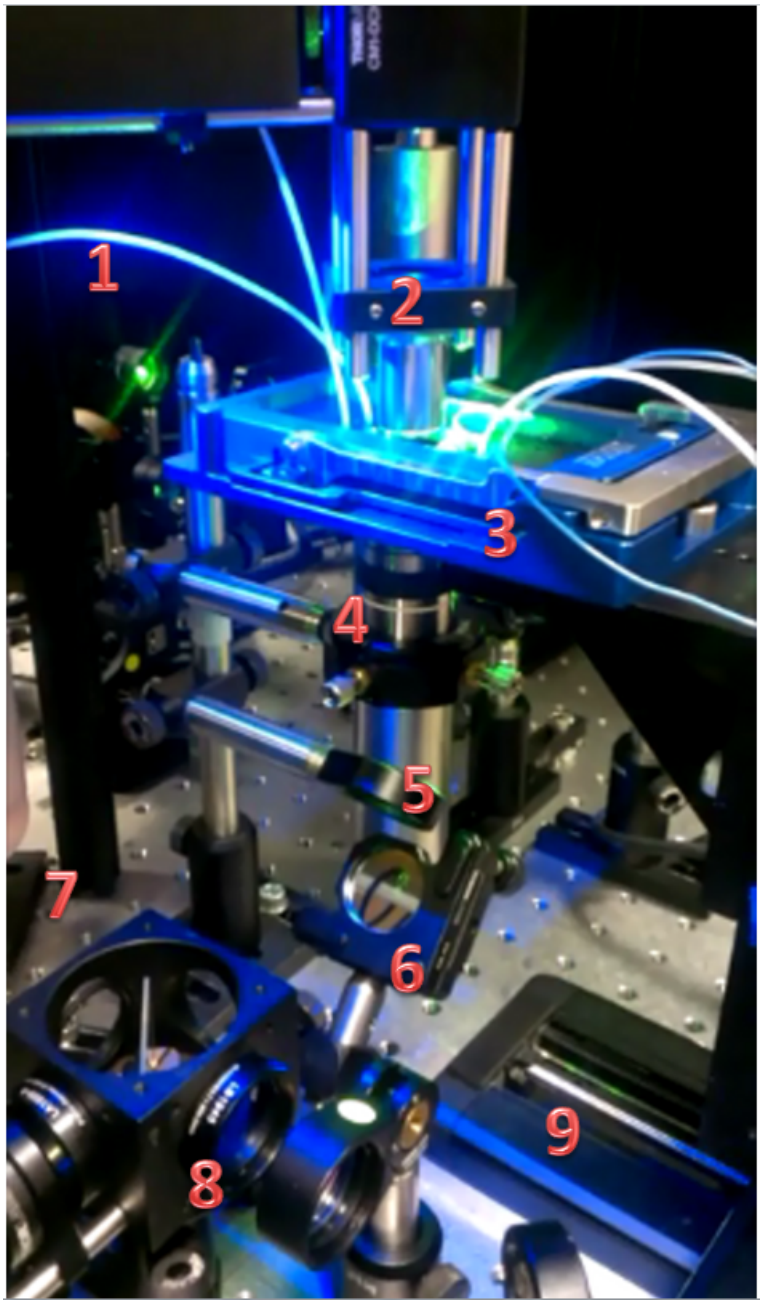


Figure 3.2: *Photograph of the experimental setup, depicting: 1. Pipe feed to channel, 2. illumination light being focussed by a 10x microscope objective, 3. the microfluidic channel in a sample holder (providing a liquid-tight connection), 4. the 1.25 NA trapping/Raman objective, 5. Polychroic mirror reflecting 1064 nm and 532 nm light and allowing all other light to pass, 6. Steering mirror for illumination and Raman light, 7. Dichroic mirror passing $>$ 500 nm light to the Raman optics and $<$ 500 nm light to the camera, 8. Tube lens to focus light onto detector and shortpass filters to block residual laser light, 9. Sigma-Koki computer controlled microscope stage for precise stage position control*

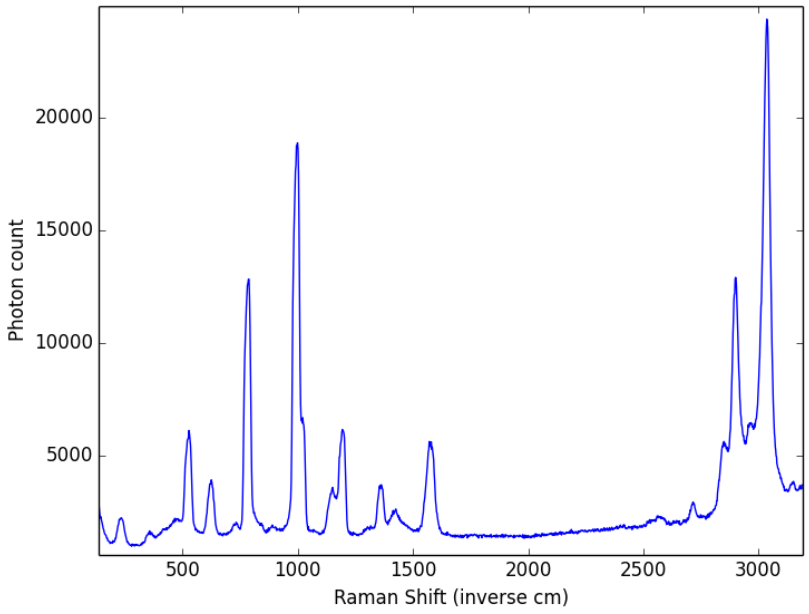


Figure 3.3: *The Raman spectrum of toluene flown through the microfluidic channel. Characteristic peaks are present at 521 $cm^{-1}$, 786.5 $cm^{-1}$, 1003.6 $cm^{-1}$, 1211 $cm^{-1}$, 1605 $cm^{-1}$ and 3057 $cm^{-1}$*

in one of the channels across the 532 nm excitation beam then drying the channel. As shown, calcite can easily be detected from the 1086 $cm^{-1}$ peak in a square area, roughly the same as the size of the crystal itself. The external rotational and translational bonds at 281 $cm^{-1}$ and 155 $cm^{-1}$ were also present, confirming the polymorph as calcite. It is important to be able to identify background spectra to be able to gauge the effect they may have on obtained spectra, especially in optical tweezers Raman spectroscopy which is typically used for the analysis of very small items. Figure 3.5 shows the Raman spectrum of a trapped PMMA bead, which is the one of the primary background spectra obtained due to the strong polymer peaks. Figure 3.6 shows the Raman spectra of water and glass (taken with the excitation beam at the centre of a water-filled channel and in the channel glass respectively), which also contribute to the background. Glass and water have broad, fairly weak Raman spectra in the fingerprint region from 500-2000 $cm^{-1}$ (water also has a strong peak at around 3000 $cm^{-1}$ due to O-H stretching [66] and glass has a fairly strong peak at around 500 $cm^{-1}$ due to Si-O bending [67]). The Raman

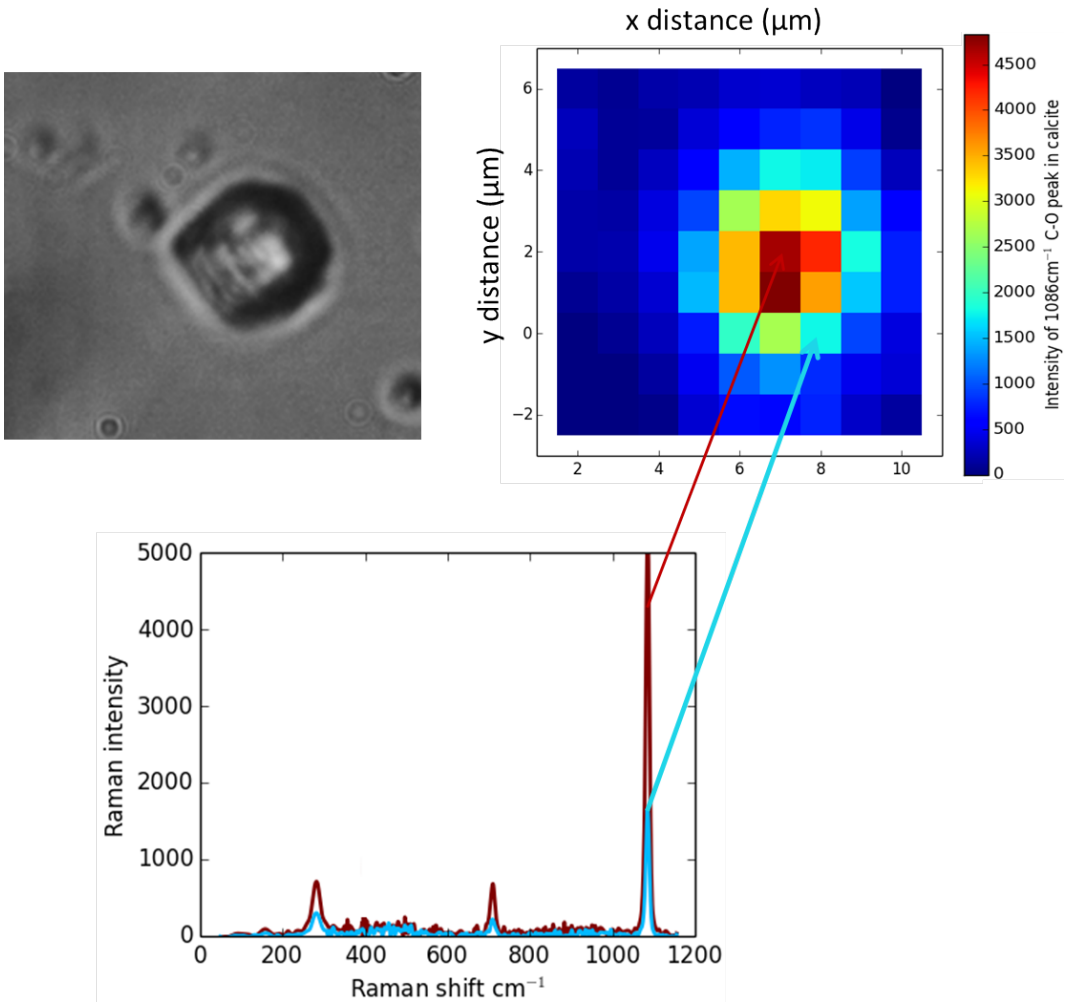


Figure 3.4: *Map depicting the intensity of the strong 1086 $cm^{-1}$ carbonate peak at several positions around a sample calcite crystal, using an integration time of 10 seconds. The intensity is strongest in a square region approximately equal to the size of the crystal*

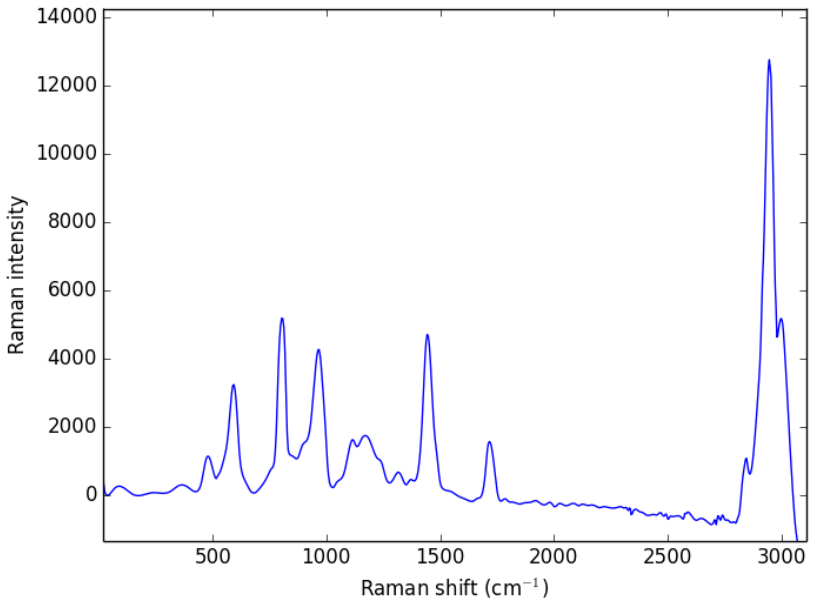


Figure 3.5:
*The background subtracted Raman spectrum of a trapped polymethylmethacrylate bead, taken over an integration time of 10 seconds*

spectra of these background sources were not anticipated to be an issue due to the excitation beam being focussed on the sample rather than the water and glass, and also due to the primary spectral region of interest being in the fingerprint region.

However, while the Raman spectra of the background sources may not be an issue, it was found that when the water flow was initiated, a very strong wide peak was obtained in the fingerprint region, which is characteristic of fluorescence. The effect of this wide peak on useful Raman peaks is demonstrated in Figure 3.7, where the water flow causes significant changes to the heights of important peaks and hence contributes a major source of noise. Given that this peak was only found when water was flowing, it was assumed this was from either the water or the glass fluorescing due to the high laser powers used to obtain the Raman spectrum of small amounts of materials; this was further insinuated by the decay of this peak over time when the flow was stopped, suggesting photobleaching was taking place. The fluorescence peak was significantly diminished when the channel was purged of water, suggesting that the fluorescence of the water was responsible

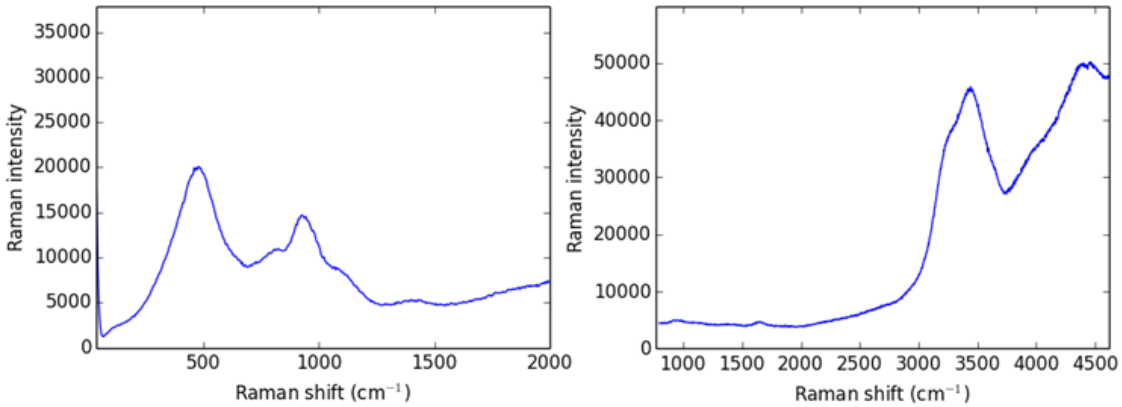


Figure 3.6: *The representative Raman spectra of glass (left) and water (right), taken over an integration time of 5 seconds*

for the majority of the total fluorescence background.

From Figure 3.7, we can also see that the fluorescence intensity is related to whether the water flow is on or off, meaning that this actually serves as a method of measuring the flow. However, it is not useful for taking Raman spectra, as it is no longer sufficient to subtract a constant baseline as the background changes. In Raman spectroscopy, obscuring of the Raman spectrum by a background spectrum is a common problem [68] and arises from sources such as fluorescence or exterior sources such as room lights. This has the effect of introducing noise into the Raman spectrum, and is a nuisance when it is necessary to take several spectra over time. Therefore a good method of subtracting the fluorescence background is necessary.

Computationally, there are several ways to estimate the spectrum. We used an automated background subtraction method previously reported by [69], where the background $B(\nu)$ is estimated from the measured spectrum $S(\nu)$. The known contaminant contributions such as glass are measured ($X(\nu)$) and then the concentration estimated ($C_{guess}$). The background is then modelled at iteration $i$ as:

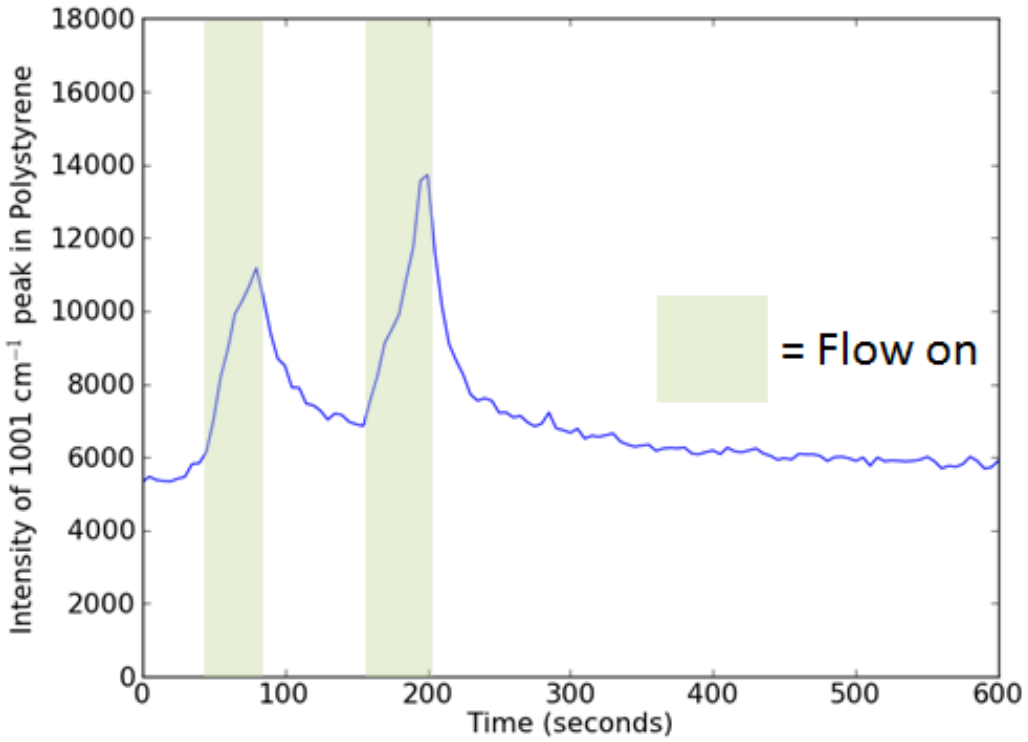


Figure 3.7:
*Graph showing the change in intensity of the 1001 $cm^{-1}$ peak in polystyrene over time as the water flow through the microfluidic channel is switched on and off. This change in intensity is in fact present over all Raman shifts and is due to the fluorescence of the flowing water*

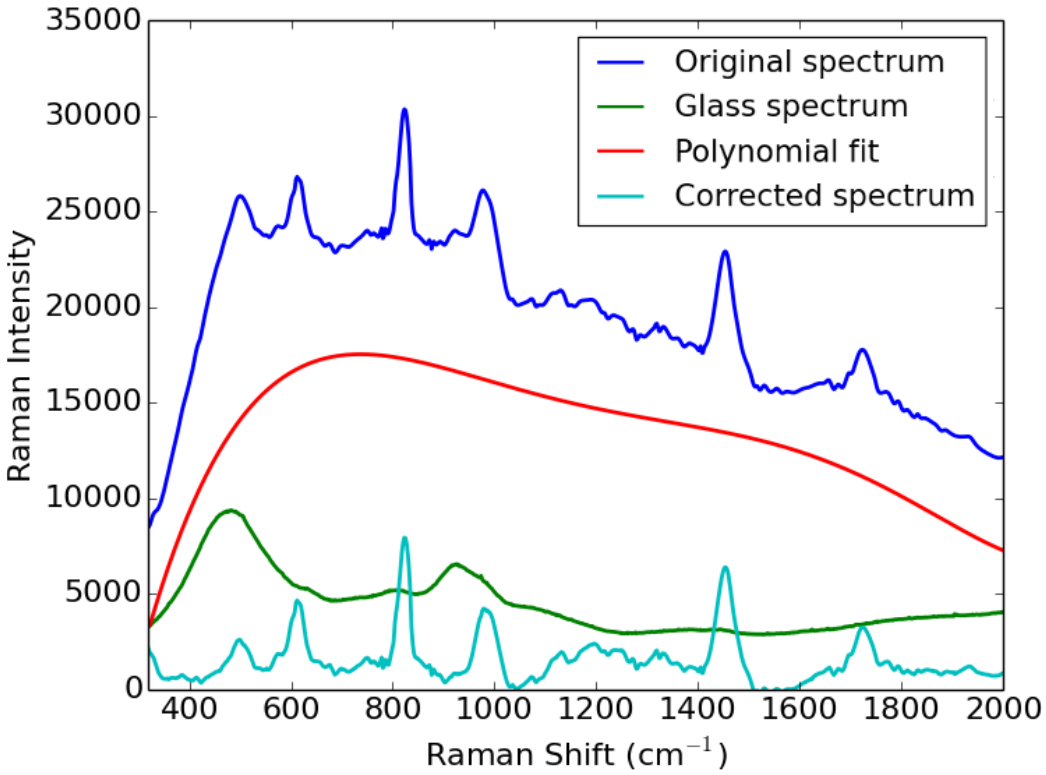


Figure 3.8: *An example of the background fitting procedure for a trapped 3 $\mu$m diameter PMMA bead in water, showing the original spectrum, glass spectrum, the simulated 5th order polynomial fit to the fluorescence background and the final background corrected spectrum*

$$B_i(\nu) = C_i X(\nu) + P_i(\nu) \tag{3.2.2}$$

where $C_i$ is the value of $C_{guess}$ at iteration $i$ and $P_i(\nu)$ is a polynomial fit to:

$$P_i(\nu) = B_i(\nu) - C_i X(\nu) \tag{3.2.3}$$

A merit function $M$ is defined as the sum of the squares of the residuals of the polynomial fit, $P_{resid}$, and $C_{guess}$ and the polynomial fit are varied to minimize $M$. Raman features are then clipped from the spectrum to give $_{i+1}$. The process is repeated until:

$$|B_{i+1} - B_i|^2 < \epsilon \tag{3.2.4}$$

where $\epsilon$ is a user defined minimum threshold. This is performed on each experimentally obtained spectrum.

It is also possible to reduce the fluorescence background experimentally. Examples reported previously have included the use of gated cameras [70] and the use of multiple excitation frequencies [71], which takes advantage of the static nature of the fluorescence signal as opposed to the Raman signal. In this experiment, we have the advantage of being able to also move the excited specimen via optical trapping; it is possible to move a bead at a certain frequency and detect the Raman signal at this frequency through the use of a faster detection method than a CCD, for example with a photomultiplier. A phase sensitive detection method has previously been reported in [72], and was implemented in this experiment in an attempt to reduce the overwhelming background contributions. A photomultiplier tube (PMT002, Thorlabs Inc.) was aligned to collect light from the second exit port of the monochromator. A chopper was placed first in front of the 532 nm laser and set to chop the beam at 500 Hz. The laser light was then modulated and the resulting modulated Raman light was detected by the photomultiplier. The photomultiplier output was connected to a lock-in amplifier, which had the reference input connected to the chopper frequency reference output. As the monochroma-

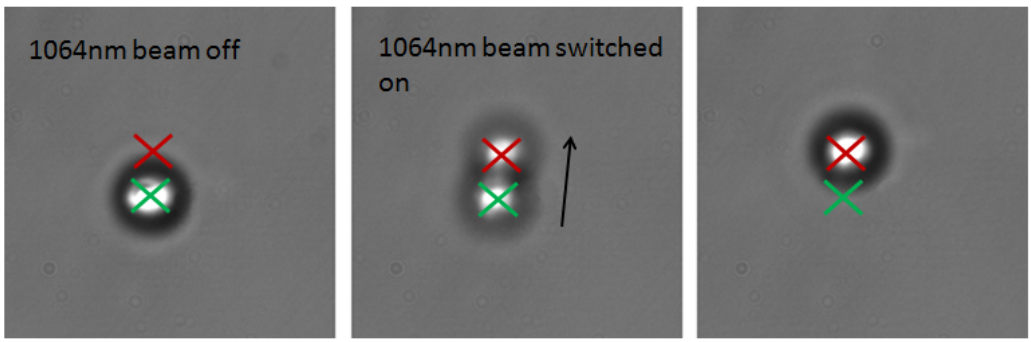


Figure 3.9: *Image of a three micron bead trapped by an optical trap at 532 nm (lower trap) and 1064 nm (upper trap). The upper trap is modulated at a frequency of 30Hz and thus the bead jumps between the two traps. The 1064 nm beam is set at a higher power than the 532 nm beam to ensure the bead preferentially jumps to this trap*

tor was scanned from 500-700 nm in one second intervals, the output voltage from the lock in amplifier was recorded using software written in LabVIEW for this experiment for both controlling the monochromator and obtaining the spectrum. This was then used to calibrate the monochromator and PMT using toluene. A spectrum was thus obtained which was free from noise not related to the 532 nm laser excitation source.

The chopper was then placed in front of the 1064 nm laser and set at a lower frequency of 30 Hz. The position of the 1064 nm laser was shifted so as to reduce the green-stimulated Raman signal from the trapped specimen to zero. As the 1064 nm laser is chopped, the bead jumps between the 1064 nm laser and the 532 nm laser traps, as shown in Figure 3.9. The monochromator was scanned from 500-700 nm in 0.5 nm steps again to obtain a background free signal, as signals were only obtained when the bead was in the green trap. This was then attempted with solution present, and scanned over a wavelength range of 6 nm in steps of 0.1 nm in one second intervals.

## 3.3 Detecting the high frequency motion changes

Given we wish to map the high frequency motion of our trapped bead to monitor its environment, it is necessary to use a camera with a high frame rate. The camera used in this experiment is a smart camera built by Durham Smart Imaging (DSi) [63], with a VGA (640 x 480) resolution. The camera is capable to tracking particle position in real time, allowing for probing of the particle power spectrum and data acquisition during image acquisition.

Images are taken by a high speed CMOS sensor, which splits the images into two paths. One displays the image and the other processes the tracked region through use of an on-board centroiding algorithm to give a dataset of $x$ and $y$ positions from the corner of a selected region over time for thresholded particle areas on the sensor. Up to 16 of these regions may be selected on the camera. A window of interest may be selected, and the size of this window determines the frequency of position measurements taken. For example, a window of 100 by 100 pixels gives a frame rate of around 5000 Hz.

Figure 3.10 shows the power spectra obtained when the laser power is changed. From this we can see that increasing the laser power increases the corner frequency and hence the trap stiffness, as we would expect given that increased laser intensity increases the trapping force towards the centre (as described in Equation 2.3.14). As we will be trapping items in flow, it is important to trap particles with a high enough trapping power to prevent beads being pushed out of a trap by the force of the liquid flowing past. The trapping power must, however, be limited, as this can contribute to particulate build-up on a bead [73].

It is also necessary to be able to model the bead motion in a trap when there is fluid flow, as the flow will contribute to the movement of the particle. Figure 3.11 shows the experimentally obtained change in the particle position histogram for a trapped 3 $\mu$m diameter PMMA bead at different fluid flow rates from the syringe pump. In this case the flow was in the $+x$ direction, and we can see that the

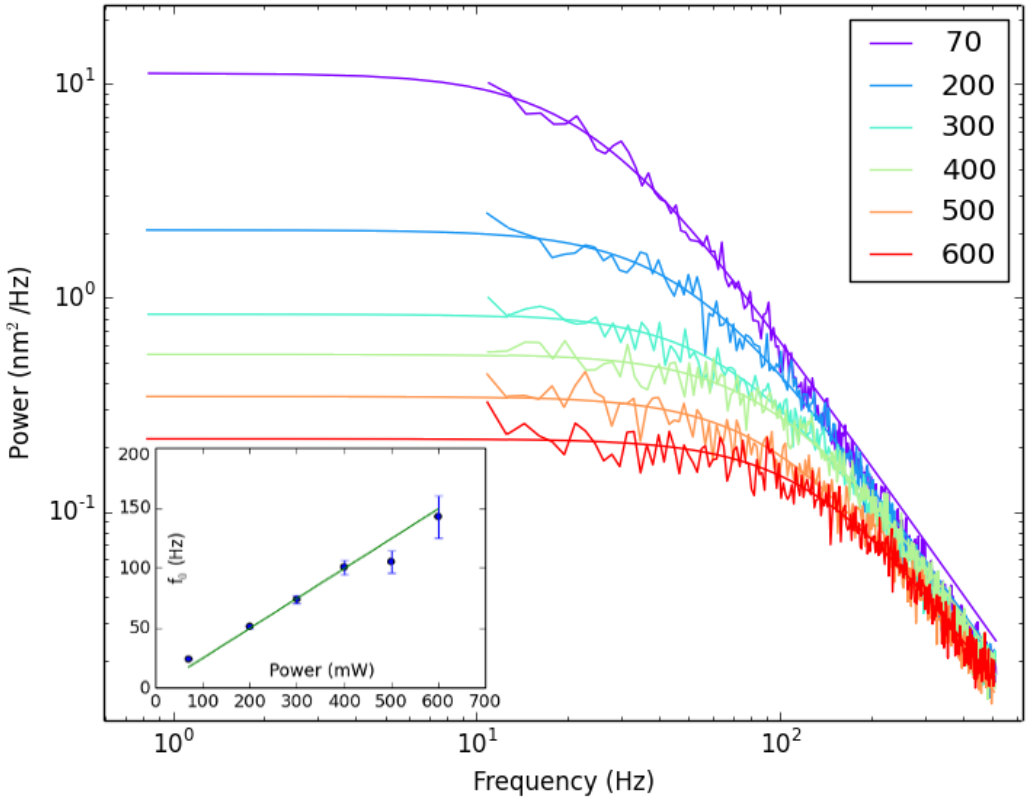


Figure 3.10: *Power spectra at different laser power output settings. Inset: linear relationship between laser power and corner frequency,* $f_0$

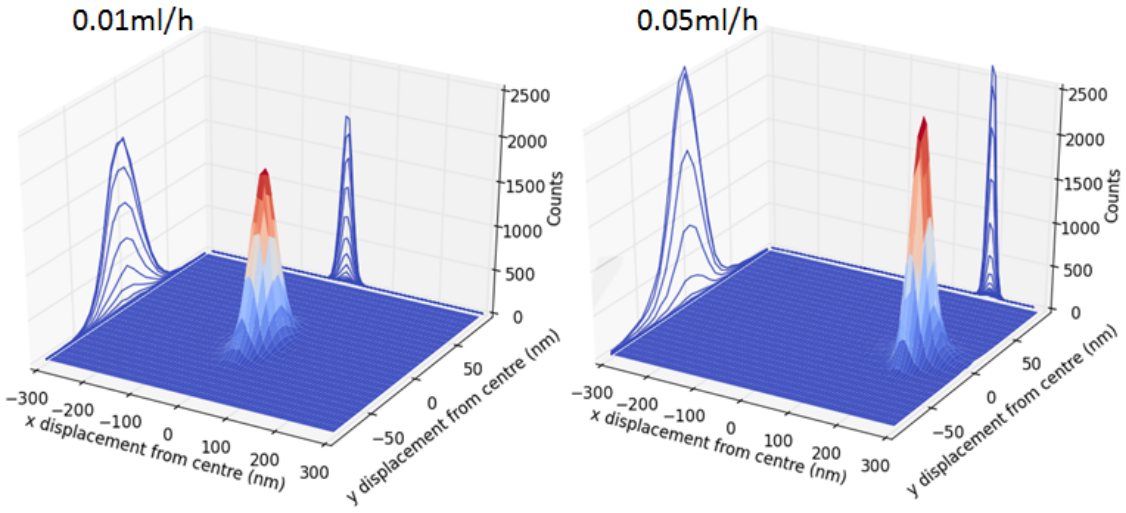


Figure 3.11: *Histograms of the obtained particle positions (from the trap centre) for flow rates of 0.01 ml/h and 0.05 ml/h.*

particle has been pushed to one side of the trap and thus displaced to the edge of the potential well created by the optical trap. Also visible is a change in the size of fluctuations as the bead positions tend to be more clustered; it is possible that the particle being pushed to the edge of the trap has a stabilising effect perpendicular and parallel to the flow. The power spectra of particle positions in flow were also calculated.

Figure 3.12 shows the power spectra for particle positions perpendicular to the direction of flow. From this, we can see that an increase in flow increases the corner frequency, from which one might deduce that, counterintuitively, flowing more material past a trapped bead increases the trap stiffness. However, it is more likely that because the bead is being pushed to an area of higher potential, the trap only appears to be stiffer as the bead motion is stablised slightly more. We can also see a decrease at 0.07 ml/h, showing that at this point the bead is starting to be pushed out of the trap and increasing the flow rate causes the bead to leave the trap. The maximum flow rate in the system was therefore limited to 0.07 ml/h.

In any optical tweezing system, it is important to be able to predict and reduce

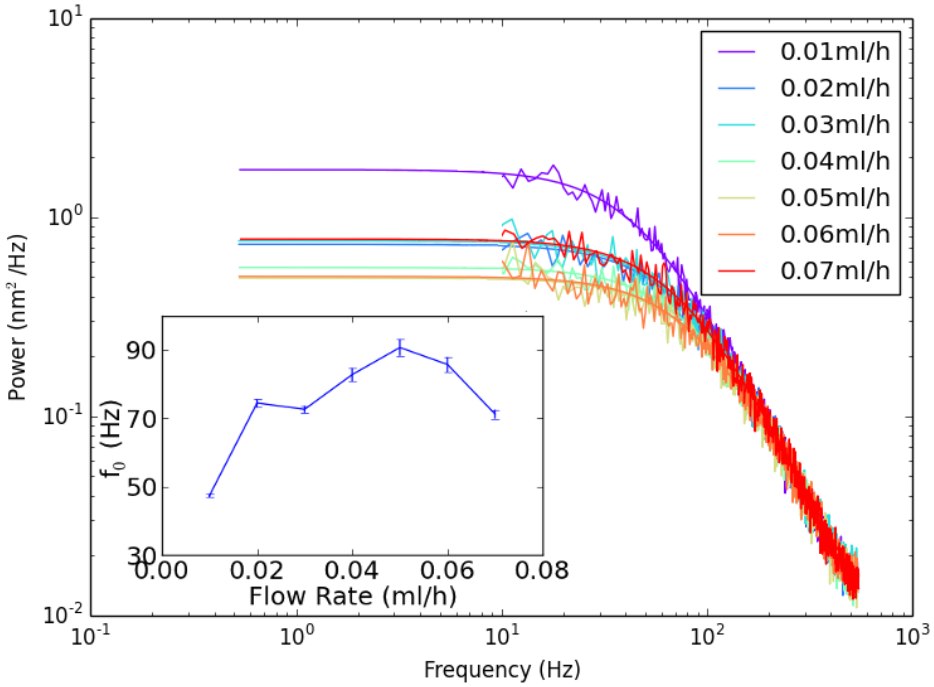


Figure 3.12: *Power spectra of a single 3 µm diameter bead trapped at the same trapping power (300 mW) for different flow rates*

the effects of noise, which may arise from several different sources. Low frequency vibrations such as people walking near the system may be reduced through the use of floating optical benches, for example. However, some noise sources may be intrinsically coupled to the system and cannot be removed. It is therefore beneficial to be able to anticipate and measure the contribution of noise sources in the system. The Allan variance is one such method of quantifying noise and was developed to extrapolate the drift of a system at infinity from finite measurements [74], and is used to measure frequency stability in atomic clocks [75], and frequency stabilised lasers [76]. In optical tweezers, it may be used to anticipate the contribution of external noise sources such as piezo stages and decide upon optimal time intervals for measurements [77], in active and passive calibration of tweezers [78], and has also been used to prove that CMOS cameras have a high enough time resolution for particle tracking [79].

The Allan variance $\sigma_x^2$ is defined as (for a total acquisition time of $t_{aq}$) [79]:

$$\sigma_x^2(\tau) = \frac{1}{2}\left\langle (x_{i+1} - x_i)^2 \right\rangle_\tau \tag{3.3.5}$$

where $x_i$ is the mean over a time interval of length $\tau$

The statistical error is given by (if we approximate $n = N/m$, where $N$ is the number of sampling points and $m$ is the number of points in interval $\tau$:

$$SE_{\sigma(\tau)} = \frac{\sigma_x(\tau)}{\sqrt{n}} = \sqrt{\frac{\tau}{t_{aq}}}\sigma_x(\tau) \tag{3.3.6}$$

Given that the movement of beads is dependent on diffusion, the mean squared displacement $\langle x^2 \rangle$ of the bead motion may be written in terms of the diffusivity $D$ as $2D\tau$, where $D = 2k_BT/\gamma$ [80]. From this we can find the thermal limit for positional detection, with $\gamma$ as the bead's drag coefficient and $\kappa$ the trap stiffness:

$$SE_{\langle x \rangle} = \frac{1}{\sqrt{n}}\sqrt{\langle x^2 \rangle} \approx \sqrt{\frac{2k_BT\gamma}{\kappa^2\tau}} \tag{3.3.7}$$

Where the Allan deviation $\sigma_x$ is a minimum indicates the precision with which the trap centre can be determined.

Figure 3.13 shows the results of calculating the Allan deviation when the system is in the presence of several different noise sources which could not be isolated from the system. The microfluidic pump itself may cause vibrations as it contains moving parts and is intrinsically coupled to the system through the pipes connecting the syringe to the channel. Additionally, the trapping laser is cooled by a fan which vibrates at a frequency of approximately 40 yHz. From finding the minimum values of the Allan deviation in the plots in Figure 3.13, the trap centre can be determined to a minimum precision of 1.37 nm when the laser fan is off and of 3.38 nm when the laser fan is switched on, at time intervals of 0.039 s and 1.38 s respectively. The thermal limit shows that when the fan is switched off, position measurements at short measurement times are close to the thermal

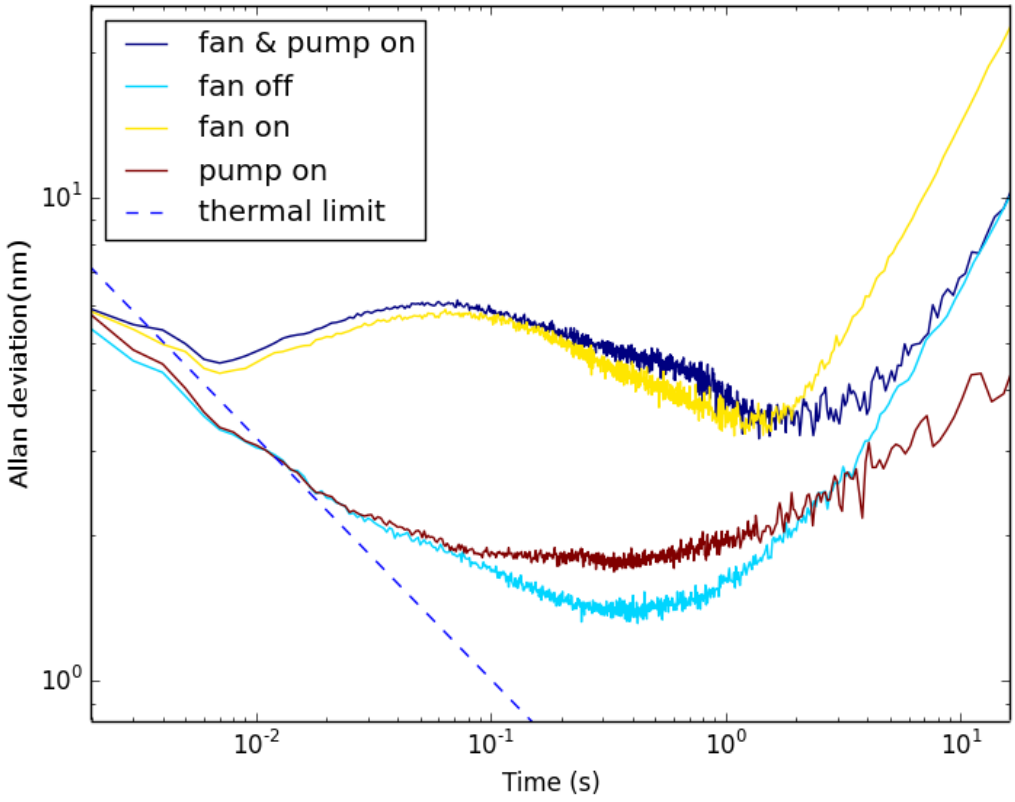


Figure 3.13: *The Allan deviation calculated over a range of time intervals for different noise sources in the system*

limit, suggesting there is little noise in the system when the laser fan and pump are switched off (at very short timescales the correlation in the values causes the thermal limit and experimentally calculated Allan deviation to cross). There is a very small increase in the minimum of the Allan deviation of about 0.04 nm when the pump is switched on without the fan, showing that the pump has a minimal effect on the precision at which measurements can be taken, although the Allan deviation surprisingly rises less steeply when the pump is switched off for longer periods of time, indicating that the pump contributes less to the noise at longer timescales. This may be due to increased stability in the trap from the fluid flow as debated earlier. It is clear therefore that the laser fan is responsible for the majority of noise in the system, as this not only vibrates the optical table but also the laser itself. Given it is impractical to remove the fan for long experiment lengths of up to 30 minutes, experiments were taken for 10 minutes at a time with one minute intervals where the fan was switched back on.

## 3.4 Flow visualization and dishwasher solutions

Being able to predict the flow in the microfluidic channel is crucial, as it tells us the sort of speed at which material will flow past the trapped species, and where in the channel it might be best to trap our bead. The flow in a microfluidic channel varies across its width. Particle image velocimetry may be used to model the speed of the flow in the microfluidic channel [81]. This is where seed particles in a fairly high concentration are added to a fluid under investigation which is then introduced into the channel. These particles must be small to follow the fluid flow satisfactorily but also be large enough to be imaged; these are typically 10-100 micrometres, although they may be larger. In this investigation, given that fairly wide channels were under examination, 2 micron diameter fluorescent beads were used to investigate the fluid flow, for visibility and also to model the flow of particulates which appear in the dishwasher solution around the bead and in the channel; these may vary in size from a few nanometres to a few micrometres.

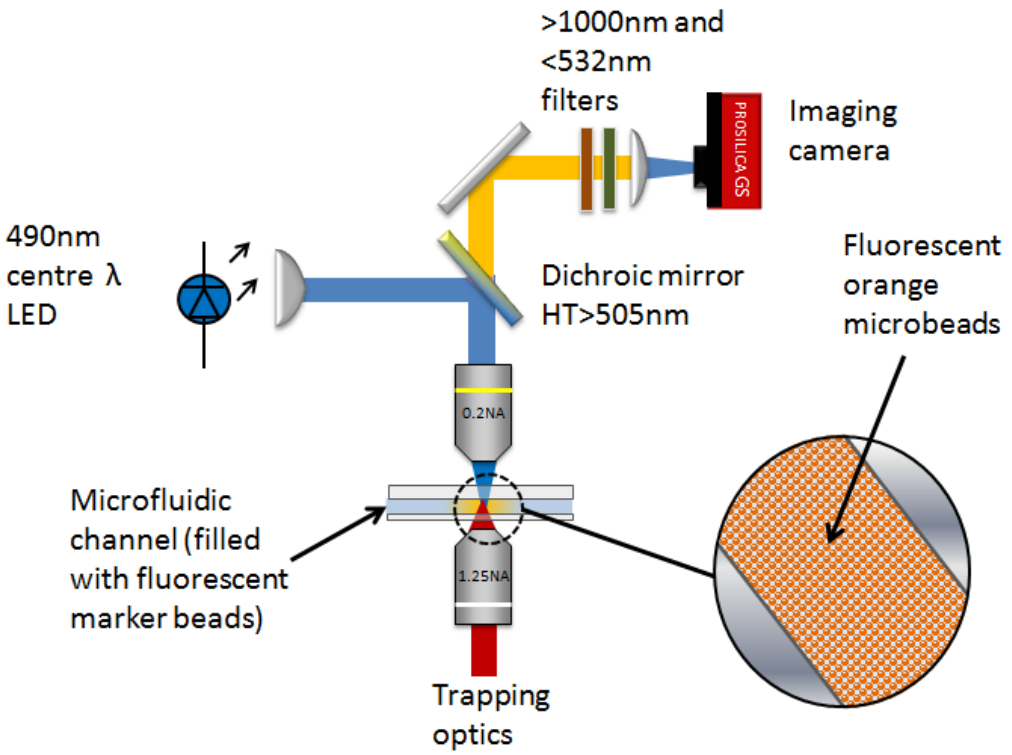


Figure 3.14: *The particle image velocimetry setup mounted above the trapping optics*

Excitation of the fluorescent beads in particle image velocimetry is usually achieved through the use of a cylindrical lens to create a light sheet through the sample so a very narrow z-section is illuminated [82]. This is often difficult in microfluidic channels which can be very thin and it may not be possible to direct light through the side. In this case we have a thin channel relative to its width and length, and thus we can use thresholding so only particles that are in focus contribute.

Figure 3.14 shows the experimental setup added on top of the current optical tweezing setup from Figure 3.1. A blue LED was focussed through a 0.2 NA 10x microscope objective onto the microfluidic slide from above; this was the highest NA that could be used for imaging through the 1mm thick top area of the microfluidic channel (see figure 6.3 in chapter 6). Fluorescent 2 $\mu$m diameter beads (Sigma L3030) were suspended in distilled water in 1:40 concentration and both illuminated and imaged from above the channel. The emitted light passed through

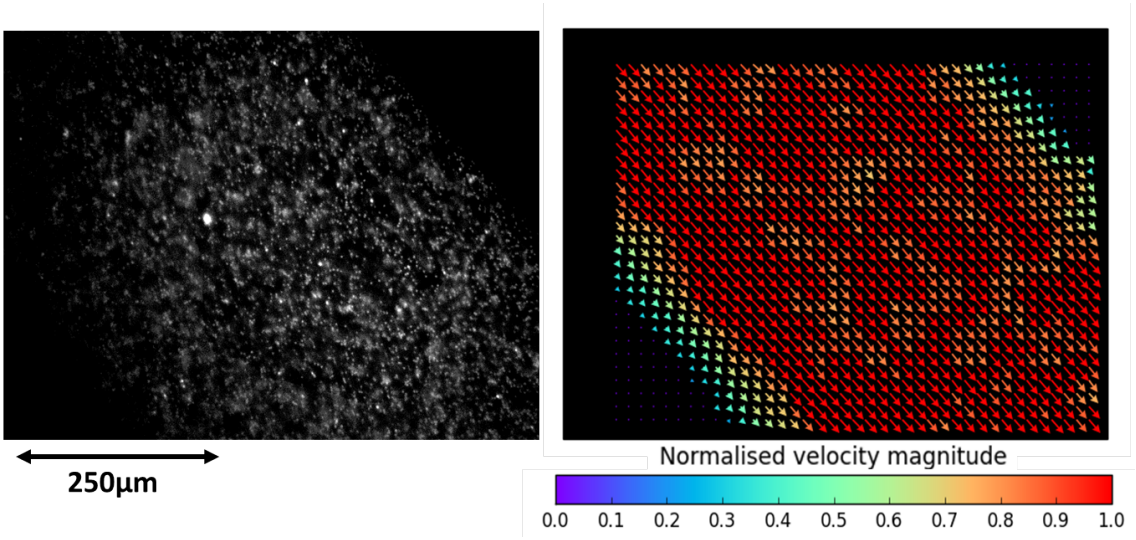


Figure 3.15: *A map of the normalised velocity profile in a channel of width 500 µm for laminar flow at low Reynolds number, and the accompanying fluorescent particle image. Arrows indicate the direction of the particle velocity and arrow length/colour indicates the magnitude of the velocity*

a dichroic mirror to the detector (Prosilica GS). Images were obtained over time using a LabVIEW program at a rate of 100 frames per second, and the ImageJ PIV plugin was used to calculate the velocity map for consecutive images of particles in flow.

Figure 3.15 shows the obtained flow map when the water/bead solution is pumped through the channel at a constant rate. We can see that while there are a few residuals, most likely due to small flow variations due to the bead size and/or beads stuck to the surface of the channel, the overall flow is laminar, with faster flows in the centre of the channel and slower flow at the edges. We would expect this as the velocity profile of the flow in a circular channel tends to be a parabola [83] (also known as Poiseuille flow), as shown in figure 3.16. However, in this case the channel cross-sectional shape is a very thin semicircle, and so we would expect the flow to fall off more gradually at the channel edges. This suggests that the ideal position for optical trapping in constant flow in the channel is away from the edges of the channel in the centre. We also see that the flow is fairly uniform in the central region, which we would expect due to the very low Reynolds number

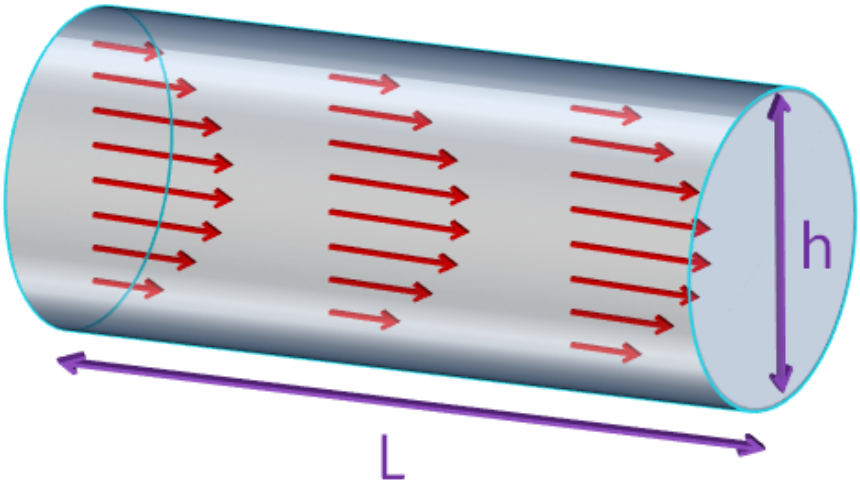


Figure 3.16: *A simple diagram illustrating Poiseuille flow through a circular channel of length L and diameter h. The red arrows depict the flow of fluid through the tube, which has a parabolic profile*

of the flow in the channel; the area is not perfectly uniform, most likely due to the settling of beads due to gravity in the channel. Trapping near the centre of a microfluidic channel is generally good practice, owing to both aberrations of the trapping beam near channel edges and also pressure reflections from the channel surface at the edge (which may be compensated for using Faxen's correction [84]).

Figure 3.17 shows the obtained velocity map when a bubble is present in the solution. This can occur when the flow is not steady, or when there is a chemical reaction occurring which causes bubbles (which is discussed in more detail in chapter 6). We can see that the overall flow in this case is lower than usual, especially at the sides, and the flow tends to move very quickly around the edges of bubbles. Bubbles can form in the dishwashing system due to the presence of surfactant, although at the relatively high temperatures the solutions are kept at they are not a particular issue.

We may also use this system to check the effect of the trap on trapped particulates and find the area around which particulates are drawn to the trap. Figure 3.18 shows the flow of the 2 $\mu$m diameter beads around an optical trap. In this

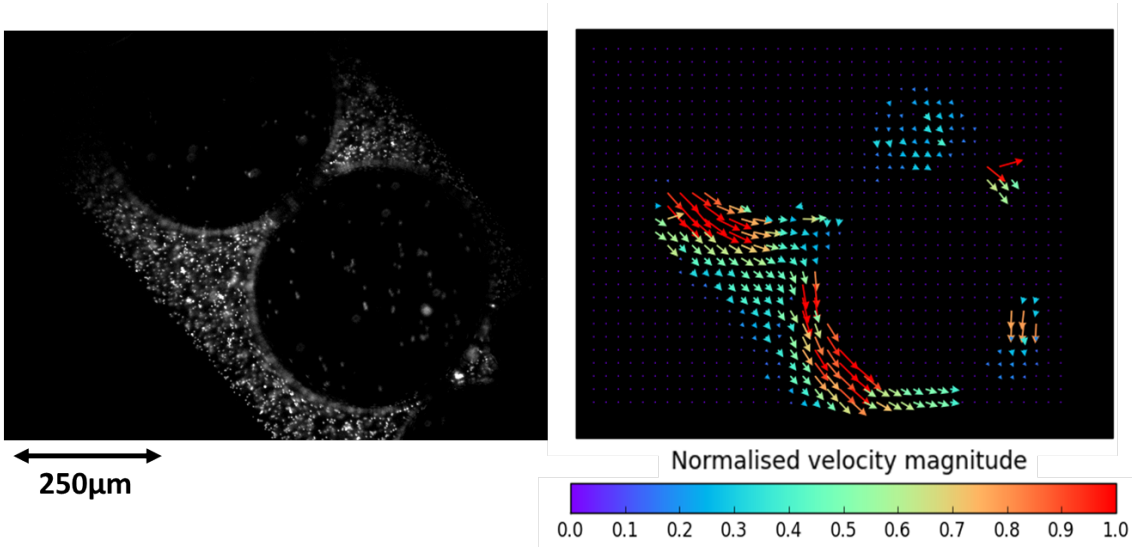


Figure 3.17: *A map of the normalised velocity profile in a channel of width 500 µm in the presence of air bubbles, and the accompanying fluorescent particle image. Arrows indicate the direction of the particle velocity and arrow length/colour indicates the magnitude of the velocity*

case, the trap area itself captured some of the tracker beads and caused a high fluorescence signal at this point, which is more or less stationary between successive image captures. Around this area, we can see a small change in the flow around the trap; the flow is slower owing to the presence of the obstruction caused by several beads caught in the trap. The overall flow is only affected in a region of an area of around 10 $\mu$m, which was not high enough to disrupt the overall flow of the system. It was not possible to check the flow around a trapped bead as the fluorescent microspheres tended to push the three micron bead out of the trap; however, from previous work (on larger beads) we would expect to observe laminar flow around the bead at low Reynolds numbers [85].

It is necessary to model a typical dishwasher solution correctly to analyse materials involved in reaction. In a dishwasher, calcium carbonate is typically formed by the reaction between calcium ions in the water and alkaline detergents, such as sodium carbonate. To mimic the ions present in hard water, calcium and magnesium chloride were added to deionised water. The magnesium chloride was added as this typically contributes to the filming of calcium carbonate. The chelating

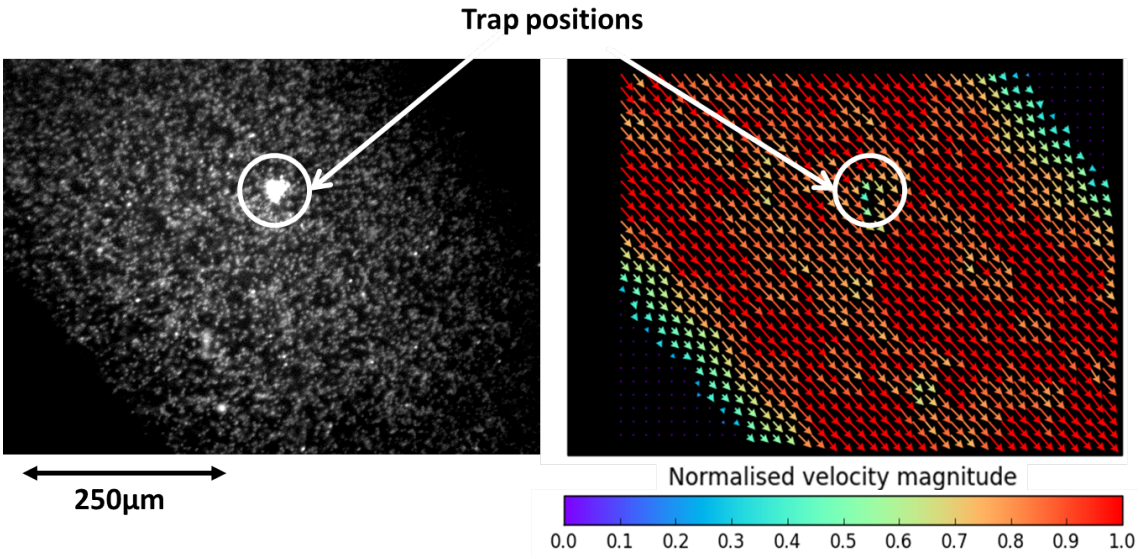


Figure 3.18: *A map of the normalised velocity profile in a channel of width 500 µm when the optical trap is switched on, and the accompanying fluorescent particle image. Arrows indicate the direction of the particle velocity and arrow length/colour indicates the magnitude of the velocity*

agent, sulphonated polymer and surfactant (TWEEN 20) were also added (concentrations and official names of chemicals in brackets are confidential and thus not given here). Solid forms of each reactant apart from sodium carbonate were weighed out and mixed with 40 ml water. The sodium carbonate was weighed out separately and mixed with 10 ml water. 4 ml of the solution of calcium chloride and reactants (as shown in Table 3.1) and 1 ml of the sodium carbonate solution were pipetted into separate vials and approximately 10 µL of bead solution (Phosphorex 3 µm diameter) and heated using a hot plate to 70 °C. These were then introduced into the channel using a 1ml capacity syringe (B-D Luer locking). The channel was kept at a temperature of 60 °C through the use of a temperature controlled power resistor thermally bonded to the channel and monitored through the use of a thermocouple close to the channel outlet. The temperature of the liquid did not fall below 55 °C throughout the duration of the experiment.

Originally only calcium chloride and sodium carbonate were mixed together, but it was found that the reaction took place too quickly and large calcium car-

Table 3.1: *Dishwashing formula for 5L water*

| Hard water | | Builder | | | Polyacrylate | Surfactant |
|---|---|---|---|---|---|---|
| $CaCl_2$ | $MgCl_2$ | (Complexer) | $Na_2SO_4$ | $Na_2CO_3$ | (Polymer) | Tween 20 |

bonates tended to form in solution, rather than on the beads; given the beads are very small compared to the size of glasses in dishwashers, this is unsurprising. The addition of the polymer and complexing agent means it is harder for the calcium carbonate to form large crystals; thus small crystals may be seen floating past. In the next chapter, the use of both different solutions is described and their effects on the power spectra are compared.

In conclusion, a bespoke Raman tweezer system was built and microfluidic flow control implemented. However, initially some unusual effects were observed, and thus it was necessary to be able to properly predict the response of the system and compensate for some of these effects. Examples include the fluorescence background of the water, which was compensated for using both computational and experimental methods, involving the use of a technique designed by Rusciano et. al. [72]. The microfluidic flow itself was also investigated for uniformity across the channel via the use of particle image velocimetry, and the effects of this flow on the power spectra were also examined.

# Chapter 4

# Results and Initial Discussions

*This chapter deals with the results obtained using the Raman Tweezing setup and focuses on the different methods which can be used to detect the very small amounts of buildup which occur on trapped beads in dishwasher conditions.*

## 4.1 Raman investigations

### 4.1.1 Characterising the Raman volume

In any Raman tweezers setup, it is important to be able to characterize the Raman volume in which Raman emission measurements will be taken. The beam profile of the focussed excitation beam itself was investigated by flooding the microfluidic channel with a high concentration of erythrocin B, which fluoresces under green light, and moving the channel axially in $1\,\mu$m steps using the motorised stage. Images were obtained for each step via a webcam and the intensity between each image step was obtained in ImageJ using interpolation to build a smooth axial image.

The obtained profile is shown in Figure 4.1, which gives the average pixel values across the $x$ and $y$ axes of the beam from the images taken. From this, we can see that the beam profile in each direction at the beam focus $f$ fits to a Gaussian, with the fit becoming poorer as the distance from the maximum intensity increases;

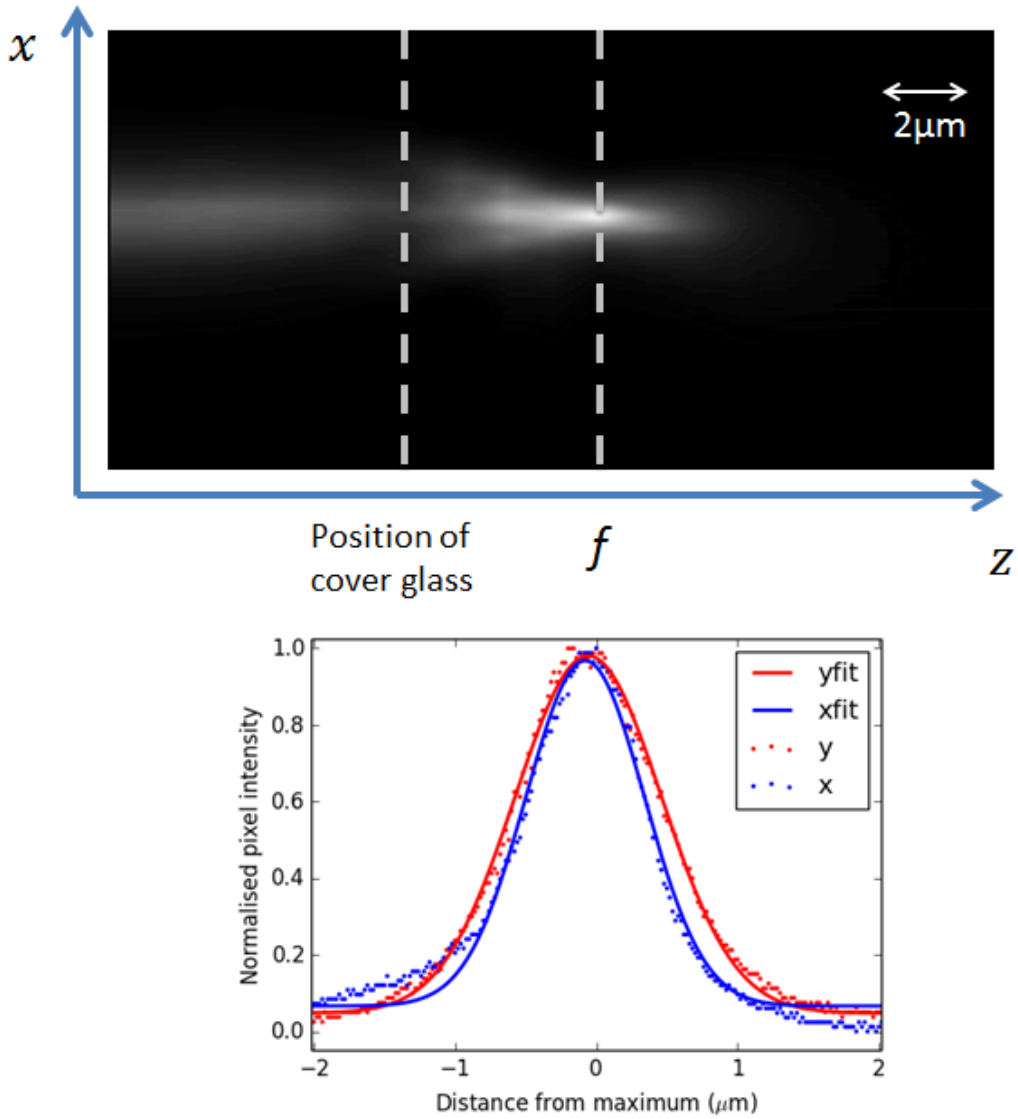


Figure 4.1: *Top: The obtained interpolated z-axis image of the fluorescence of erythrocin B excited by the 532 nm focussed excitation beam. Bottom: The calculated intensity profile over each pixel at point f obtained in each axis and the Gaussian least squares fit*

due to optical components drifting and imprecise alignment the profiles are very slightly skewed and also slightly wider in the $y$ direction than the $x$ direction. The perfectly diffraction limited radial spot size for a Gaussian beam of wavelength $\lambda$ focussed through a lens of numerical aperture NA and mounting medium refractive index $n$ is given by:

$$d_{lateral} = \frac{1.22\lambda}{\mathrm{NA}} \tag{4.1.1}$$

and the axial spot size, which is double the depth of focus, is given by:

$$d_{axial} = \frac{2n\lambda}{\mathrm{NA}^2} \tag{4.1.2}$$

In this case, $d_{lateral} = 0.518\,\mu$m, and $d_{axial} = 1.033\,\mu$m. The FWHMs in each direction were calculated from the Gaussian fits to be $\mathrm{FWHM}_x = 0.99 \pm 0.01\,\mu$m and $\mathrm{FWHM}_y = 1.22 \pm 0.01\,\mu$m, and the extent of the volume in the z direction is given by $2\sqrt{2}\times\mathrm{FWHM}_{av}$ [86], which was calculated to be $3.12 \pm 0.02\mu$m . The beam is therefore not perfectly diffraction limited. We would expect a very small aberration to arise from the microscope objective being optimised for a coverglass width of $0.17\,\mu$m, whereas the width of the bottom of the microfluidic slide is only $0.14\,\mu$m, but the majority of the discrepancy is most likely to be due to imperfect alignment as mentioned previously. The light profile between $z = 0$ and the position of the coverglass (that is, the bottom edge of the microfluidic channel) is due to the transmission of fluorescence light through the coverglass and immersion oil.

To demonstrate the utility of the excitation beam for accurate detection of materials within a certain distance, the 1064 nm laser beam was used as a trapping laser to move a 3 micron diameter PMMA bead across the 532 nm excitation beam in $1\,\mu$m steps, which was achieved with high precision using the SLM. Each time the bead was moved its Raman spectrum was taken with an integration time of 1 second. Figure 4.2 shows the results of plotting the background subtracted height of the $2957\,\mathrm{cm}^{-1}$ peak, which is a major feature in the spectrum of PMMA (see Chapter 3) against the bead position relative to the position of the centre of the excitation beam.

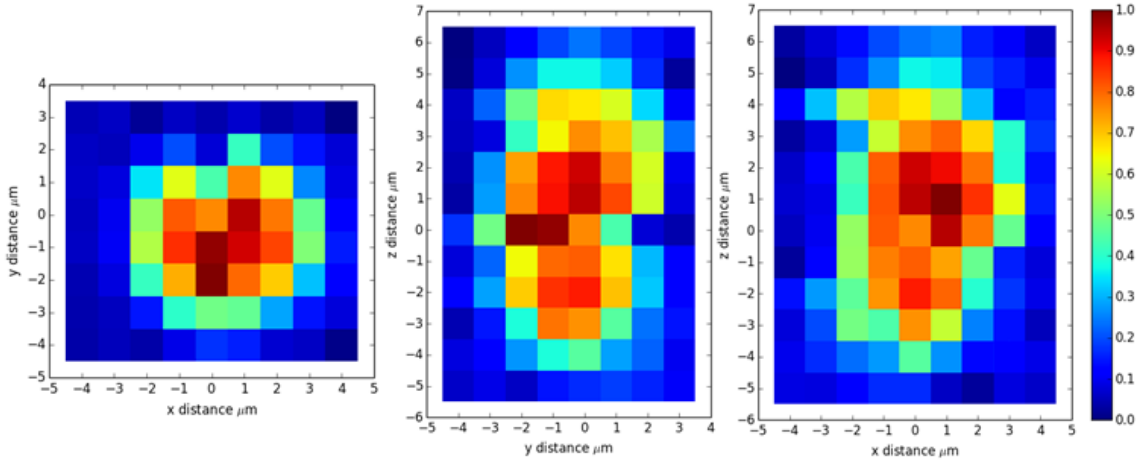


Figure 4.2: *Raman images taken in 3 different axes of a trapped 3 μm diameter PMMA bead. The pixel colour is mapped to the bar on the right which indicates the normalised intensity of the 2957 $cm^{-1}$ C-H stretching peak in PMMA*

From this, we can see that in the lateral section taken at the focus, the Raman spectral intensity is a maximum for a diameter of around 3 $\mu$m, which we would expect; given that the beam is expected to have a Gaussian profile, we would also expect the gradual decrease in intensity continuing outside the bead radius. This could also in part be attributed to the slight movement of the bead in the optical trap itself, although this would not contribute to the spectrum outside the beam area to such an extent. As the beam profile of the 532 nm excitation beam will be longer in the z-axis than in the lateral axes, we would expect the spectrum to be present for a greater axial distance. It is also evident that the slight skewing of the beam profile has little effect on the obtained Raman signal.

### 4.1.2 Investigating carbonate crystallisation on the channel surface

It is possible to use the setup with only the green excitation beam as a method of mapping the spectrum of calcium carbonate which builds up on the flat glass surface of the channel during the experiment. This build-up can be a nuisance

for trapping as the channel must be cleaned thoroughly between each use with dilute hydrochloric acid to remove this build-up, as it may cause aberrations in the trapping beam travelling through the coverslip. It may also cause crystals to preferentially adhere to crystals already present on the glass rather than the trapped beads. However, it also allows us to study crystals which build up on glass. This is known as Raman imaging [87] and is an invaluable tool in the investigation of surface science. Figure 4.3 demonstrates the use of this technique for a build-up of crystals around a PMMA bead stuck to the channel surface. From simple imaging, it is difficult to distinguish between the two; however, Raman imaging clearly reveals the extents of the two materials on the slide, with some error allowing for the Gaussian nature of the beam.

All spectra obtained from the coverglass were found each time to have the $155\,\mathrm{cm}^{-1}$ and $281\,\mathrm{cm}^{-1}$ peaks common to the Raman spectrum of calcite. It was thus deduced that for flat glass, the polymorph of calcium carbonate which preferentially builds up is calcite. It was however also found that the structure of the crystals was mostly cubic without the polymer and complexer present whereas irregular shapes were obtained when these were added. This suggests that the polymer and complexer inhibit the formation of larger uniform crystals, as would be expected.

### 4.1.3 Raman spectroscopy of trapped material in flow

We may gain insight into the precipitates which form in the mixed dishwasher solution in the absence of beads by simply trapping material in the solution when no beads are present in the solution, creating a combined lump of particulates which are trapped according to their opacity. Figure 4.4 shows the background subtracted spectra obtained when particulates are trapped in solution a few minutes after mixing. This spectrum may be separated into two separate spectra which dominate; that of calcium carbonate, and also a spectrum which was deduced to be that of the surfactant used, TWEEN 20 [88]. This was confirmed by flowing water and surfactant only through the channel, resulting in the spectrum shown in Figure 4.5. It is important to note that such particulates are not stably trapped;

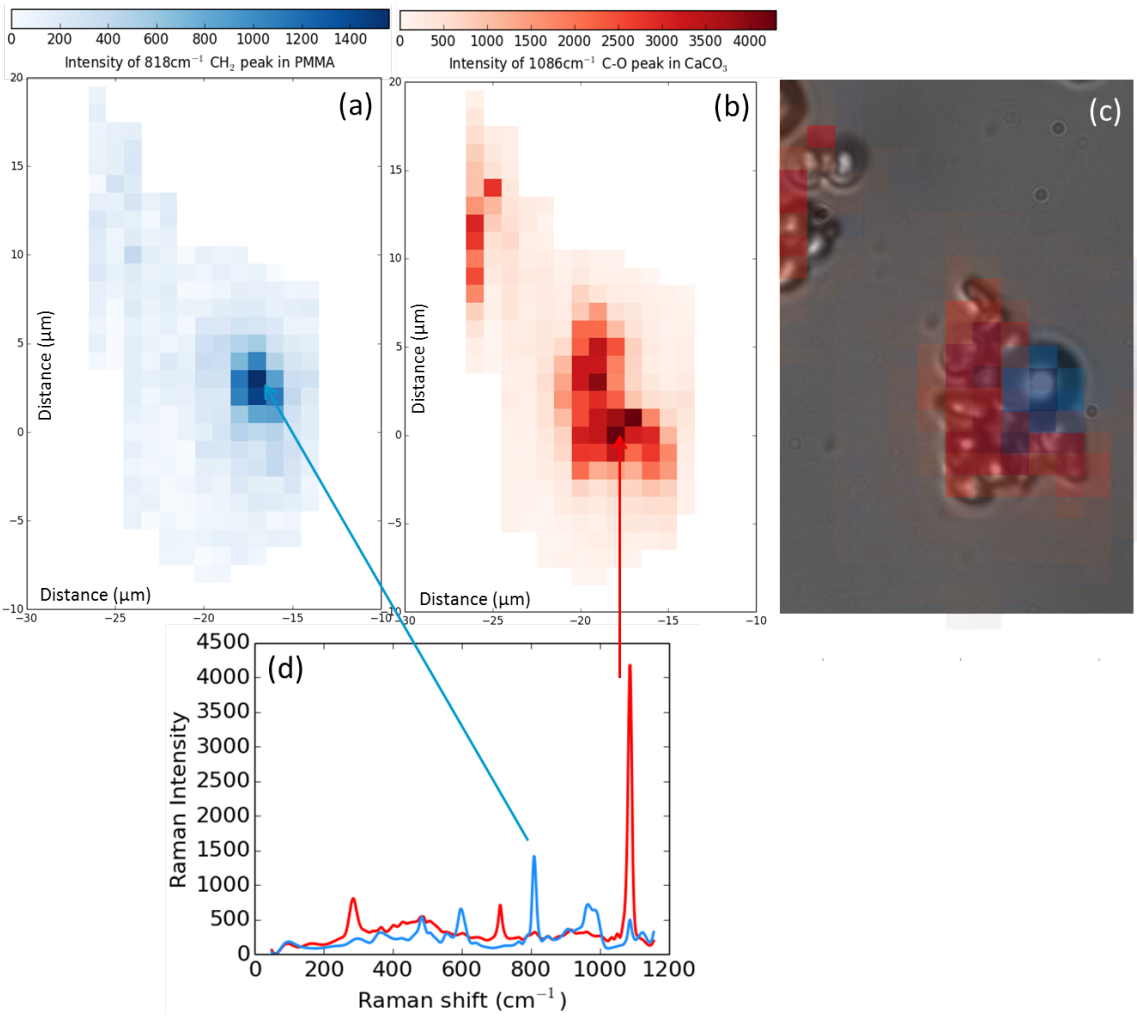


Figure 4.3: *A surface Raman spectrum taken for build-up around a PMMA bead in the microfluidic channel. (a) Surface spectrum of 181 $cm^{-1}$ peak in PMMA (b) Surface spectrum of 1086 $cm^{-1}$ peak in $CaCO_3$, (c) Overlaid spectra on a camera image of the build-up, and (d) An example of the background subtracted Raman spectral data. We can clearly see that the spherical particle is a PMMA bead rather than calcite from the Raman spectrum in this area*

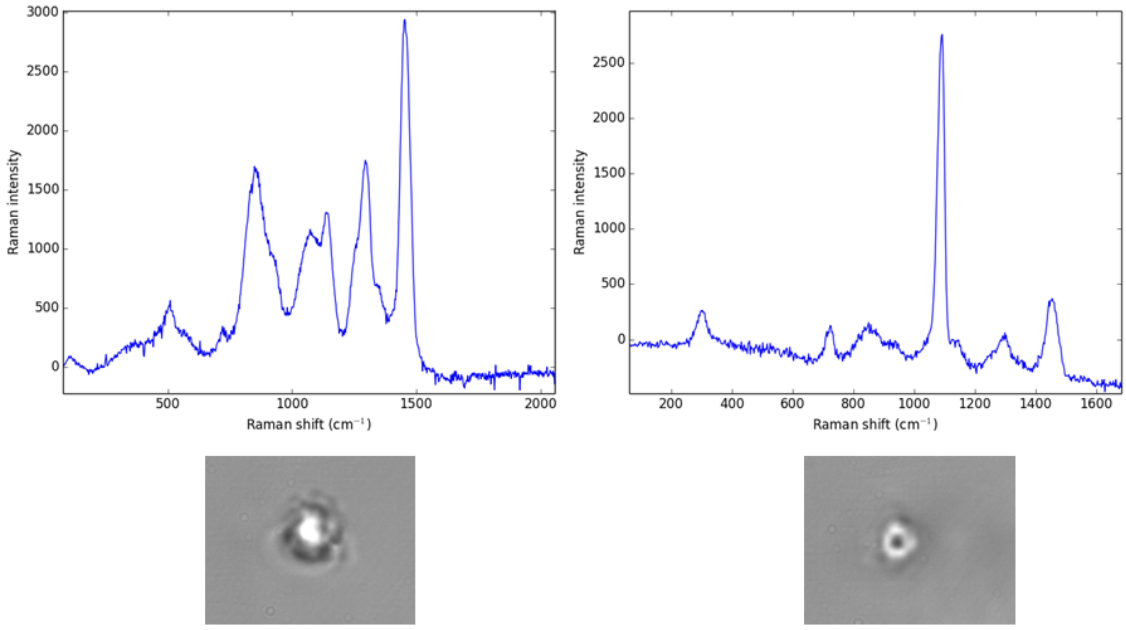


Figure 4.4: *The background subtracted Raman spectra of material trapped in the optical trap 10 minutes after reaction begins, along with the corresponding images of the trapped particulates. In the image on the left, the spectrum is dominated by the surfactant spectrum, whereas on the right, the spectrum is dominated by the calcium carbonate spectrum. Typically a mixture of the two compounds were usually obtained*

particles at the centre are much more strongly trapped than those at the sides due to the Gaussian profile of the trapping beam. One should also note that a shielding effect takes place around larger optically trapped species [85], which in this case prevents material being attracted to the optical trap after a certain amount of precipitates have already been trapped.

Figure 4.6 shows the Raman spectrum of TWEEN 20 trapped in solution after 250 seconds between $2600\,\mathrm{cm}^{-1}$ and $3100\,\mathrm{cm}^{-1}$, a region unaffected by fluorescence. We can observe the change in the $2905.9\,\mathrm{cm}^{-1}$ peak of the surfactant and deduce that small amount of the surfactant is first caught in the trap, some of which escapes (which is possibly due to a small local increase in the flow rate), and then the peak height increases to a maximum, meaning a maximum amount of surfactant has been trapped.

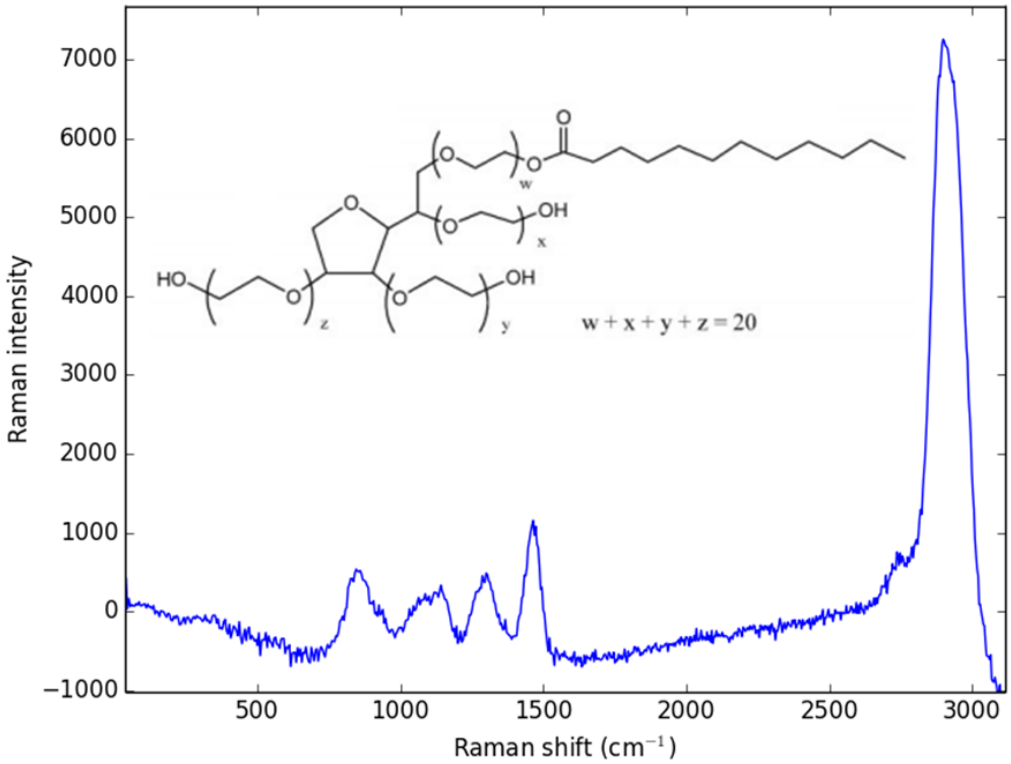


Figure 4.5: *The Raman spectrum of trapped TWEEN 20 only between 50 $cm^{-1}$ and 3100 $cm^{-1}$, showing peaks at 849.4 $cm^{-1}$, 1150.4 $cm^{-1}$, 1295.1 $cm^{-1}$, 1468.3 $cm^{-1}$ and 2905.9 $cm^{-1}$. Inset: the structure of the basic TWEEN molecule*

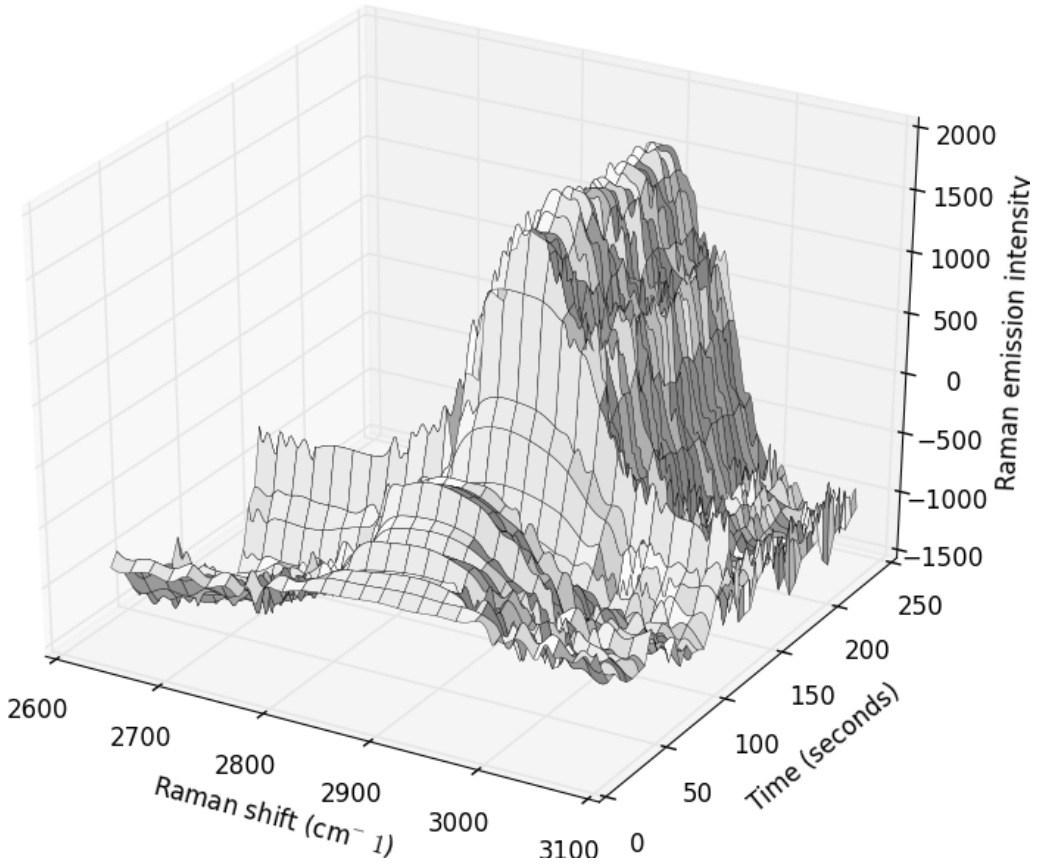


Figure 4.6: *3D surface plot demonstrating the background subtracted Raman spectrum of TWEEN 20 trapped in the optical trap over time between 2600 $cm^{-1}$ and 3100 $cm^{-1}$*

### 4.1.4 Raman spectroscopy of the surface of trapped beads in a dishwasher environment

#### Spectral acquisition with the CCD

3 $\mu$m diameter PMMA beads were trapped using the 1064nm laser and analysed over time using the excitation laser. An integration time of 10 seconds was used, and measurements were taken for 30 minutes. This was first attempted when flowing only distilled water past the specimen at a temperature no lower than 55 °C. It was found that there was little change in the Raman spectrum of the bead over time, as shown in Figure 4.7, which we would expect. This was then attempted with the solution described in Table 3.1 in Chapter 3. The solution was introduced to the channel immediately after mixing.

Figure 4.8 shows the change in the PMMA spectrum over time at the start of the reaction. As we can see, there is no obvious difference in the Raman spectrum for all known peaks of PMMA or at the 1086 $\mathrm{cm}^{-1}$ Raman shift characteristic of calcium carbonate compared to the spectrum obtained when no solution is present. This may be due to the very small amount of particulates which form at the start of the reaction, creating very thin layers of calcium carbonate. As the Raman excitation beam is quite small it is difficult to detect build-up on a surface unless we know exactly where it is, and the beads are quite large. However, reducing the size of the beads further reduces the likelihood of crystallisation as the surface area of a single bead is reduced and also inhibits shielding around the bead from the excitation beam, which is useful for preventing perceived build-up due to attraction of particulates by the beam, rather than surface adsorption.

Figure 4.9 shows the Raman spectra obtained over time when the solution from Table 3.1 with 10 $\mu$L bead solution is left after mixing for a few hours to react. In this case, we can see a marked increase in the amount of calcium carbonate which builds up on the bead, which happens in a very short amount of time (1 minute). This is most likely due to a larger amount of reacted calcium carbonate appearing

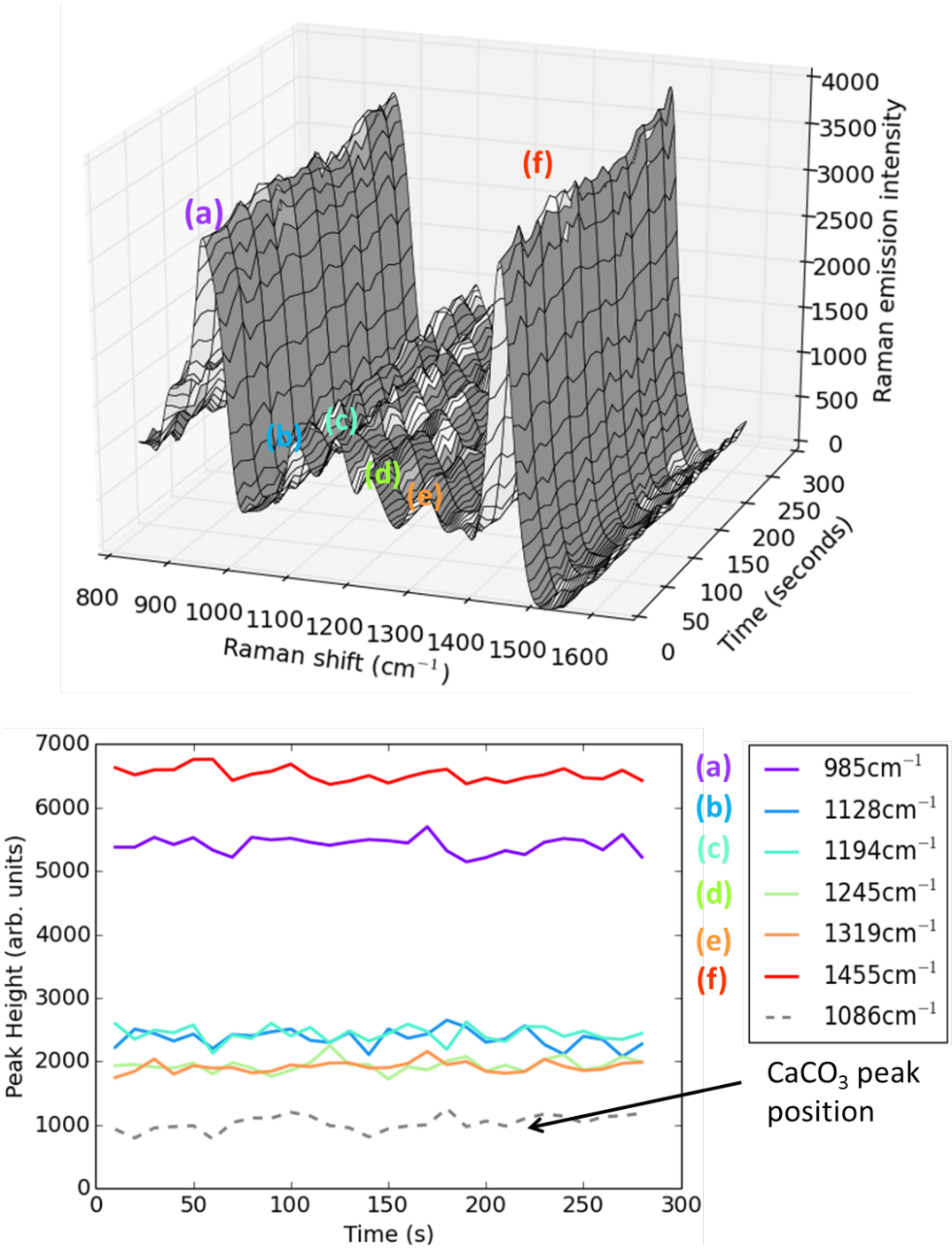


Figure 4.7: *Top: 3D surface plot showing the change in Raman spectrum over time when distilled water is flown past a trapped bead. Bottom: plots of the intensities of the known peaks of PMMA and $CaCO_3$ over time*

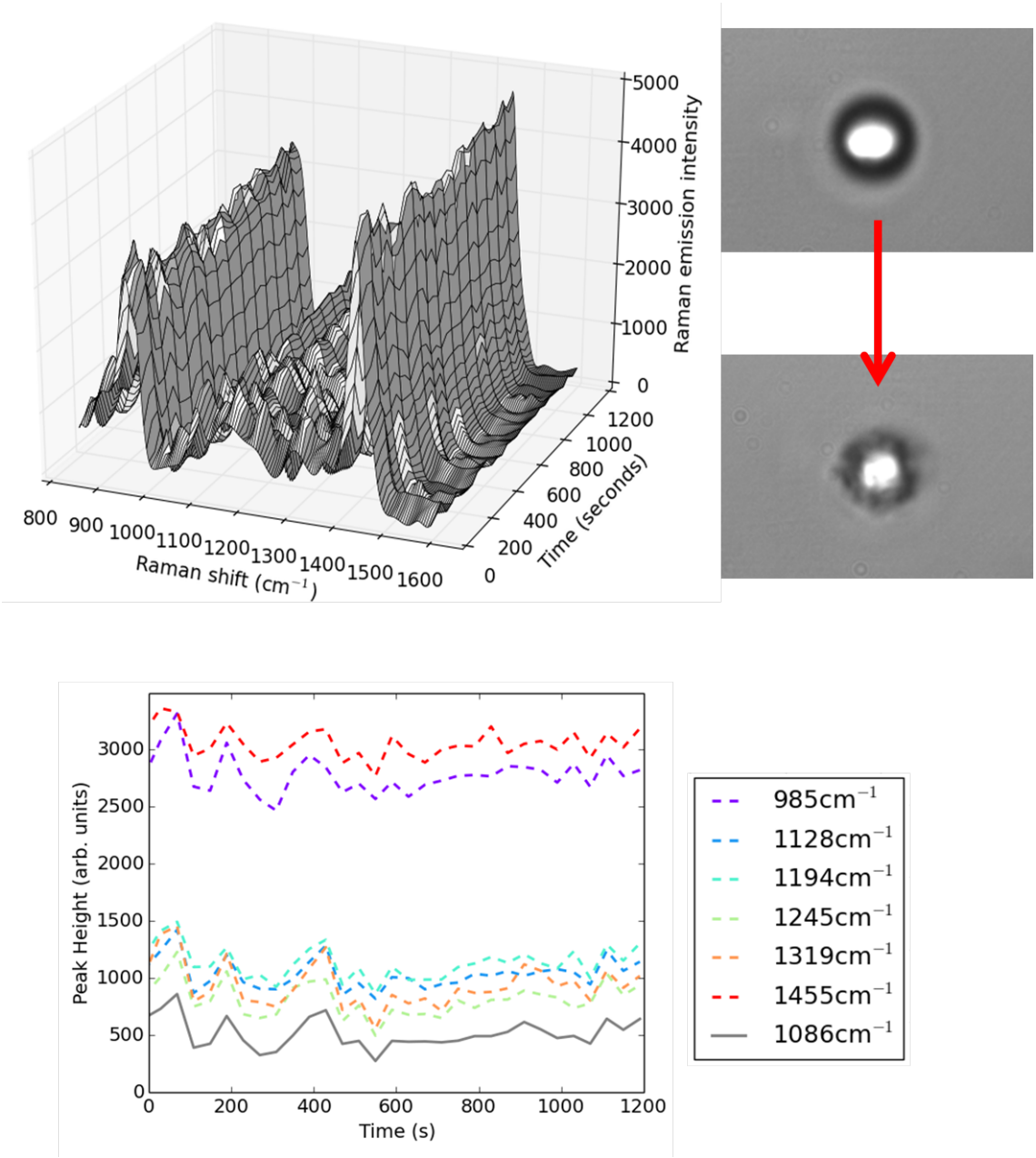


Figure 4.8: *Top: 3D surface plot showing the change in the Raman spectrum over time for freshly made solution, over a time period of 20 minutes. Bottom: plots of the intensities of known peaks of PMMA and $CaCO_3$ over time. Inset: Camera images of the trapped bead at the start of the reaction (upper) and after (lower) the reaction has taken place*

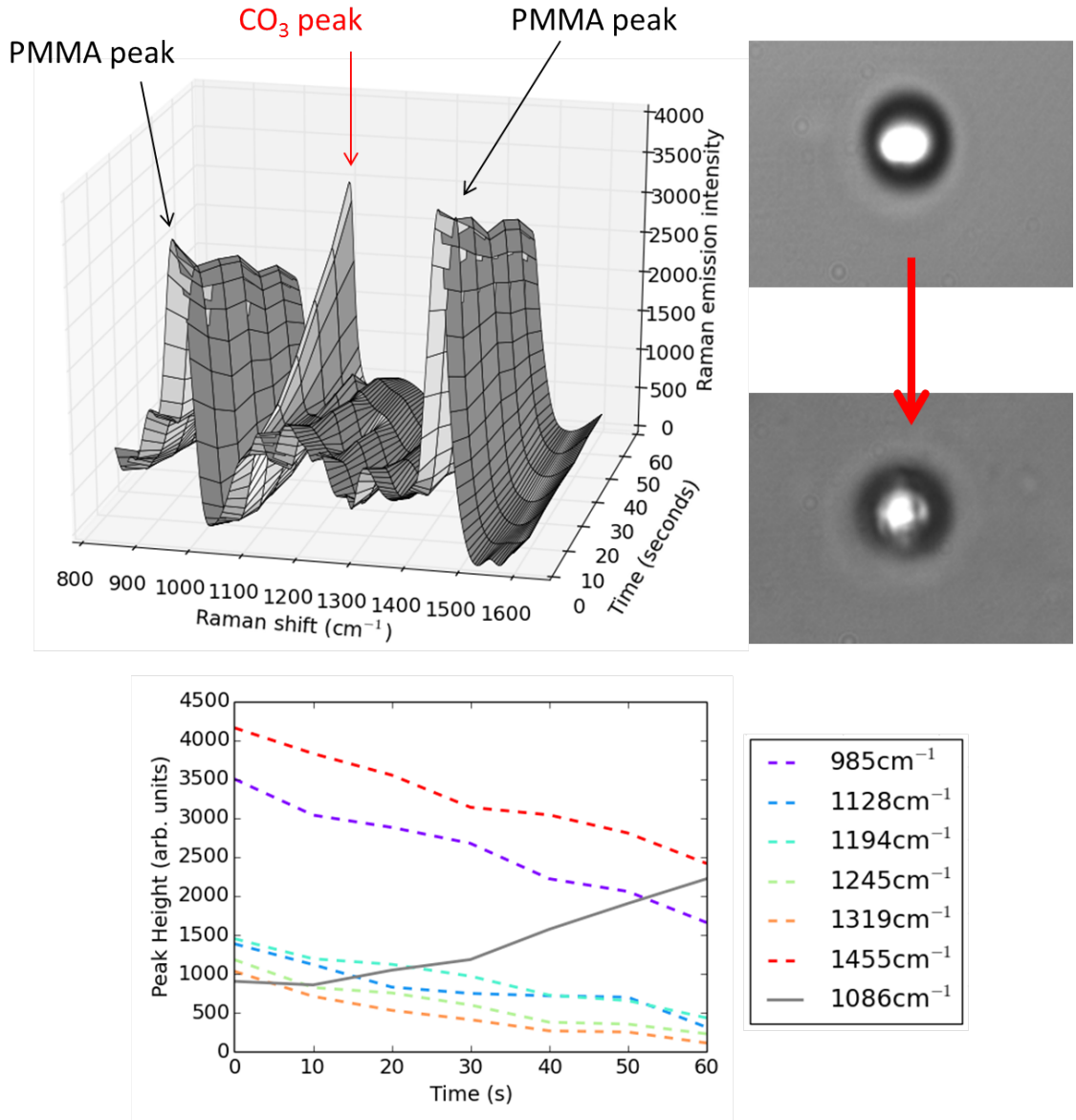


Figure 4.9: *Top: 3D surface plot showing the change in the Raman spectrum over time for solution mixed and then left for 8 hours before being introduced into the channel. Bottom: plots of the intensities of known peaks of PMMA and $CaCO_3$ over time. Inset: Camera images of the trapped bead at the start of the reaction (upper) and after (lower) the reaction has taken place*

in solution. Also noticeable is the small reduction in the peaks of PMMA, which is due to the bead being pushed slightly out of the optical trap as material in the trap re-centres itself to the trap centre. Unfortunately, it is difficult to deduce whether the crystals are actually building up on the bead or are experiencing a trapping force in the vicinity of the bead, mostly owing to the small amount of time that the bead can be caught in the trap before it escapes in the presence of larger particulates. It is possible that the increased amount of time for which the solution is left to react causes some small calcium carbonate adsorption on the surface, which thus encourages more calcium carbonate to build up on these beads when they are finally introduced; this agrees with the typical scenario in dishwashers, where it is generally found that crystallisation is worst after several washes due to this seeding effect. There is also a difference in the image obtained; in Figure 4.8, the particulates around the bead look very non-uniform, and the build-up is clearly made from many small particulates. In Figure 4.8, it is almost possible to see a crystal-like structure. Further imaging at a higher resolution, possibly using confocal scanning to image the bead at different axial points, may lead to more clarity. We can however deduce that Raman spectroscopy is not an adequate technique for detecting calcium carbonate immediately after the reaction has begun.

### Using phase sensitive detection

It was decided that phase sensitive detection may be a more sensitive method for analysis of material early in the reaction. First, the signal of a bead in distilled water was checked without fluid flow for a wavelength range of 500-700 nm in 0.5 nm steps, at a rate of one second per step. Figure 4.10 shows the Raman spectrum obtained from the phase sensitive detection setup for a PMMA bead trapped between both traps in distilled water. As we can see, the signal is of PMMA, and is automatically background subtracted, as we would expect given a signal is only detected when the bead is in the 532 nm trap. We would also expect to obtain the Raman spectrum of only distilled water upon changing the phase detected by the lock-in amplifier by 180 degrees.

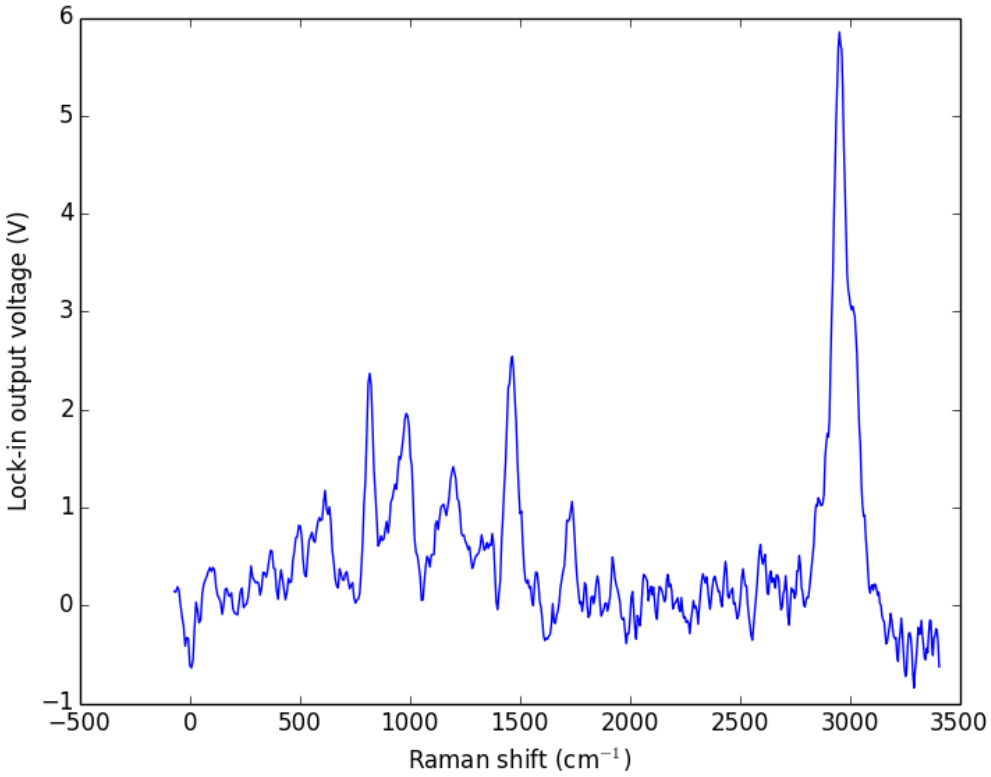


Figure 4.10: *Raman spectrum obtained from phase sensitive detection of a bead trapped between two optical traps; a modulated 1064nm beam and an unaltered 532nm beam, the latter of which acts as both an optical trap and a Raman excitation source*

The experiment was then attempted with the dishwasher solution. However, a problem was encountered upon initiating the flow with dishwasher solution. It was found that once material was flown past the pair of traps, any trapped beads were displaced from the trap immediately. It was thought that this may be due to the two trap oscillatory setup being inherently unstable, as the bead is constantly being pushed in and out of one continuous beam and one chopped beam; this is more of a concern when particulates may be in contact with the trapped bead, which slightly moves the bead in the trap as has already been discussed. To investigate this concept further, the motion of the bead between the two traps was monitored at a high acquisition frequency using the smart camera. A region of interest was selected which encompassed both the 1064 nm and 532 nm beam foci, and readings were taken at an acquisition frequency of 1700 Hz, far above the chopping frequency which was set to 20 Hz. The effect of the magnitude of the chopping frequency and the intensity of the 1064 nm beam were also investigated, as shown in Figure 4.11.

It can be seen from Figure 4.11 that as the trapping power increases, the modal bead positions approach the stationary laser spot positions, as shown in Figure 4.12. High 1064 nm laser trapping powers are necessary to pull the bead from the 532nm excitation trap, as this allows for modulation of the Raman signal from a maximum to a minimum. Large changes in the signal are easier to detect by the lock-in amplifier. However, at higher trapping powers, it is evident that the bead does not move directly between the traps as there is a probability of finding the bead in an arc above or below the direct straight line path between the two traps we would expect the bead to take. The bead also appears to be moving in a certain direction as the histogram shape is non-symmetric between the traps. This is also evident when the trap is modulated when the 532 nm beam is switched off; there appear to be two stable points at which the bead is trapped, rather than one.

This phenomenon was thought to be due to the fact that the 1064 nm laser was

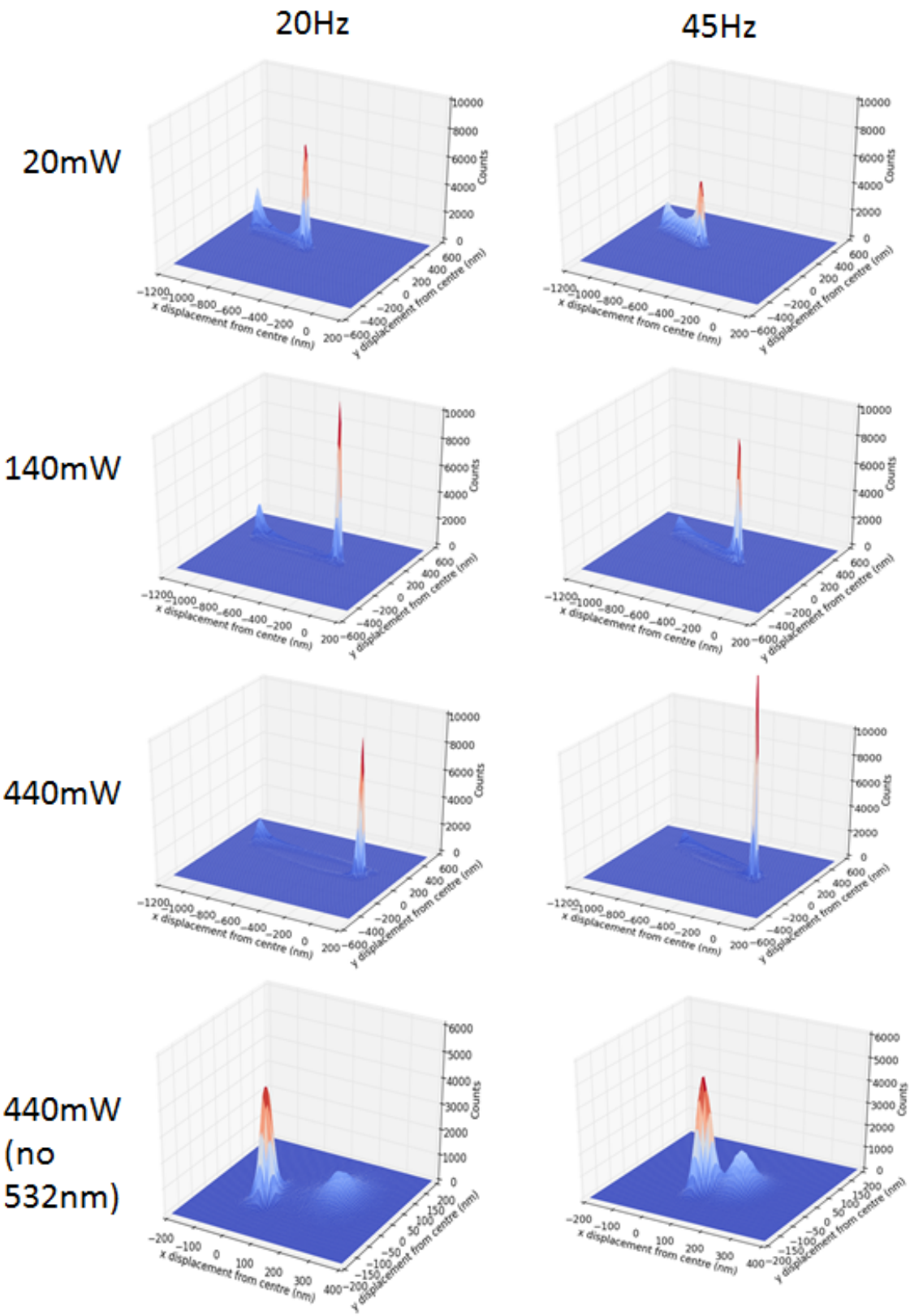


Figure 4.11: *Figures depicting the position counts of the centre of a bead moving in an optical trap in the x and y directions. The trap on the left is a trap formed by the 532 nm laser at an output power of 50 mW*

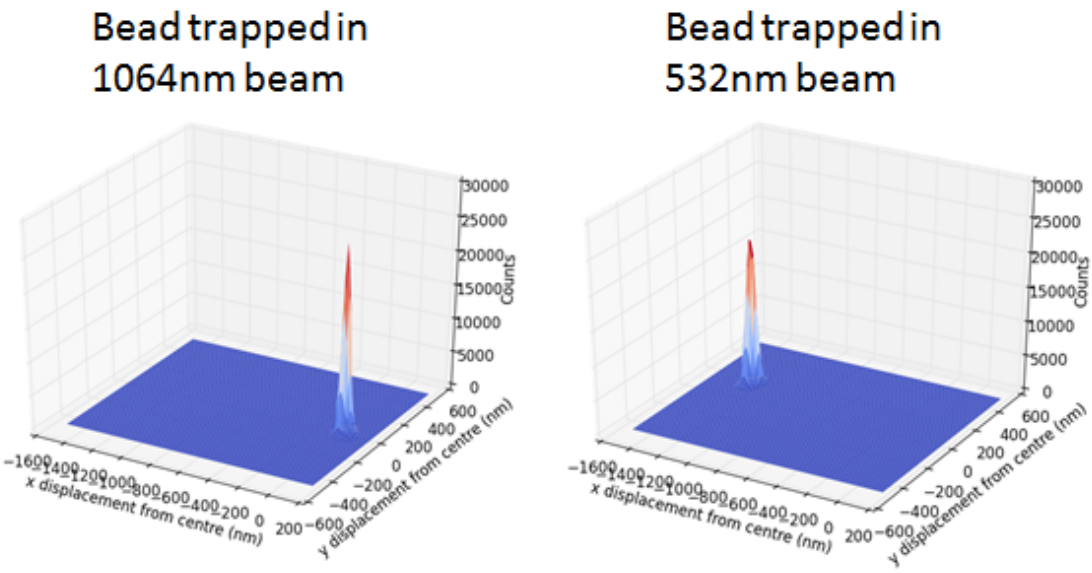


Figure 4.12: *Figures depicting the positions of beads trapped in the 532 nm and 1064 nm traps respectively*

modulated through the use of a mechanical optical chopper, which is comprised of slits which rotate to block light or allow light to pass. This was investigated further by turning the chopper around, thus causing the chopper to rotate in the opposite direction. From Figure 4.13, we can see that turning the chopper around changes the shape of the asymmetric elliptical path the bead motion follows; the bead now moves in the opposite direction. This demonstrates that the laser intensity at the trapping focus is not in a discrete 'on' or 'off' state at any time (a tophat function over time), but rather there is a gradual increase and decrease; this has previously been reported when using a photodetector to detect optically trapped particles using a chopped beam [89]. The effect is considerably more pronounced at higher trapping powers due to the Gaussian profile of the laser beam; the lateral and axial intensity gradients of the focussed beam itself are responsible for the stable trapping of particles, as detailed in Chapter 2, and thus the change in the gradient as the chopper moves is more pronounced and the bead motion is more erratic between the traps. This erratic motion produces an intrinsic instability in the oscillatory system, and hence prevents the phase sensitive detection method being a viable technique to use in a system where chemical reactions may

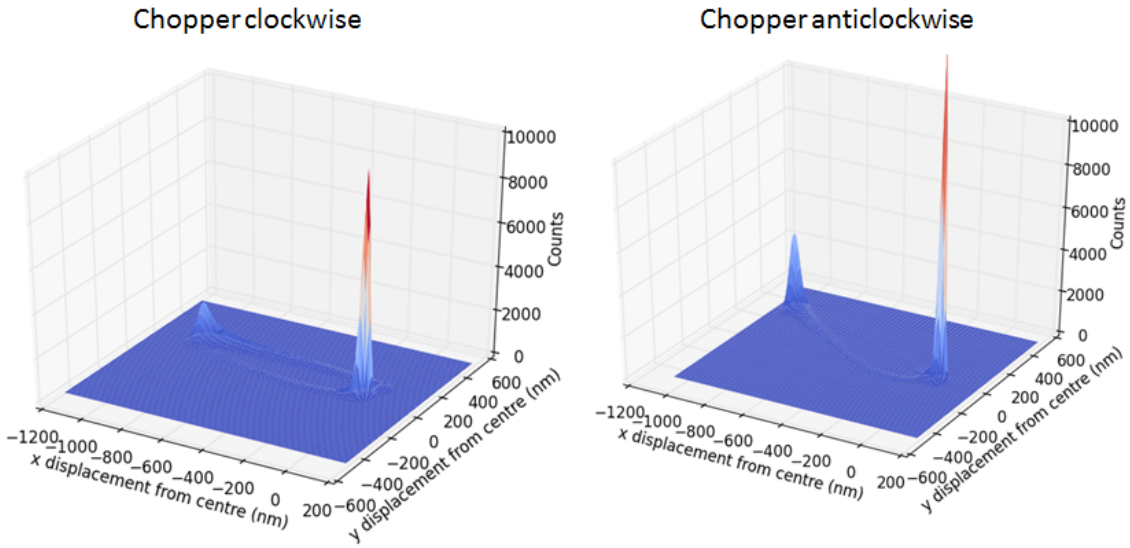


Figure 4.13: *Histograms obtained of the motion of a tracked 3 µm bead trapped between a continuous 532 nm laser beam and chopped 1064 nm laser beam. The chopper is rotating clockwise in the left image and anti-clockwise in the right image, through turning the chopper through 180 degrees parallel to the optical table*

be taking place on a trapped specimen.

## 4.2 Motion tracking in optical tweezers in a changing environment

### 4.2.1 Practicalities of the use of a CMOS camera for tracking a changing bead

When using a camera based method for tracking particle speed, the particle position is found via performing centroiding calculations (described further in Chapter 2) on an area which represents the particle. Typically, an area is selected where only certain pixel intensities are counted as being the particle. It is necessary to select an intensity threshold value in the camera software (that is, a pixel intensity value from 0 to 255 which is subtracted from the pixel intensities of each pixel; thus, no pixels are within the threshold (and thus tracked) at a value of 255 and all are within the threshold at 0) which is high enough to reduce the contributions

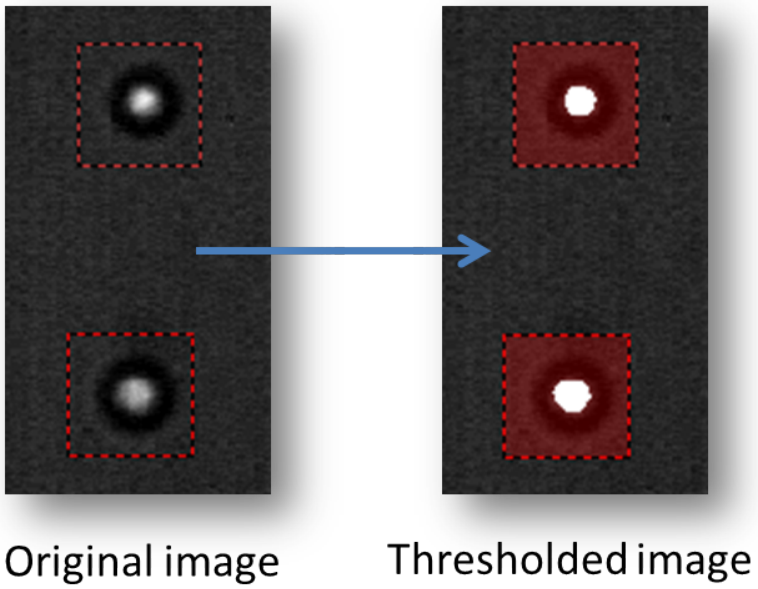


Figure 4.14: *Image depicting an example of the use of thresholding in particle position detection by the smart camera for two trapped 3 µm diameter PMMA beads held 10 µm apart; the white area is the tracked area, and the red area is discounted from position measurements*

of background noise, but also low enough to be able to detect the particle. The thresholded 'image' which is usually tracked is the top surface of the bead through which illumination light is focussed to a white spot, as shown in Figure 4.14.

However, in this experiment, it was found that when crystallisation occurs on a bead, the image on the camera changes, as shown in Figure 4.15. This was found to be more of a problem with the complexer and polymer added, as more particulates were formed and thus spread more across the bead surface. The intensity values in the tracked area therefore change slightly due to light scattering from the particulates, thus there is some obscuring of the bead image, which affects position readings. To counter this, the beads were trapped slightly out of focus and the thresholding adjusted to always be monitoring a sufficient amount of the refracted light through the bead.

It was decided that monitoring several beads at once could be beneficial, as several

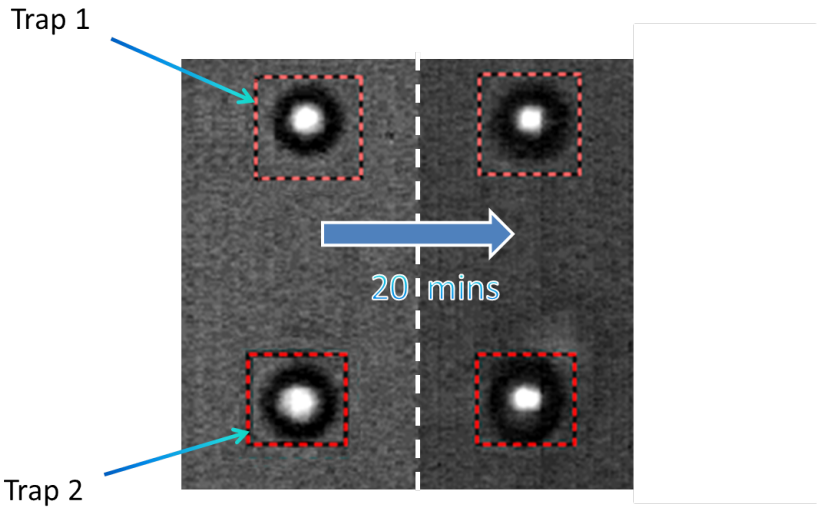


Figure 4.15: *Image depicting buildup of calcium carbonate on the surface of two trapped 3 $\mu m$ diameter PMMA beads after 20 minutes*

datasets of particle tracking data can thus be obtained at the same time, reducing the time necessary for multiple measurements. However, this imposes a further limit on the collection frequency as the beads have to be far enough apart that they do not affect each other through hydrodynamic coupling [90], necessitating an increase in area of the region of active camera pixels (leading to a decrease in the imaging frequency). Increased collection frequency also limits the light reaching the detector, which reduces the contrast necessary for tracking particles; this is further complicated if Raman analysis is necessary at the same time, as the light must be limited to a wavelength range either above or below the wavelength range of the Raman spectrum. This affects the measured power spectrum of the bead motion, which has been discussed previously by Horst et. al. [91] where a camera with a limited bandwidth was used to calibrate multiple holographic optical traps.

As already described in Equation 2.3.13, the power spectrum is given by:

$$S(f) = \frac{k_B T}{2\gamma\pi^2(f_c^2 + f^2)} \tag{4.2.3}$$

which fits to a Lorentzian profile. However, in the case of a lower acquisition frequency, the power spectrum may not fit well to a Lorentzian profile, particularly

in the high frequency 'tail' of the spectrum, and especially for stiffer traps. This is due to the finite image integration times from using a camera not found in higher frequency devices such as photodiode detectors, in which case the camera image may suffer from motion blur. The power spectrum equation is thus altered to take the acquisition time, W, into account [92]:

$$S_{blur} = S(f) \times \left( \frac{sin(W)}{W} \right)^2 \tag{4.2.4}$$

This tends to give an underestimate of the power spectrum, particularly at higher frequencies. The limited frequency of particle measurements also leads to aliasing of the spectrum for corner frequencies approaching the Nyquist frequency, $f_{Nyq}$, which is equal to half the sampling frequency ($f_{Nyq} = 0.5 f_s$). This alters the power spectrum to:

$$S_{alias}(f) = \sum_{n=-\infty}^{\infty} S(f + 2n f_{Nyq}) \tag{4.2.5}$$

which tends to overestimate the power spectrum. We may combine this with the inherent positional detection error (which is present in any particle tracking technique) in the system, assuming a variance of $\epsilon^2$, to give:

$$S_{meas} = \sum_{n=-\infty}^{\infty} S(f + 2n f_{Nyq}) + \frac{\epsilon^2}{2 f_{Nyq}} \tag{4.2.6}$$

### 4.2.2 Calibrating the system with distilled water and a simple carbonate formation reaction

The response of the system was tested whilst distilled water was flown past a trapped bead at a constant speed as a control, as demonstrated in Figure 4.16, over a period of 30 minutes. It was found that the value calculated from the Lorentzian fit for the corner frequency was roughly stable over time, although there are some fluctuations. This is to be expected from the random motion of beads in the trap and the finite time for which measurements are taken; as measurement times are increased, we would expect the standard deviation of the calculated frequencies to decrease. This may also be due to minute fluctuations in the rate of the water

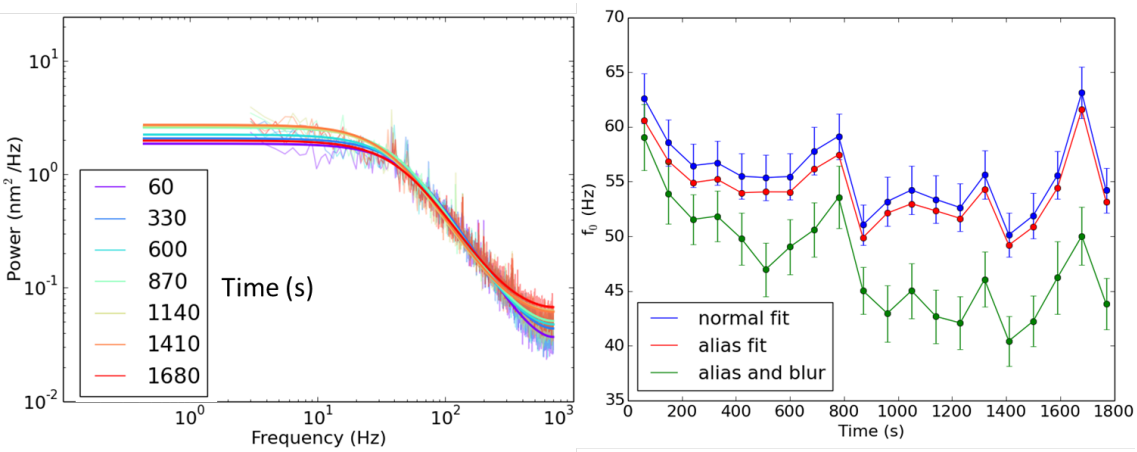


Figure 4.16: *Left: Power spectra of a bead trapped in distilled water only over a period of 30 minutes at a flow rate of 0.5 ml/h, at an output power of 100 mW. Every nth spectrum is plotted for clarity. Right: change in calculated $f_c$ using a standard Lorentzian fit (blue), the fit from equation 4.2.5 which takes into account aliasing (red), and the fit from aliasing, blur and errors in equation 4.2.4*

flow. Fluctuations may be observed due to water which is not completely clean being used; thus, efforts were taken to ensure that the channels and the connecting tubing were cleaned well after measurements were taken, so there were minimal particulates remaining in the distilled water.

A solution of distilled water, sodium carbonate and calcium chloride was then flown past the trapped bead. From Figure 4.17, we can see that there is a change in the power spectrum over time as the corner frequency increases quite rapidly after 240 seconds of continuous fluid flow past the trapped bead. The power spectrum of the 'tail' of the plot also increases, which indicates a change in the intrinsic Brownian motion at high frequency due to the buildup of calcium carbonate. It is important to note that the change in corner frequency over time does not indicate a change in the trap stiffness, but rather a perturbation of the laser spot trapping the bead, at which point the linear relationship between stiffness and corner frequency may no longer apply. Increasing a trapped bead's volume tends to increase the corner frequency due to both the increase in viscous drag and the dependency of the trapped stiffness on bead radius and hence volume, which for Mie particles is non-linear and complex even when not taking into account a non-uniform in-

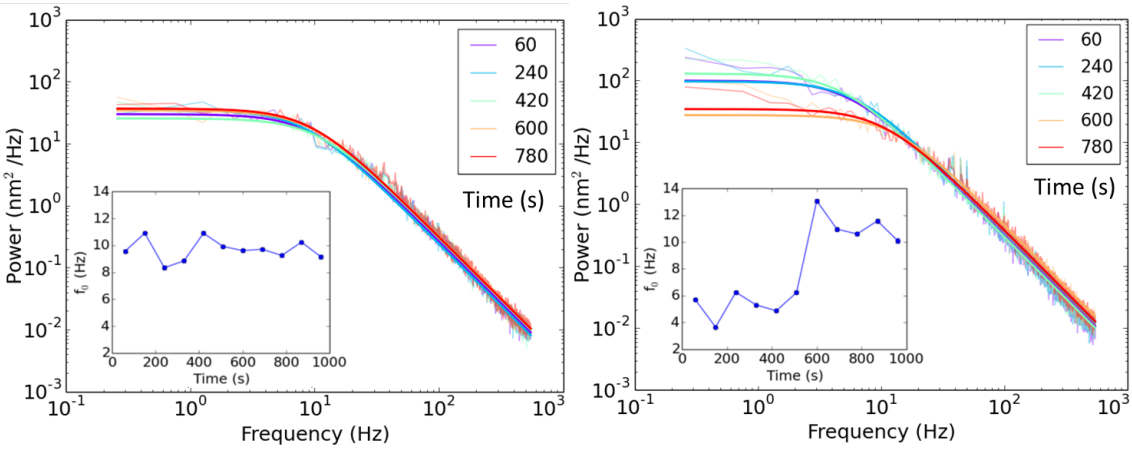


Figure 4.17: *Power spectra of two beads trapped in separate optical traps, in a solution of beads mixed with calcium chloride and sodium carbonate only. There is more power in the second trap than the first; this is a consequence of using the SLM to produce the traps as some light may be directed into traps more than others*

crease [17].

This was attempted with several more beads, examples of which are discussed in [93]. To increase the probability of observing a distinct change in the power spectrum of a trapped specimen, it is beneficial to trap more than one bead and record the power spectrum of two beads at once, which was achieved through the use of the SLM (with a corresponding decrease in the power in each trap), and through looking at two areas at once with the smart camera. An example of this may be seen in Figure 4.17. While one bead's power spectrum has not changed, and thus no coating has taken place, the other bead shows a clear change in corner frequency over time which indicates a change in the bead's environment; this change could either be due to a change in the flow rate, due to particulates also being pulled into the optical trap, or due to the bead itself being coated.

While using this method there is not enough information to deduce the mass of calcium carbonate buildup from changes in the corner frequency of the power spectrum, as the inertial term containing the mass drops out of the Langevin equation when we undertake the power spectrum calculation (as discussed in Chapter 2), monitoring the power spectrum over time nevertheless provides us with a powerful

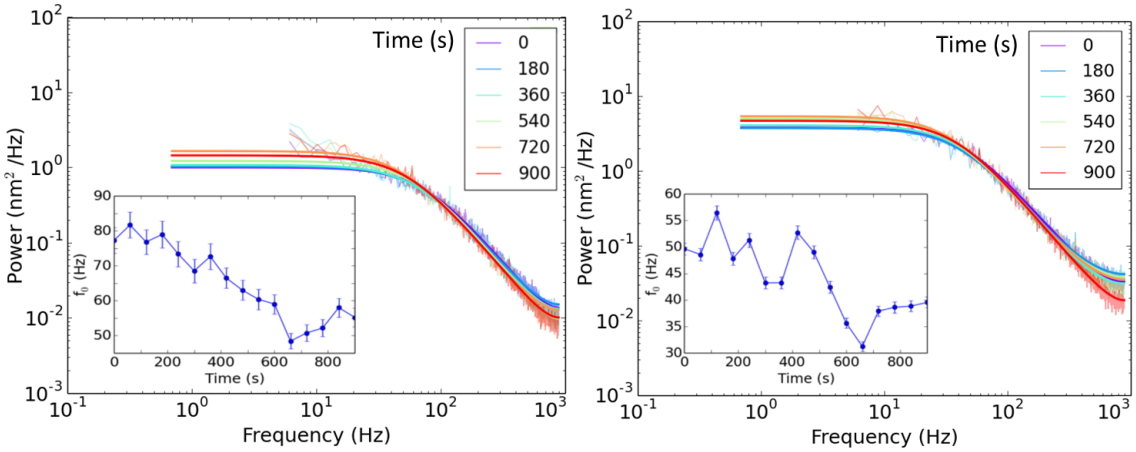


Figure 4.18: *Power spectra of two beads trapped in separate optical traps, in a solution of beads mixed with the solution described in Table 3.1, Chapter 3 (with calcium chloride, sodium carbonate, chelating agent and sulphonated polyacrylate). There is more power in the first trap than in the second, as the SLM has directed more light into this trap. Inset: the calculated corner frequencies*

tool for deducing when there is buildup on a bead. It is possible to increase the time resolution of this by decreasing the time over which position measurements are taken, although this introduces more errors by decreasing the amount of block averaging we can do during the power spectrum calculations.

### 4.2.3 The change in the power spectrum for a simulated dishwasher solution

We then introduced the solution with both the complexer and polymer and trapped PMMA beads while this solution was flown past. It was noted that in this case, far more particulates were present in the solution than when these additives were not present. This is expected due to the role of the complexer and polymer in the solution; the polymer is added to suspend small particles of calcium carbonate that form, and the complexer is designed to bind with these particles to prevent the formation of larger crystals. Thus, there is a noticeable reduction of large crystals flowing past the trapped specimen.

This difference in particle size has an unusual effect on the power spectrum, as

shown in Figure 4.18. Instead of the increase in corner frequency witnessed in Figure 4.17, we obtain a very gradual decrease in the corner frequency. Another unusual effect is the behaviour in the high frequency region, where the power spectrum levels off due to aliasing; over time, we notice that this aliasing effect actually decreases, which is more dramatic at lower trapping powers. These effects are unusual, as we would expect the corner frequency to decrease with increasing build-up. There are two possibilities of what could be happening to alter the measured particle motion in such a way; the particulates are not actually adhering to the bead but are being trapped in the solution itself, or more likely due to the unusual high frequency behaviour, the particulates are obscuring the bead to the point that it is not tracked properly. This highlights the limitations of the system, as the binary thresholding method used in the smart camera means that large amounts of build-up tend to alter the bead surface. However, it does still show that there is something happening on the surface of the trapped bead, and so despite its limitations, tracking particle motion may prove a viable technique.

In summary, in this chapter the usefulness of the microfluidic Raman trapping system for simulating and analysing the reactions in a dishwasher is explored and discussed. It was found that the system is good for analysing particulates which form in the solution as these can be relatively easily trapped, but in turn this leads to more difficulty in analysing particulates forming on small beads; this is due in part to the ambiguity of whether the particulates are being attracted to the trapped bead or whether the particulates are adsorbed to the bead. It is also very difficult to detect material on the bead surface via Raman spectroscopy at the beginning of the calcium carbonate forming reaction, as only very thin layers are produced. However, we can observe changes on the bead surface through camera imaging and to an extent quantify them through the use of power spectral analysis; with improved tracking methods, this could prove a more promising method for quantification. Raman spectroscopy is a rather more useful technique on larger surfaces, such as the surface of the channel, and could prove useful if channels of different materials were analysed in this way. It was also found that the phase sen-

sitive Raman detection method is too unstable to use in a system where the beads are already disturbed by build-up and/or fluid flow; the use of an alternative beam chopping method to a rotating mechanical chopper could possibly lead to more stability in this system. The system therefore has limited use for analysing in-situ reactions on bead surfaces due to the size of the beads and the small amounts of calcium carbonate formed.

# Chapter 5

# A Fast Spectroscopic Method for the Quantification of Laundry Detergent Performance

*This chapter details the development of a new spectroscopic method for quantifying the level of staining on small fabric samples. This has been designed as an improvement on a current method used by Proctor and Gamble to assess the performance of detergents on stained fabric*

## 5.1 Introduction and aims

The modern laundry detergent industry has seen considerable changes over the past 40 years, and the field is still seeing developments today with an outlook for using cooler washing temperatures, more environmentally friendly chemicals, higher efficiency (so less can be used) and resulting in cleaner fabrics. A large amount of time, work and effort are expended in the production of new washing machine detergent formulations and it is therefore necessary to have high-throughput, robust methods of quantifying their performance. The current method employed by Proctor and Gamble for testing their detergents involves the analysis of many different detergents at one time. This is carried out in pharmaceutical standard high throughput well plates with 96 circular wells (commonly used for testing biological

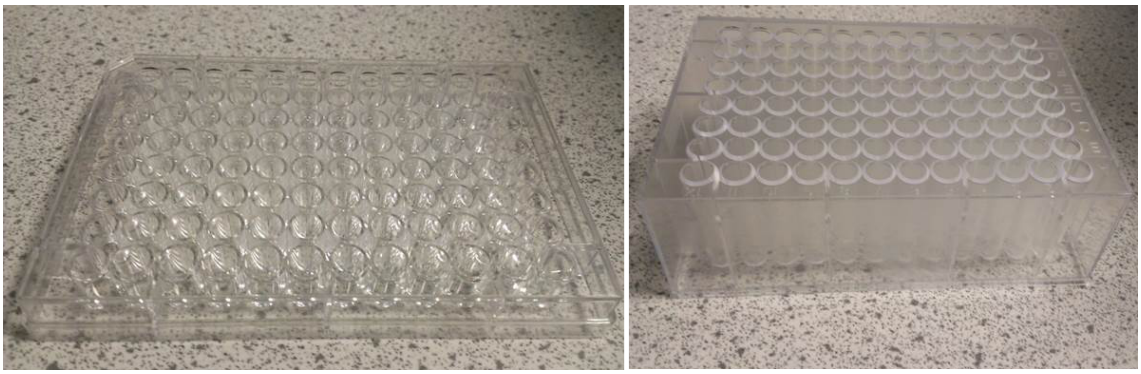

Figure 5.1: *Photographs of the 96 well plates. The image on the right shows the plate used for washing the samples, and on the left is the plate under which samples were analysed*

assays [94]). Circular samples stained with a variety of common stains are placed in the wellplate on the right of Figure 5.1 with test-tube like protrusions along with the formulation to be tested, and mixed using ball-bearings and magnetic stirrers. The fabric circles are then tipped into the wellplates on the left and allowed to dry. The samples are then analysed in a white light imaging box. The cleanliness of the fabric is then determined by quantifying the intensities of the individual pixels from the TIFF images obtained. The analysing system itself is thus based on the concept of what is perceived to be clean by the eye, and is therefore suited for use as a demonstration tool for potential customers of how well detergents work. However, subtle changes in cleanliness of fabric are difficult to accurately quantify via this method, and 'invisible' stains such as grease, which affect how clean fabric 'feels', cannot be detected at all.

It would be advantageous to develop a system in which subtle changes could be recorded, as this would allow detergent researchers to detect the presence of stains that would not normally be visible using this method but may still render the fabric dirty. For example, a fabric circle with a greasy stain on it would be passed as clean under this system, as grease is invisible under white light imaging. Adding to this, there is also the problem of different types of fabrics having weaves of varying thicknesses. At high resolution, this gives rise to the visibility of holes in the sample (as shown by the lighter regions in Figure 5.2, where the imaging light

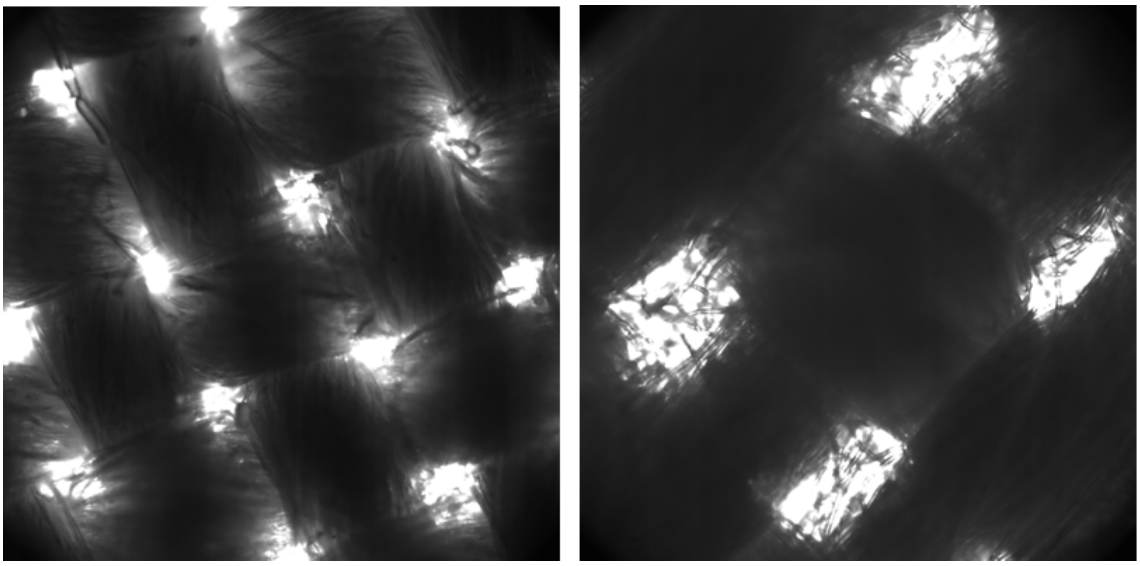

Figure 5.2: *Microscope images at 10x magnification of thin weave elastane (left) and thick weave polyester dacron (right) fabrics. The light regions indicate areas where there is no fabric and thus light transmission is high. In white light imaging, pixel intensities which would be obtained from these areas would not be valid*

is blocked by the fabric but can be detected through the holes). This appears as a dark area in the obtained white light image, and if not adequately compensated for, may underestimate the efficacy of detergent performance. The fluorescence of certain stains under different excitation wavelengths has been studied extensively in the forensic sciences [95], and therefore the possibility of this as a stain quantification technique was also investigated.

## 5.2 Theory

It was decided that a spectroscopic method of analysing samples, using not only scattered but also transmitted light (as the well plates are transparent), and using discrete wavelength ranges rather than a full white light spectrum, may allow additional information on the cleanliness of a fabric sample to be obtained. We used the wavelengths from five fibre coupled LEDs to test whether it was possible to detect stains from their fluorescence, as the level of staining would then be proportional to the amount of emitted light from any excited stain.

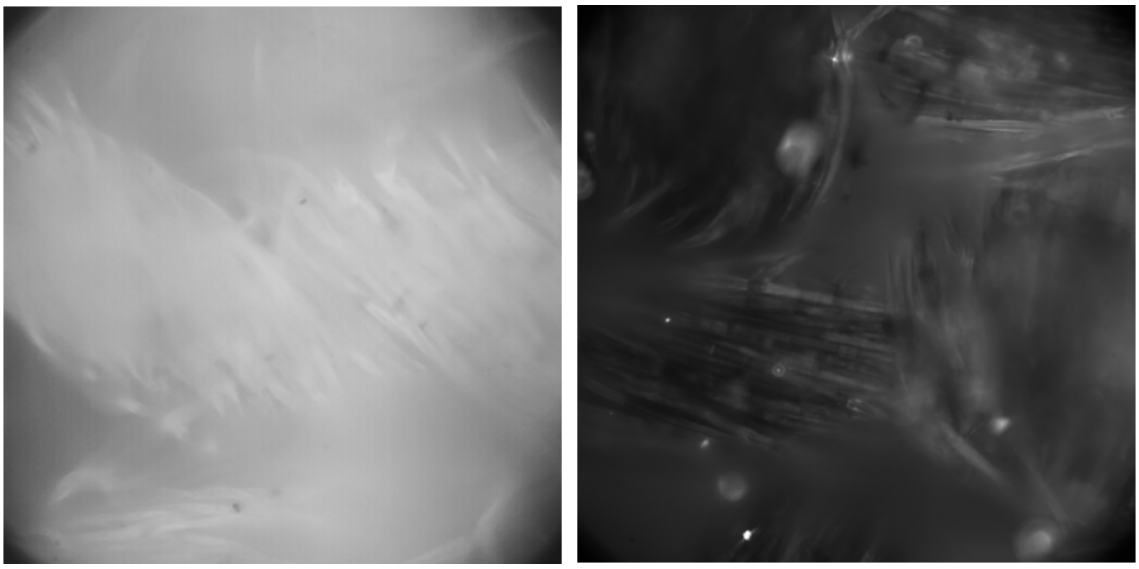

Figure 5.3: *Confocal microscope images at 10x magnification of fluorescence under ultraviolet illumination. The image to the left is of clean washed fabric showing fluorescence of optical brighteners, and the image on the right depicts the fluorescence of dried motor oil on fabric*

Unfortunately, this did not prove to be a viable method as little to no emission light was detected. The fluorescence was investigated using a more powerful light source, and Figure 5.3 shows the images obtained under a microscope with higher intensity ultraviolet light as an illumination source for fluorescent samples. On the right of Figure 5.3 is fabric (elastane) stained with motor oil, which shows a very small amount of fluorescence in small patches. While this fluorescence is visible using the microscope, it is not enough for us to detect easily using the spectrometer, and certainly not quickly enough to be of any use in a high throughput system. It is also entirely possible that the stain fluorescence may be quenching as the stains themselves dry on the fabric, and thus stains are more fluorescent when in liquid forms. As a comparison, optical brighteners (a common additive in modern detergents) display a large amount of overall fluorescence, as shown on the left of Figure 5.3; the fabric is evenly covered during the washing process and thus we obtain fluorescence from all areas of the fabric. Therefore, while this may be a good method for quantifying the effect of optical brighteners themselves on fabrics, it is not powerful enough for the analysis of dried stains on fabric.

Of note, however, was that different incident light wavelengths were reflected and transmitted differently by fabric coated in different stains, and some stains even cause a slight change in the full width half maximum of the spectrum. This feature was utilised in this experiment by measuring the spectra at different wavelengths in transmission and reflection as a method of building a database of spectral 'fingerprints' for stains at different incident light wavelengths. These spectra were then compared to those of washed stains and clean fabric to quantify how clean the fabric was, and thus the efficacy of the detergent.

## 5.3 Methodology and experimental setup

Eight different stains and clean 'reference' fabric were examined in 9 separate wells. The fabric used was a closely-knitted elastane blend which had very small holes, and each sample was analysed over 5 different areas of the fabric to compensate for the weave of the fabric. Five 400 $\mu$m diameter, 0.21 NA fibre coupled LEDs were used to illuminate the fabric samples, with peak wavelengths of 396 nm (UV), 468 nm (blue), 516 nm (green), 594 nm (yellow) and 634 nm (red). Figure 5.4 shows the optical setup used to direct light onto the fabric and collect light reflected and transmitted by the fabric. Light from the fibre coupled LEDs was collimated and sent through a beamsplitter, and then focussed onto the fabric sample. Light reflected from the fabric was directed up through the same focussing lens and reflected by the beamsplitter onto another lens, which focussed the light onto a 400 $\mu$m diameter 0.22 NA fibre for detection by the spectrometer. The spectrometer used was a USB2000+ spectrometer by OceanOptics. Light transmitted by the fabric was expanded onto a mirror which directed the light to another focussing lens which focussed the light onto another identical fibre connected to the spectrometer. Thus both reflection and transmission measurements could be obtained for the same portion of fabric with this setup via simply swapping the fibres.

Measurements were recorded by a program written in LabVIEW which collected the spectra obtained by the spectrometer for five evenly spaced areas of the fabric

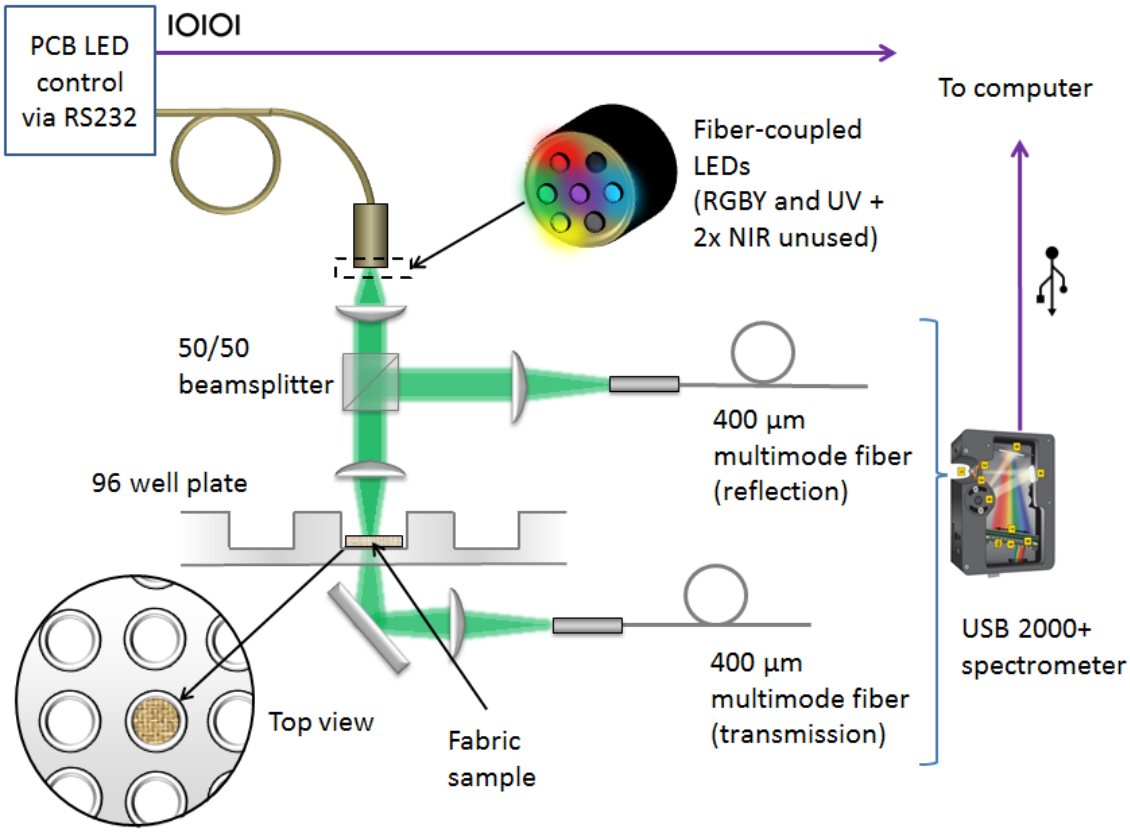


Figure 5.4: *Schematic of fabric analysing instrument, with the 96 well plate integrated into the system*

and subsequently averaged them for each LED colour, in both reflection and transmission; thus the system was partly automated, with manual translation stages and a program which switched between LED colours. There was some variation in the maximum intensities of each raw LED spectrum, and this was possibly due to discrepancies in the brightness of the LEDs themselves, particularly for the green and ultraviolet LEDs. Taking this into account, integration times of 90 ms were used for the blue, yellow and red light, whereas 800 ms was used for the green and 750 ms was used for the UV light, to try and give a similar maximum measured intensity for each light wavelength.

The stains analysed are shown in Figure 5.5. A range of sticky (Ribena and squash), greasy (olive oil), dark (soy sauce, strong tea) and light (fruit tea and

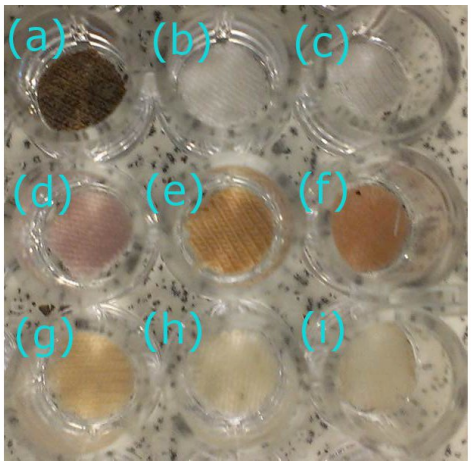


Figure 5.5: *Image of the fabric samples in the well plate coated with different stains: (a) soy sauce, (b) unbleached reference cloth, (c) old cloth, (d) fruit tea, (e) strong stewed tea, (f) Ribena, (g) weak tea, (h) olive oil and (i) orange squash*

weak tea) stains were used so that a good range of results reflecting common stains found in the everyday could be obtained. Each stain was placed in a different well. The reference fabric used was previously unwashed clean cloth (and thus not optically brightened by detergents previously). 'Old cloth' refers to reference fabric which had been left out in the laboratory for a few days, to test if we could detect very subtle changes using our system such as dullness in clothes which have simply been left in storage.

Three washed stains were also analysed, as a comparison; these were samples which had previously been stained with olive oil, soy sauce and tea, and then washed in detergent. This was carried out to investigate the difference in cleaning when faced with dark and greasy stains that are commonly encountered in everyday life.

## 5.4 Initial Results

Figure 5.6 shows the reflected light spectra for each LED colour for elastane fabric stained with olive oil, before and after washing; the range of each LED is also shown. The peak value increases if more light is reflected by the fabric; as we

would expect, the reflected intensity increases when the fabric has been washed, as the oil absorbs light. We can also see a very small amount of fluorescence for washed fabric when the UV LED is used in the region between 440 nm and 520 nm, which originates from the use of optical brighteners in the detergent.

From the spectra obtained, it was decided that the peak values and full width half maxima of the data would provide most of the information required to compare how well samples had been washed. The data were analysed using code written in Python. The peak values were obtained from finding the maximum intensity of the data via differentiating (that is, finding the maximum value of each curve) and the full width half maximum was found from fitting a univariate spline and finding the values at half the maximum value found previously. Figure 5.7 shows the washed and unwashed stains as a comparison. The data was normalised by dividing the maximum of the peak for the stain by the maximum of the peak for the clean reference fabric for each LED wavelength.

From Figure 5.7, it is evident that samples such as soy sauce do not reflect much light through the spectrum nor transmit it, but when washed the intensity values become closer to those of the reference across the spectrum of colours, which is a simple result that we would expect. This provides some validation of the method, as compared to simple visual observation made by customers.

Figure 5.8 shows the relationships between the LED and full width half maximum of the data obtained for washed and unwashed stains. We can see that for the transmitted light, there is hardly any spreading of the spectrum for the washed fabric, but the spectral profiles widen considerably for reflected light when fabric is washed. Olive oil interestingly shows a narrowing of the spectrum for the washed and unwashed fabric in reflection, but the FWHM then increases in transmission, and for soy sauce the opposite is the case. This may be due to soy sauce being a very dark stain which blocks holes in the fabric, restricting the transmitted light to a point where the FWHM is affected, which conversely means that olive oil, which

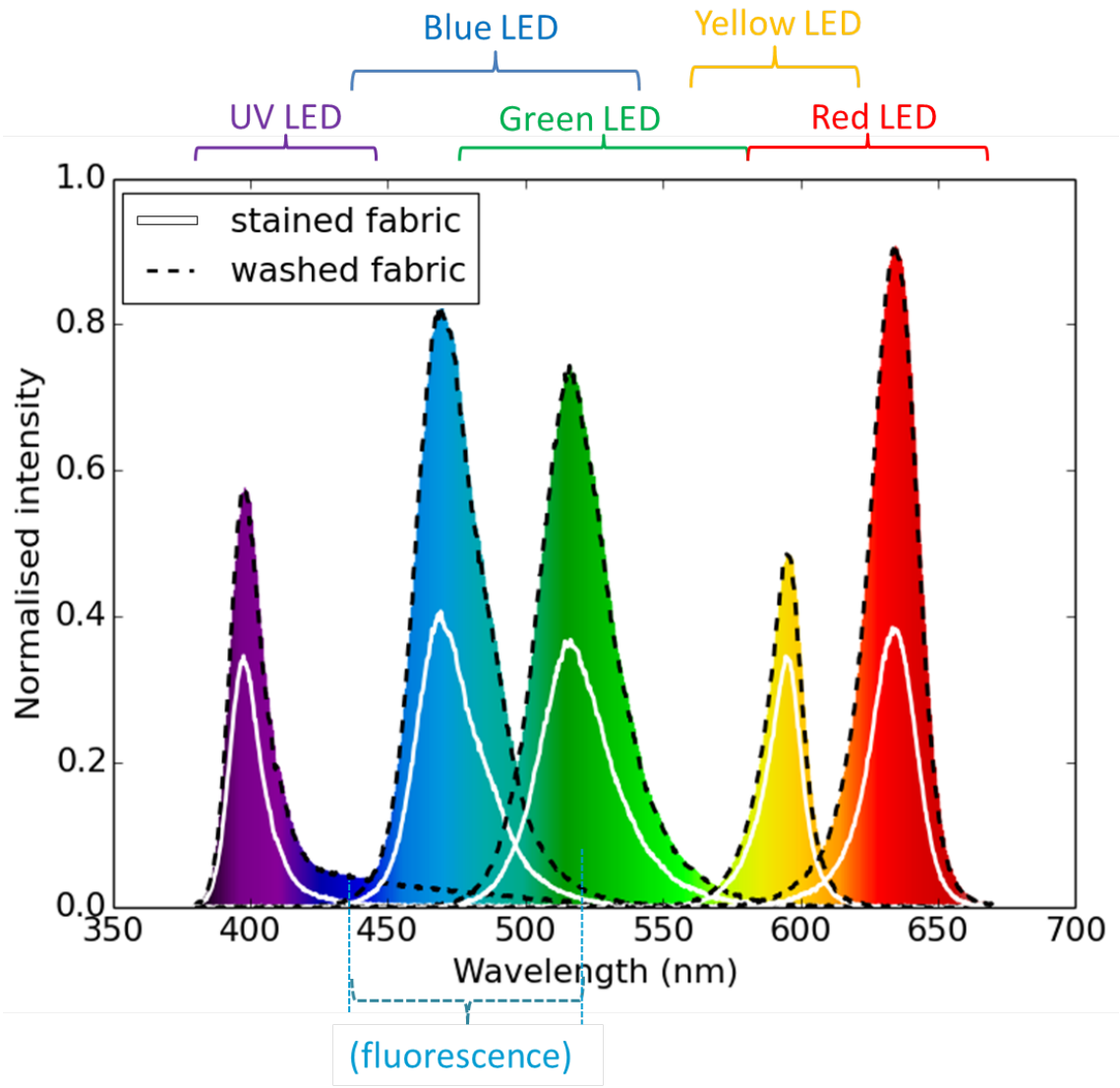


Figure 5.6: *Example of the spectra obtained in reflection when illuminated by each LED for a piece of fabric stained with olive oil, before (solid white line) and after washing (dotted line), and the corresponding LED bandwidths. Of note is the UV spectrum after washing, where the fluorescence of the optical brighteners under UV light can be seen*

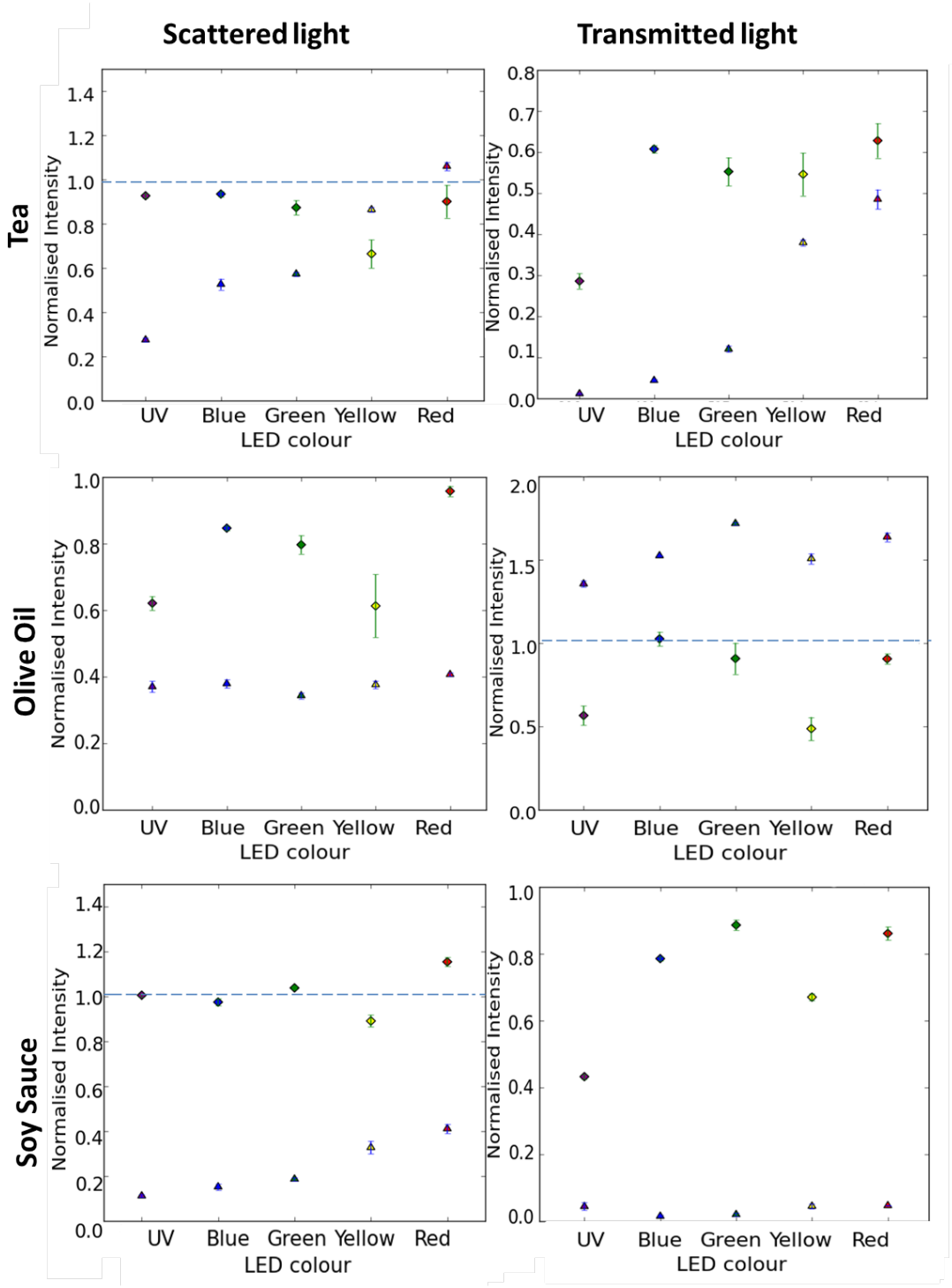


Figure 5.7: *Results obtained as graphs of normalised maximum intensity vs input wavelength for tea, olive oil and soy sauce, where ∘ indicates washed fabric and △ indicates unwashed fabric. Results on the left are for reflected light and on the right are for transmitted light. Error bars are the standard error on the 5 values obtained for each measurement. The dotted lines indicate the transmitted and reflected intensities of light incident on clean, previously unwashed fabric, which was used as the normalisation factor*

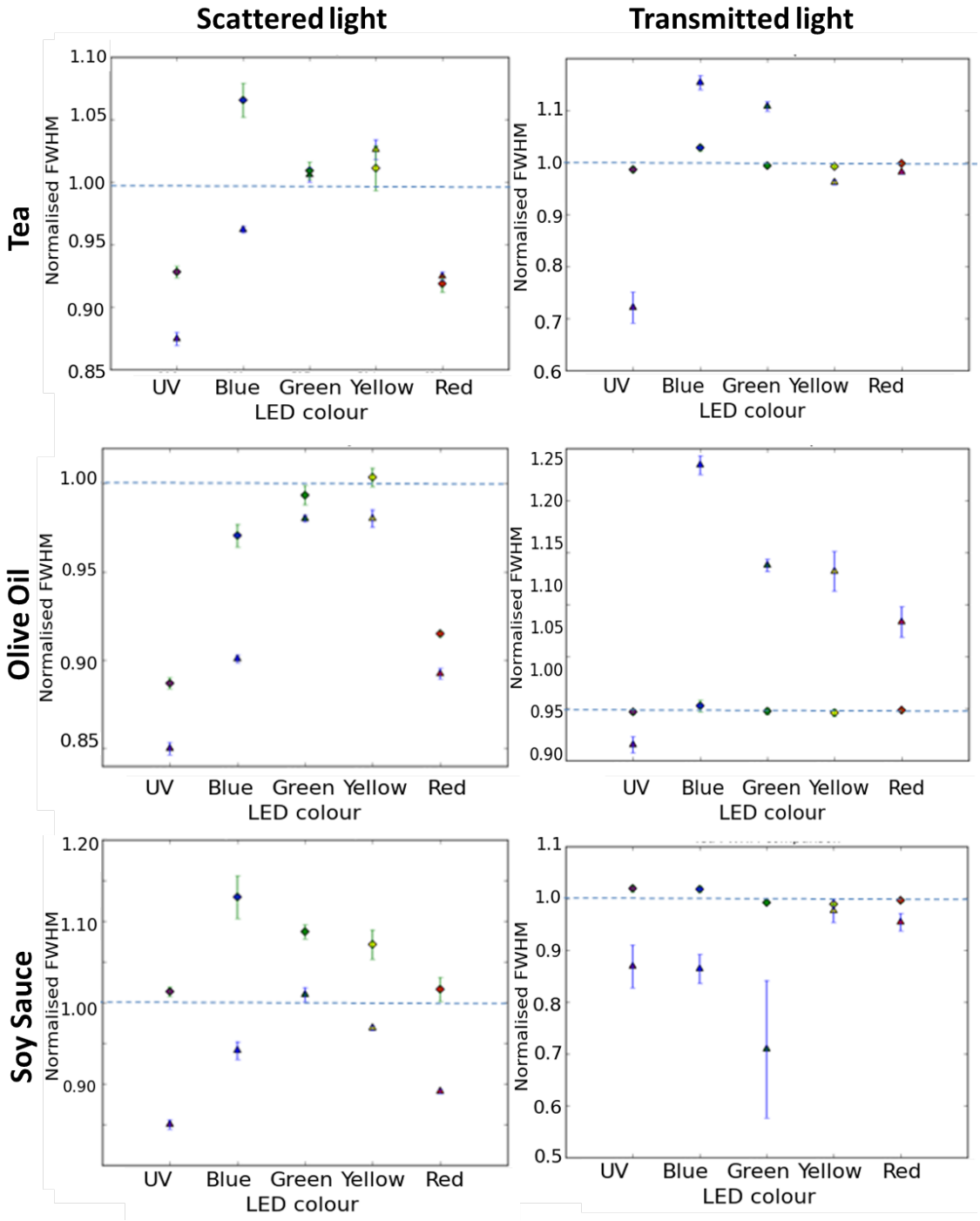


Figure 5.8: *Results obtained as graphs of normalised FWHM vs input wavelength for tea, olive oil and soy sauce, where ○ indicates washed fabric and △ indicates unwashed fabric. Results on the left are for reflected light and on the right are for transmitted light. Error bars are the standard error on the 5 values obtained for each measurement. The dotted lines indicate the transmitted and reflected intensities of light incident on clean, previously unwashed fabric, which was used as the normalisation factor*

increases light transmission through the fabric, also increases the FWHM. This is due to the holes in the fabric now being filled with oil due to surface tension. Given that the refractive index of oil ($n_{oil} = 1.47$) is closer to that of elastane ($n_e \approx 1.5$) than air ($n_{air} = 1.00$), light rays approaching the fabric at an angle are transmitted rather than reflected through the fabric; thus the reflected light is reduced and the transmitted light is increased.

It is clear that the data obtained, however, has many different properties - whether the data has been taken in transmission or reflection, what colour the light was, what the stain is and whether the sample was clean or dirty - and it is not trivial to quickly deduce the extent to which these properties contributes to fabric cleanliness.

## 5.5 Using PCA to reduce the dimensionality of data

Given that the experimentally obtained data has many dimensions which makes it quite difficult to compare all the stains at once, a suitable method to use to compare the stains is Principal Component Analysis (or PCA), which is a simple method of eigenvector-based multivariate analysis. Using PCA allows us to reduce the dimensionality of our data but includes the contribution from all the different wavelengths of light we are shining on our sample and takes into account the levels of light transmitted and reflected, and the width of the peaks obtained. PCA works on the idea that possibly correlated variables can be converted to a set of uncorrelated variables called principal components which are orthogonal ; this technique is commonly used in applications with many variables, for example facial recognition [96] and for feature extraction in hyperspectral imaging [97]. PCA particularly finds application where the most important variables in an experiment are as yet unknown.

As a real world example, if we are given a set of data relating to the perfor-

mance of athletes, we may have many variables in an event such as a decathlon where 10 events take place; we may have a list of distances for discus throwing and long jumps, and sets of times for races. We may then wish to look at the variability of the performance of individuals in the race, whether there is any correlation between the variables themselves, for example, if athletes who excel at one event also tend to excel at another, and whether we may group individuals into sets to predict performance. An example of principal components after the application of PCA in this case may be the speed and strength of athletes; thus this may lead to grouping of athletes into these skill sets.

The PCA calculation itself consists of a linear transformation where a $N \times a$ matrix $X$ is transformed to the $N \times b$ matrix $Y$. The mean of the data is first found and subtracted, and then the $a \times a$ covariance matrix is calculated. This is given by [98]:

$$C = \frac{1}{N-1} X^T X \tag{5.5.1}$$

The diagonal of this matrix, $C_{i,i}$ is the variance of the variable $i$, and off diagonal elements $C_{i,j}$ are the covariance values between the variables $i$ and $j$. The eigenvectors of this covariance matrix are then calculated. Then, $b$ eigenvectors are selected which correspond to the largest $b$ eigenvalues to be the new basis. These eigenvectors are the principal components, while the eigenvalues are the individual values.

The first principal component always has the largest variance and each succeeding component has the next highest. It is important to note that each principal component does not necessarily correspond to one variable; it may be a combination of several. This is particularly the case in facial recognition, where facial images are taken and projected onto space composed of 'eigenfaces'; the variation among known face images is thus encoded as many eigenvectors but these generally do not correspond to certain facial features; for example, mouths and noses. In this work, PCA is utilised for the comparison of stains given spectral width and height data, and to observe whether there is any grouping of dirty and clean stains, so we

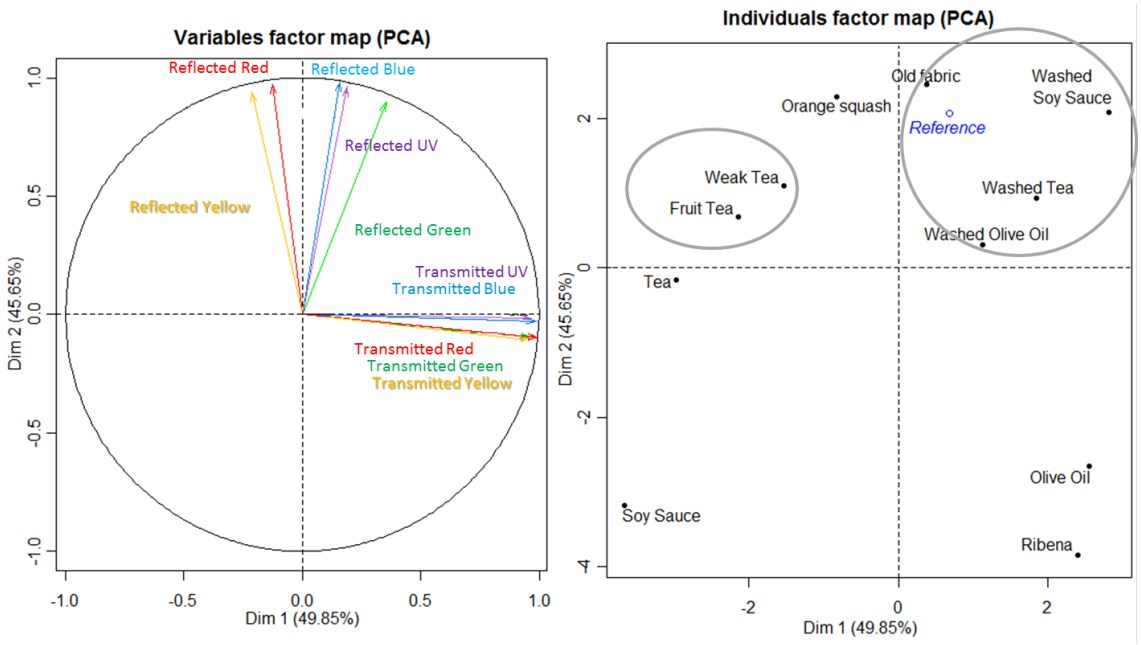


Figure 5.9: *Graphs showing the weighting of the intensities for different stains (individuals) and different illumination wavelengths (variables) along the principal axes*

can categorise if a piece of fabric is clean or not, and how clean; that is, whether it is possible to characterise individual stains by any variables used in the experiment.

A program called 'FactoMineR' written in R by Husson et. al. [99] was used to process the data and obtain the principal components. The program subtracts the mean from all data, calculates the covariance matrix of the data and then calculates the eigenvalues and eigenvectors of this matrix. The principal components were calculated for the peak light intensities transmitted and reflected by the fabric samples by each LED. The output figures give the weighting of both the variables (given as a correlation circle graph with the variables as vectors; longer arrows mean that the variable contributes more to the principal components) and the individuals along the calculated principal components.

We can see from Figure 5.9 that stains in the lower left quadrant of the individual factor map tend to be stains with low light reflection, hence darker stains would appear here, and stains with high transmission are in the lower right quad-

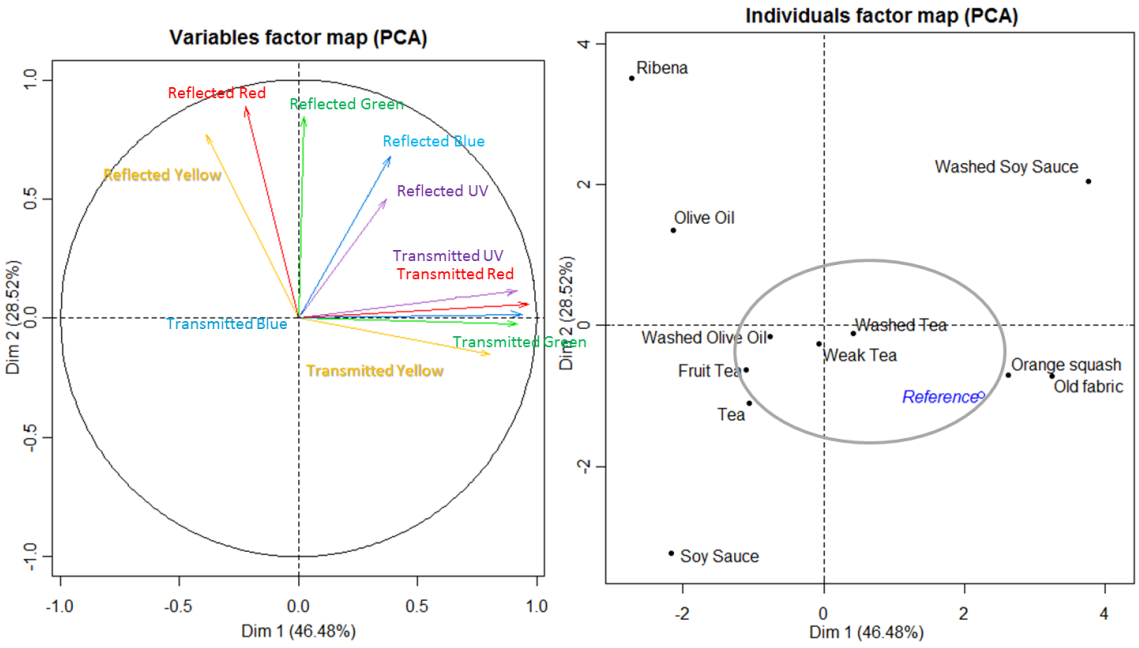


Figure 5.10: *Graphs showing the weighting of the FWHMs for different stains (individuals) and different illumination wavelengths (variables) along the principal axes Dim1 and Dim2*

rant, so greasier stains tend to be in the lower right. Stains in the top right are the cleanest, as circled, indicating high light reflection and a balance in the amount of transmitted light. The least visually obvious stains, weak tea and fruit tea, also seem to be grouped together. The biggest change in dirty and washed fabric is demonstrated with the soy sauce stained fabric, suggesting that the detergent used was very good at washing obvious stains, but not as good at washing greasy invisible stains. We also used PCA on the FWHM values obtained, again using FactoMineR, and obtained different principal components related to the spreading of the different LED spectra in both reflection and transmission.

From Figure 5.10, we can see that there is no longer a clear grouping of clean and dirty fabric. However, it is interesting to note that the dirtier stains such as olive oil, soy sauce and Ribena have very different values of the second principal component (Dim2). The greasier stains tend to be found in the top left quadrant of the individual factor map, while 'normal' stains are clustered around the horizontal axis (as circled), suggesting little to no spreading of the spectrum in transmission

but some spreading of the reflected light. Washed soy sauce was actually one of the stains most removed after washing, and it shows a large amount of spreading of the UV light. This spreading may partly be due to the fluorescence mentioned earlier due to fluorescent additives in washing powder under UV light; possibly this suggests that looking at the fluorescence of fabric may be a good way to quantify how much stain has been removed from a stained fabric sample.

## 5.6 Conclusions and Further Work

Looking at principal components allows us to look at the large quantity of multi-dimensional data we have in a simpler way, though we lose some information in the process. From performing PCA on the preliminary data obtained, it is clear that there is definitely some grouping of the cleanest fabrics for higher values of both principal components, and a general spread of the stained fabric - greasy stains are grouped in a different area to non-greasy stains, and thus it is possible to quantify how greasy a stain is. For analysis of the washed fabric, further testing will be required with different washed stains, and possibly with different detergents and the same stain to look at subtle changes.

In the data collected, unbrightened fabric was used as a reference for normalising values; however, most clothes people wear will have been pre-washed and will thus appear brighter and cleaner, so pre-washed fabric may be more useful as a control fabric for comparison with washed stains. This will affect the normalisation of the intensity values obtained for reflected and transmitted light, especially for UV and blue light.

As the system we have is quite small, with further development it should be possible to incorporate this into a high throughput system with the optical system remaining stationary while the samples are moved. It should also be possible to use the system to eventually look at coloured fabric and look at the fading of dyes over time. In particular it was found that for dyed fabric, some fabric dyes fluoresce

under light, and the current system would not need to be modified significantly to include this utility. We would expect that as the fabric fades, the amount of fluorescence detected would provide the functionality to quantify how much dye remained in the fabric.

# Chapter 6

# Towards a High Throughput Microfluidic System for Monitoring the Reactions in Hair Dye

## 6.1 The Problem

When purchasing hair dye, it is, perhaps obviously, important to be able to predict the development of colour, as mistakes may lead to embarrassment and in the case of salons, lost customers! It is important that companies such as Proctor and Gamble are able to test batches of hair dye, including new formulas, to avoid such errors. Hair dye is a product which changes colour over time through the addition of an oxidising agent, such as hydrogen peroxide, and a catalyst, such as iron or copper chlorides, which speed up the decomposition of hydrogen peroxide into oxygen and water.

To monitor the rate of such a reaction where there is a change in colour, optical spectroscopy is an ideal choice, and typically absorbance spectroscopy is used by P&G to compare the white light spectra of the dyes over time and hence monitor the rate of hair dye development. This allows a library of absorbance spectra

to be built from many measurements as a standard, and batches of hair dye which fall outside certain defined parameters in this library are rejected. However, this method requires a large amount of user input and fairly large amounts of samples.

It would be useful to develop a system in which the reaction may be undertaken in a small volume with the ability to control the reaction at small scales. Microfluidic channels, mentioned extensively in this thesis, are ideal for reactions where speed, high throughput and control are essential. In this chapter, we discuss the development of an optical system to aid P&G in the production of a new hair dye testing system with minimal user input. We then discuss the possibility of creating a miniature production line where reactions of different chemicals to make different dyes may be carried out and their absorbance spectra analysed.

## 6.2 Theory of reaction kinetics and absorbance spectroscopy

The rates of simple chemical reactions are modelled by rate equations, which link the rate of a chemical reaction to the concentrations of the reactants. While the concentrations of reactants may be difficult to calculate in situ, we may deduce them from the knowledge that the absorption of light through a substance is related to the concentration of the material through which the light is travelling. The Beer-Lambert law relates the absorbance of a non-transparent material to its properties by:

$$A = \epsilon l c \tag{6.2.1}$$

where $\epsilon$ is the molar absorption coefficient (a measure of how strongly a chemical species absorbs light of a certain wavelength), $l$ is the path length (that is, the distance the light travels through the material) and $c$ is the concentration. Thus we may model the concentrations in a reaction via the absorbance and use these in the rate equations.

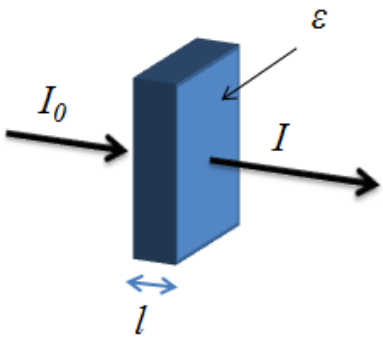


Figure 6.1: *Figure showing the attenuation of light of initial intensity $I_0$ attenuated through a material with molar absorption coefficient $\epsilon$ and path length $l$*

As a beam of light travels through a substance, as shown in Figure 6.1, the intensity becomes weaker according to:

$$A = -\log_{10}\left(\frac{I}{I_0}\right) \tag{6.2.2}$$

where $A$ is the absorbance, a unitless quantity, $I_0$ is the intensity of the light incident to the material, and $I$ is the light intensity after attenuation by the material.

The rate of a simple reaction is related to the concentration of the reactant by:

$$r = k[C]^x \tag{6.2.3}$$

where $k$ is the rate constant, $[C]$ is the concentration and $x$ is the order of the reaction. Given the absorbance is related linearly to the concentration from equation 6.2.1, a standard first order (i.e. $x = 1$) rate equation for a simple reaction with two reactants is:

$\ln A_t = -kt + \ln A_0$ (6.2.4) where $k$ is the rate constant, $A_t$ is the absorbance at time $t$ and $A_0$ is the absorbance at time $t = 0$. In the case of hair dye, however, the reaction is not simply between two reactants but rather many, and thus the

reaction does not follow a standard first or second order rate equation. Equation 6.2.4 may be modified for hair dye [100] to give:

$$A = A_{\text{inf}}(1 - e^{-kt}) + d \tag{6.2.5}$$

where $A_{\text{inf}}$ is the absorbance of the dye at infinite time - that is, when it has completely reacted, and $d$ is the contribution from the dye.

It is therefore possible to loosely model the reaction by plotting the natural log of time vs absorbance for each wavelength, which should have an approximately linear relationship.

## 6.3 Chemistry of Hair Dye

The chemistry of hair dye is complicated, involving several chemicals to not only provide the correct colour but also manipulate the hair structure itself. Hair itself is made of several layers of keratin, as shown in Figure 6.2. Permanent hair dying oxidises melatonin in the hair cortex underneath the outer layer of the hair (the cuticle) in an irreversible chemical reaction removing its pigment. A secondary oxidation reaction then provides the colour. Peroxide is used for the oxidation as it decomposes into oxygen and water; the peroxide also removes sulphur from the hair.

Intermediates such as resorcinol and aminotoluenes provide the colour for hair dye; a wide spectrum of shades may be obtained through combinations of these intermediates along with aniline derived couplers, which are typically grouped into red, blue and yellow-green. Ammonia is required for an alkaline reaction environment, and to open the hair cuticle thus allowing the colour to penetrate, which allows for hair dying without pre-bleaching. Alcohols dry the hair out so its easier for the colour to stick to the hair, and conditioners are added to close the cuticle again after colouring [101].

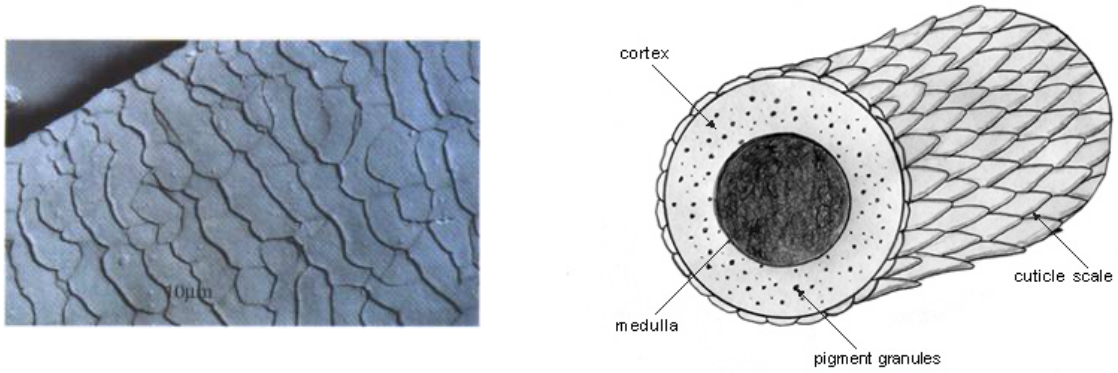


Figure 6.2: *(a) SEM image of a human hair showing the keratin layers of the cuticle (taken from [7]), (b) the structure of a human hair (taken from [8]), showing the cortex layer underneath the cuticle, which is the part of the hair responsible for its colour*

## 6.4 Confocal microscopy

In the case of thin microfluidic channels, equation 6.2.1 indicates that resulting small path length will give very small values of absorbance. To increase the signal to noise ratio, it is important to reduce the background signal in relation to the absorbance signal. The flow channels used in this experiment were thin-bottomed flow channels from Micronit microfluidics, with dimensions as shown in Figure 6.3. Conversely, in the hair dye monitoring system currently used by P&G, a specialised one-drop sample holder with a path length of 1 mm is used, which is about 20 times greater. We would therefore expect an approximately 20 times decrease in the absorbance values obtained in our system.

Adding to the reduced signal to noise in these channels, Figure 6.4 shows the projected image of the microfluidic channel when light is shone through it, and indicates the problems involved with using a focal spot much larger than the size of the channel. We can see that the channel edges make the image look darker as the light is scattered by the channel edges, and thus the scattered light will not reach the spectrometer. Therefore more light reaches the spectrometer with liquid present than without, hence the ratio $I/I_0$ is greater than 1. This leads to

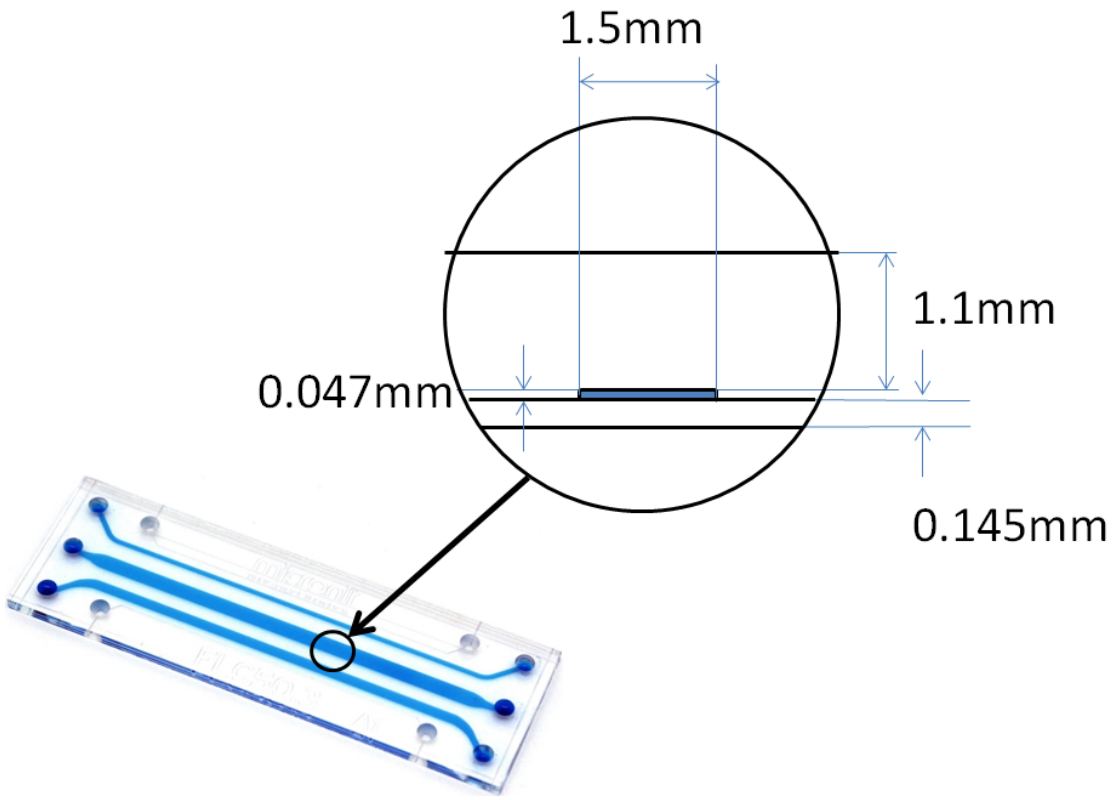


Figure 6.3: *Image adapted from Micronit microfluidics of the flow channel cross section (not to scale)*

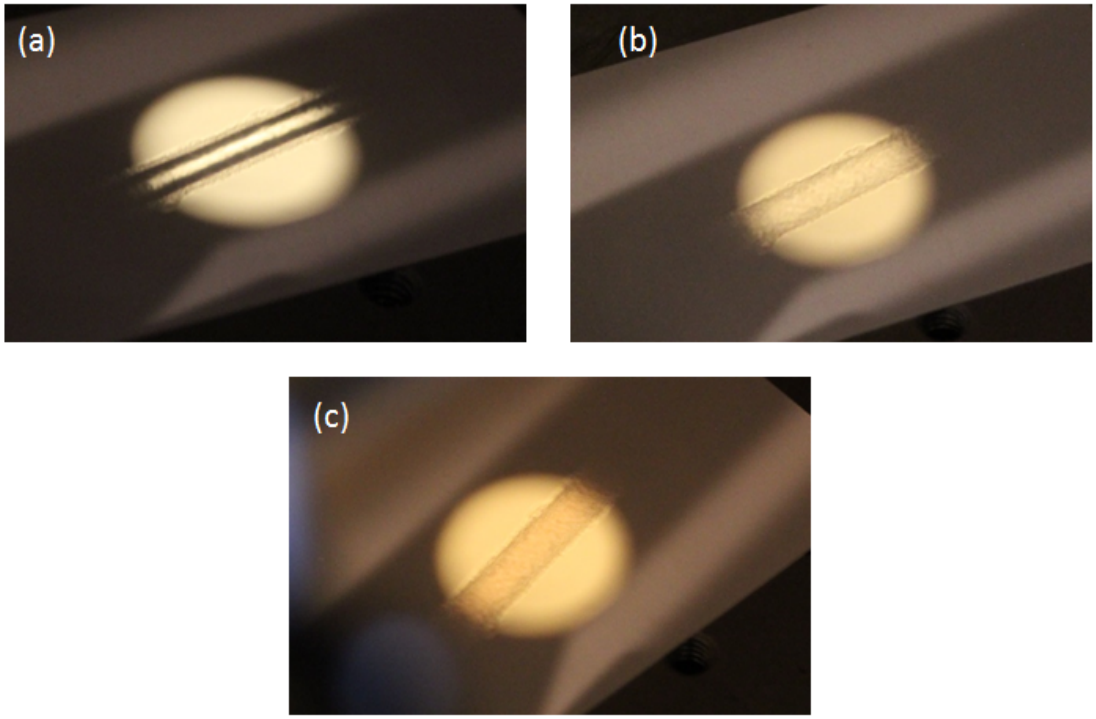


Figure 6.4: *Images showing the problem of non-matching refractive indices when taking spectra of microfluidic channels (a) an empty channel, (b) channel filled with water, (c) channel with Illumina 5/- dye after 10 minutes*

negative absorbance values if air is used as a reference.

It was decided therefore that the light passing through the channel should be restricted to a small active volume in the channel. The light from the LED was attenuated by a pinhole and focussed onto the sample by a microscope objective, and this was collected by a second microscope objective which re-imaged the light onto the spectrometer fibre. In this scenario, we may calculate the axial full width half maximum (FWHM) of the focussed spot to be [102]:

$$FWHM_{ax,pinhole} = \sqrt{\left(\frac{0.88\lambda}{n - \sqrt{n^2 - NA^2}}\right)^2 + \left(\frac{\sqrt{2}nPH}{NA}\right)^2} \tag{6.4.6}$$

where $PH$ is the pinhole diameter, $n$ is the medium refractive index and $NA$ is the microscope objective numerical aperture. Laterally, the diffraction limited FWHM for pinholes larger than one Airy unit is given by:

$$FWHM_{lateral} = \frac{0.51\lambda}{NA} \tag{6.4.7}$$

which for pinhole sizes under 1 mm will be far smaller than the width of the channel. It may be tempting to use a smaller pinhole to further reduce the illuminated volume of the channel, but problems may occur in this scenario, as shown in Figure 6.5 which shows some of the aberrations that may take place in absorbance spectroscopy undertaken in a microfluidic channel. Equation 6.4.6 describes the dependence of the axial spot size on the wavelength of the light; shorter wavelengths are focussed more strongly than longer wavelengths, and in this experiment it is necessary to use broadband light from 450 nm to 650 nm. Through making the system more confocal there is more of a dependence on the light wavelength and thus some light wavelengths are focussed onto the fibre at different axial distances, which is undesirable, thus giving incorrect absorbance results. There is also the problem of bubbles in the channel, which causes light to be improperly focussed onto the optical fibre due to refraction. This is very hard to control, and is compensated for through the use of a camera inserted into the transmission arm of the

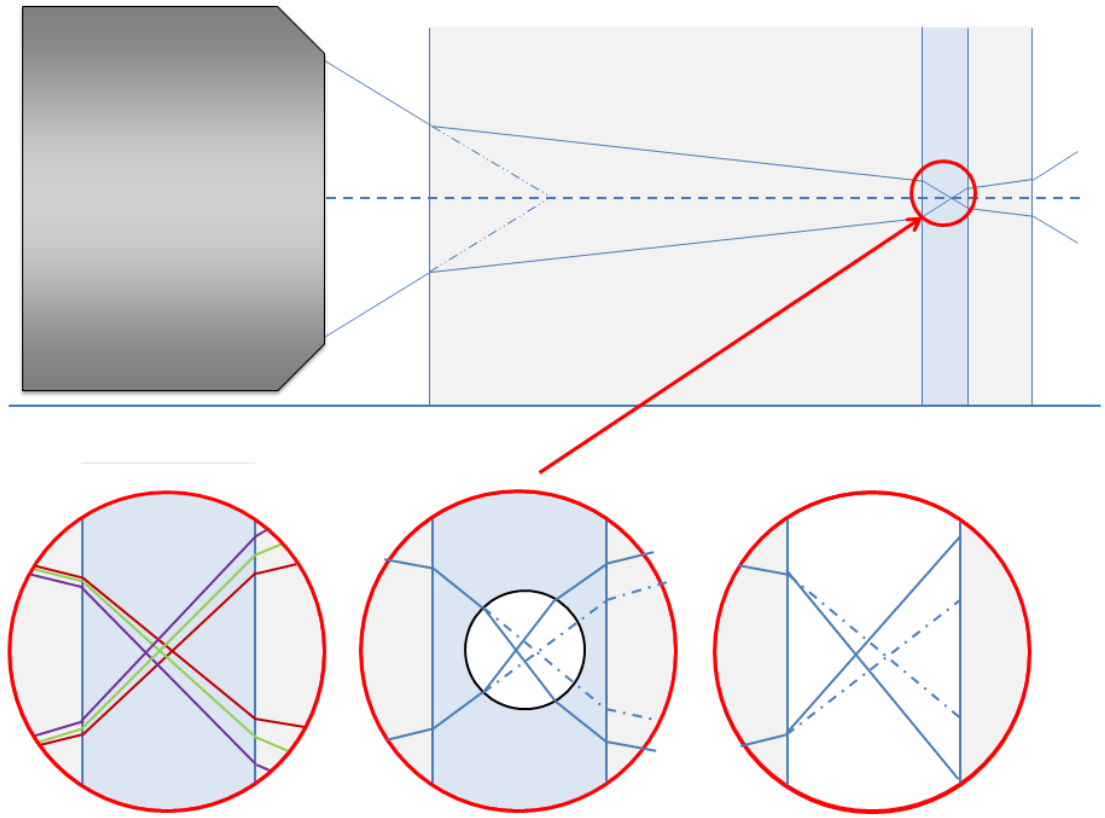

Figure 6.5: *An example (not to scale) of some of the possible aberrations encountered in the microfluidic channel, through the use of a) tightly focussed broadband light (chromatic aberration), b) the presence of bubbles (spherical aberration) or c) the presence of air (defocus)*

setup.

Additionally, there is the problem of the hair dye solution being non-uniform, and hence we wish to examine as large a volume of the liquid as possible to judge the solution as a whole. There is therefore a limit on the minimum pinhole size we can use.

## 6.5 Experimental setup and details

### 6.5.1 Simple replica setup

The hair dye samples were first investigated using a very simple setup as shown in Figure 6.6. This was designed to compare the performance of our LED and spectrometer to the results from P&G, who use a broadband light source as part of their commercial spectrophotometer system (Jasco V-650 UV-Visible spectrophotometer with one-drop SAH-769 accessory). This takes spectra over a period of 10 minutes, and takes 60 seconds to record each spectrum via measuring the transmitted light through the sample over a 400-700 nm spectral range. The hair dye itself is a viscous gel mixture which allows for easier application to hair (hereafter referred to as the gel 'chassis') and must first be diluted to increase its transparency and permit light to pass through the sample to be measured. This also allows for faster mixing with the peroxide-catalyst mixture. 150 ml of the chassis was diluted in 4000 $\mu$l water by carefully introducing and expelling the mixture in and out of a pipette for about 10 minutes to prevent bubble formation. 30% hydrogen peroxide was diluted to a 1:30 solution and 45% iron chloride diluted to 1:600, and these were mixed together in a 1:1 ratio to create 150 ml of peroxide-catalyst mixture [1]. This mixture was left for 30 seconds to allow some oxygen to develop, and this was then added to the diluted hair dye chassis mixture. The two were mixed together via swirling the container, and 20 ml of this solution was pipetted onto a microscope slide and a LabVIEW program used to take spectra over time. For each reading, 200 spectra were taken with an integration time of 5 milliseconds each and averaged, giving a total time of 1 second per reading. Dark and reference spectra were taken first, then one reading was taken every minute over a total of 10 minutes.

[1] It should be noted that the hydrogen peroxide is not usually catalysed by this much iron chloride in professional hair dying procedure; this simply reduces the time for the reaction to complete to 10 minutes for faster analysis

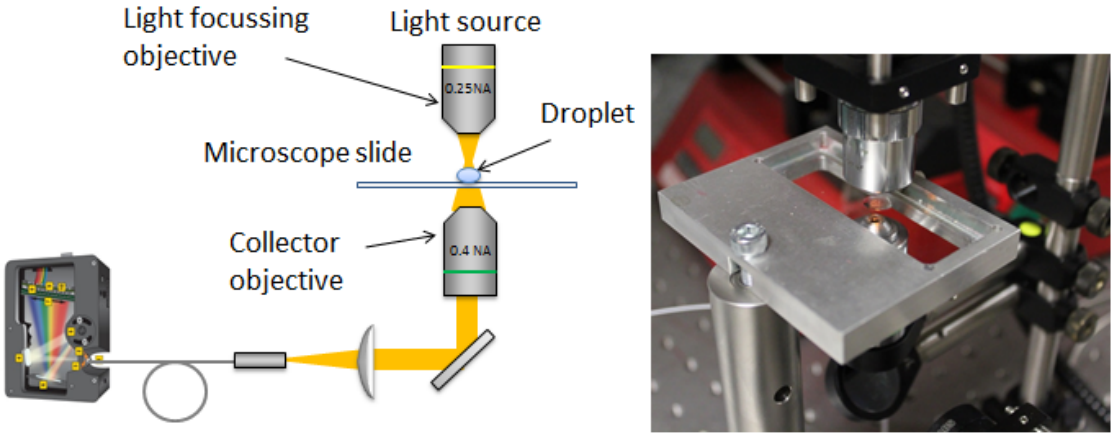


Figure 6.6: *Simple setup for investigating the absorbance spectrum of a 20 ml sample of hair dye. The alignment here is not critical as the idea is to focus the light onto the sample and collect light from a small area underneath*

### 6.5.2 Confocal setup

A second setup was used to investigate the reactions in a microfluidic channel, as shown in figures 6.7 and 6.8. Given that the illuminating objective has a magnification of 10×, a 200 $\mu$m diameter pinhole at the focus gives an image of the pinhole at the focal plane with a diameter of 20 $\mu$m. As the channel is 1500 $\mu$m across, this removes the effects from the image edges. The axial width of the resulting confocal volume is therefore approximately 1.5 mm which, while larger than the width of the channel, is greater than the distance which would cause chromatic aberration and allows us to examine a larger amount of fluid.

The mixture was made up in the same way as in the first setup, but instead of pipetting onto a slide, a small amount of the hair dye solution and catalyst was syringed out and introduced into the channel via PTFE tubing attached to the syringe via a Luer lock connector. It was found that the reaction itself generated a large number of bubbles from the production of oxygen, which caused aberrations in light path through the channel. Therefore, a channel with a width of 1500 $\mu$m was chosen to give as large a volume as possible to decrease the effects of the

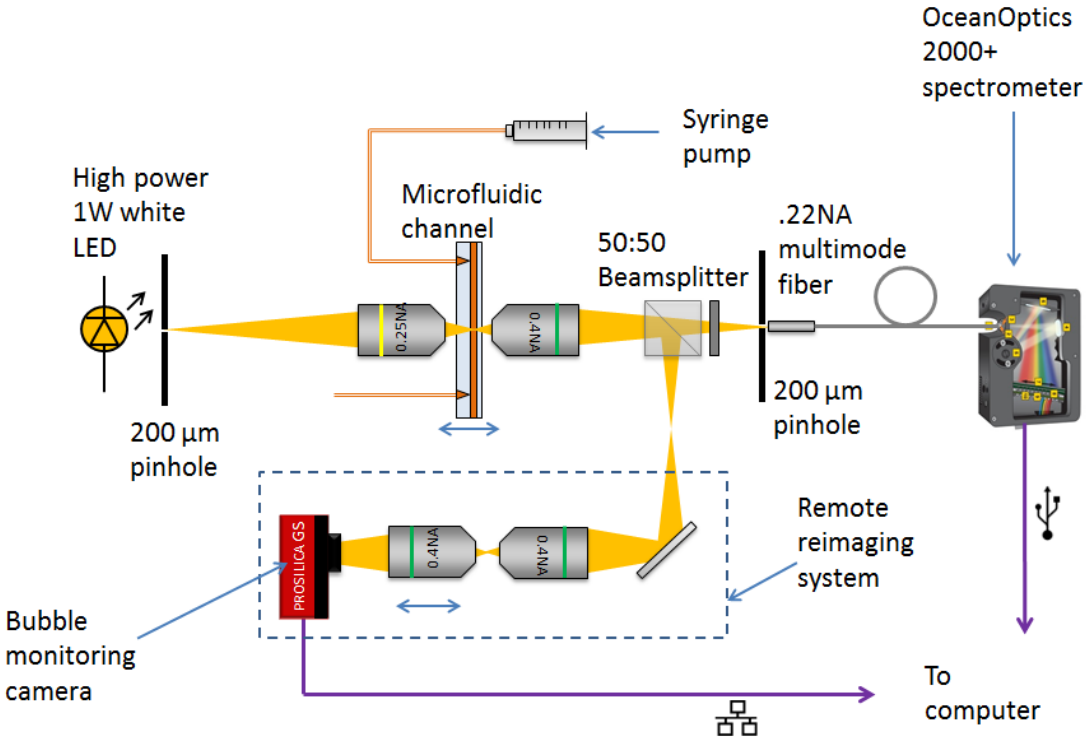


Figure 6.7: *Schematic of the experimental setup*

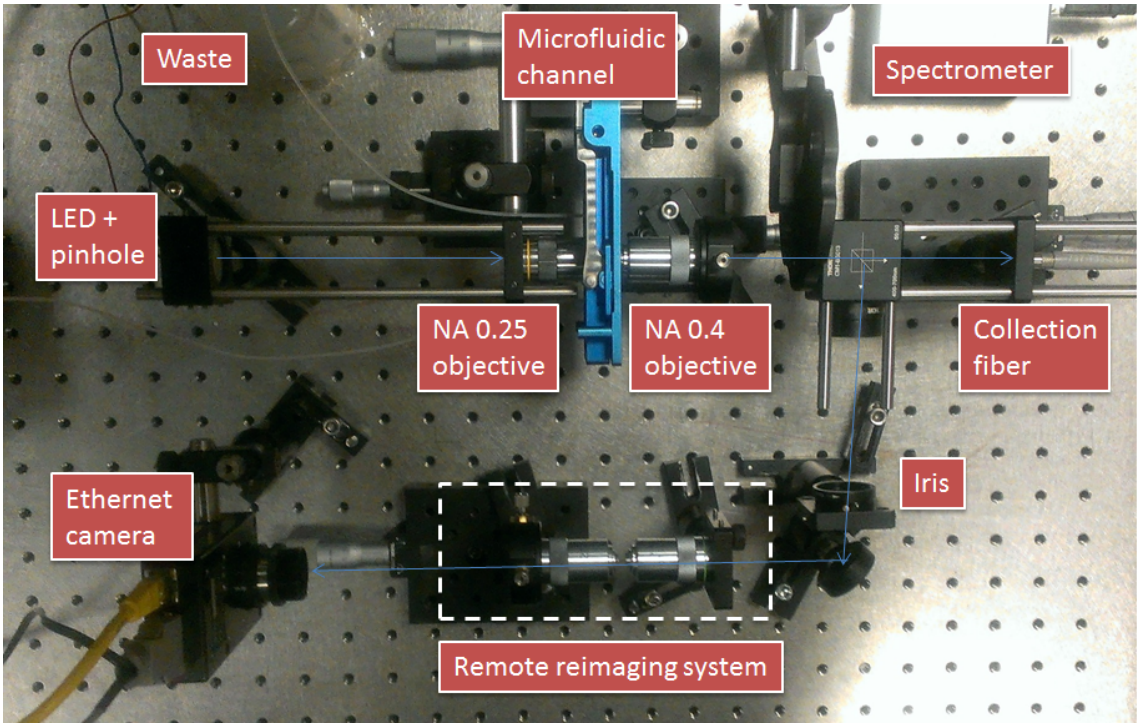


Figure 6.8: *Photograph of the experimental setup*

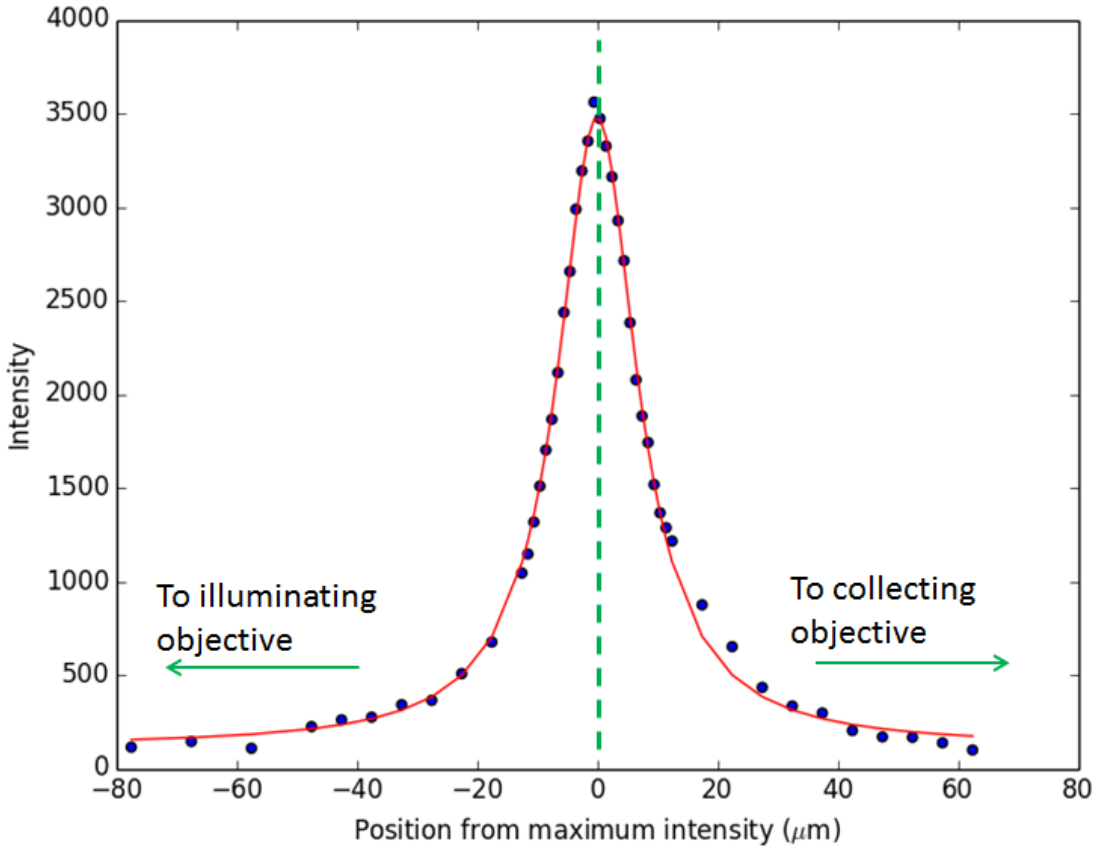


Figure 6.9: *A plot of the emission intensity of fluorescein when the white LED is replaced with a blue LED, against the position of the microfluidic channel in μm, and the corresponding fit in red, which was found to be a Lorentzian. The channel width may be determined from the full width half maximum of the fit.*

bubbles. The hair dye solution was then flown at a constant rate using a syringe pump set to flow the mixture through the channel at a rate of 0.1 ml/h. This was found to be the greatest possible pump speed that did not introduce more bubbles into the system.

To determine the optimum position of the microfluidic channel so the focus of the illuminating objective coincided with the position of the sample volume, an axial scan was taken by moving the stage and checking the light intensity of a fluorescing fluid inside the channel. The white LED was replaced with a 470 nm LED with a $(450 \pm 10)$ nm bandpass filter placed in front of the LED and a blocking filter added before the beamsplitter in the setup. 1 mM of fluorescein was

then introduced into the channel. The channel was moved axially on a micrometre stage and spectra taken at 1 $\mu$m intervals. The position was plotted against the maximum of the obtained emission spectrum as shown in Figure 6.9. We can see that there is a point at which the fluorescence is a maximum and this drops off at the sides. The depth of the channel is 47 $\mu$m, and we can see that the signal is only present in an approximately 47 $\mu$m axial range. We can also see that the spectrum drops off more slowly on one side than the other; given that the channel is axially antisymmetric we might expect this. Absorbance spectra were therefore taken with the channel at this position.

Spectra were taken at an integration time of 10 milliseconds with 500 spectra averaged per reading, giving a time of 5 seconds per reading, every minute for 10 minutes. A longer integration time was decided on due to the lowered light levels in the system from the addition of the pinhole and beamsplitter, and increased averaging was used in an attempt to increase the signal-to-noise ratio. Dark and reference spectra were taken with deionised water in the channel as the reference.

### 6.5.3 Bubble rejection procedures

Hair dye development is a process which intrinsically produces bubbles. These bubbles, while not a problem for large volumes, present a problem in a microfluidic channel, where a 1mm diameter bubble in our microfluidic channel takes up a length of several centimetres! As removing the bubbles entirely would hinder the development of the dye, it was decided that a camera should be placed in the setup to monitor the bubbles.

#### Remote reimaging

Good images are necessary to define robust rejection criteria of images, and hence spectra, taken by the camera, which is discussed further in the next section. We need to be able to distinguish between edges of bubbles, the non-uniform solutions and large bubbles that take up the entire volume being analysed. It was found that when a detector was simply placed in the transmission arm of the experiment

after a beamsplitter, images were poor. This is due to the fact that, while the centre of the channel may be the best volume from which to obtain spectra, it is not necessarily the best area for a good image. This is due to aberrations caused by the non-uniformity of the fluid. It might be tempting to move the camera to a different imaging plane, but this both gives rise to spherical aberration and is much dimmer. Given that both the illumination and transmission objectives must remain stationary to obtain spectra, it was decided that instead the focal plane would be reimaged remotely [103]. This is a technique generally used in high numerical aperture microscopy when the imaging objective either cannot be moved or where movement would cause significant specimen disturbance.

The system is as follows; a second objective is placed in the rear focal plane of the transmission objective, with the same numerical aperture. This creates a perfect image of the focussed spot; however, a third objective is required to magnify this due to the resolution of the detector. The third objective also serves to select the plane required for imaging. The detector is then placed in the plane of the correct, unaberrated image. A pinhole is also used at the rear focus of the second objective to block out extra light from brighter planes.

### Rejection criteria

An Ethernet camera was programmed to take an image for every spectroscopic reading. After the readings were taken, the contrast was enhanced Figure 6.10 shows some examples of the camera images There are also some errors due to inadequately mixed solution. The solution is in effect an emulsion; the hair dye is held in a gel 'chassis', and so must be diluted before use. Insufficient mixing results in large lumps of the gel chassis in the mixture.

Figure 6.11 shows the criteria used for determining whether a spectral reading is compromised by either bubbles or poor mixing. Each image is cropped so only the image of the channel is analysed, and a histogram is made from the pixel values in each image. Small bubbles or large clumps may be detected as a spike at low

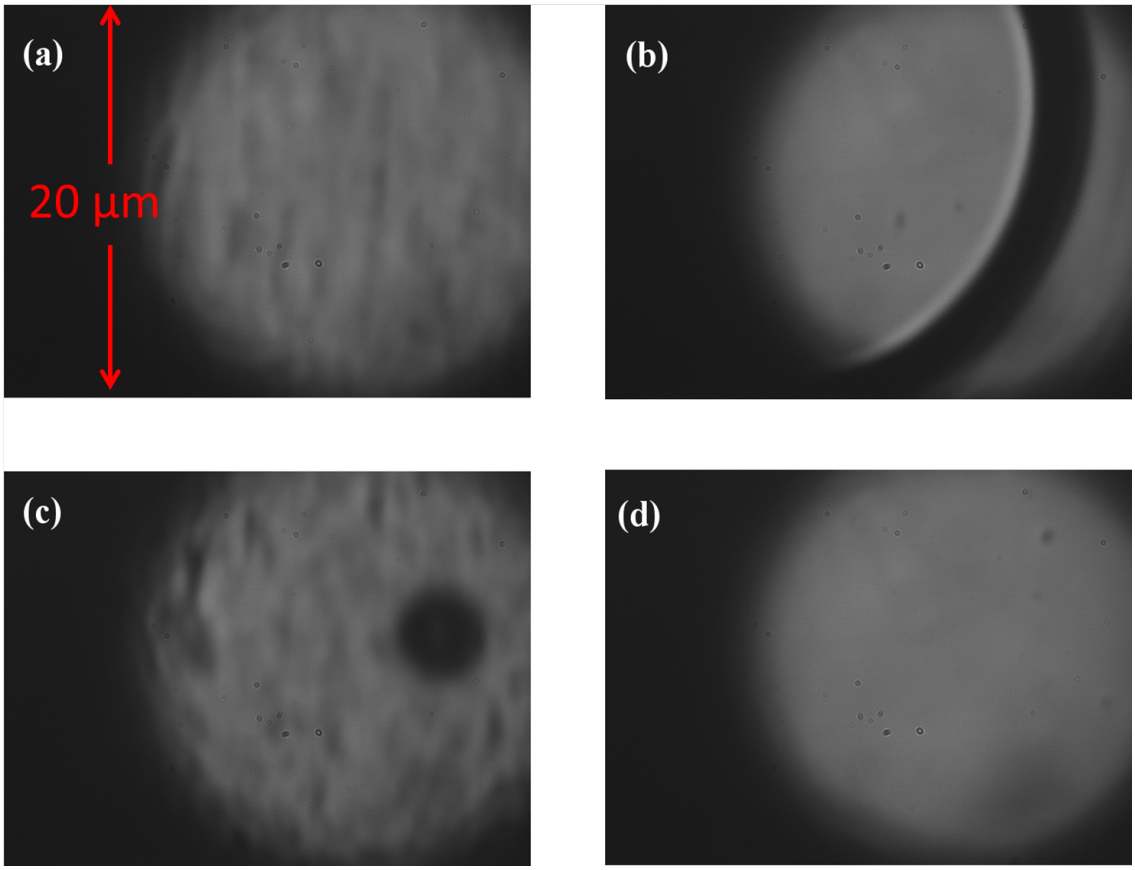


Figure 6.10: *Images depicting examples of the possible camera images we can obtain. In (a), we have an ideal image. In (b), there is a bubble flowing through the channel and thus our obtained spectrum will be suboptimal. In (c) the chassis has not been mixed thoroughly enough and a blob of chassis is flowing past. In (d) the bubble flowing past is so large that we can't see the edges*

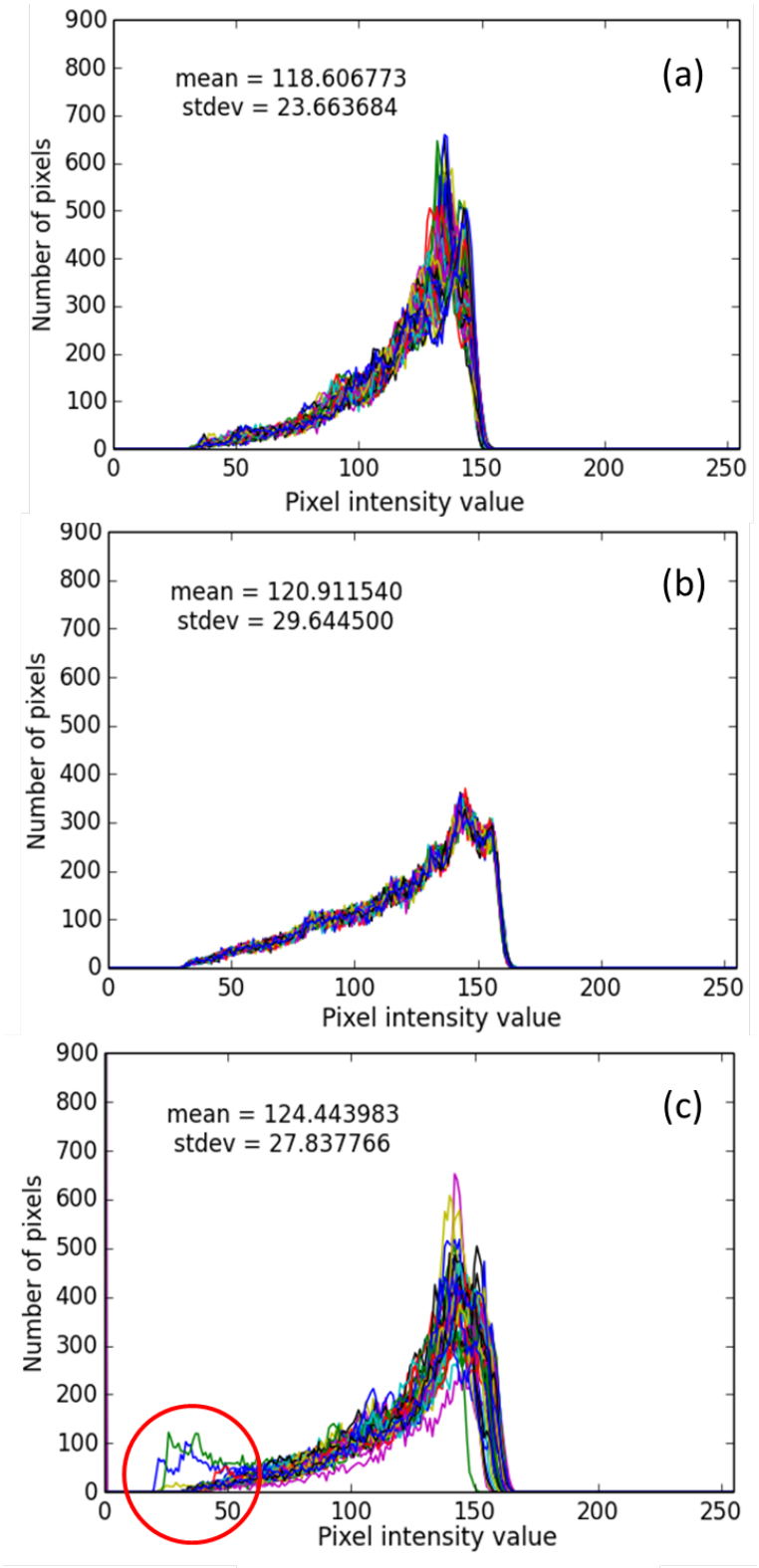


Figure 6.11: *Figures showing pixel intensity (0-255) values against number of pixels, each corresponding to an example 5 second averaged spectrometer reading. 50 histograms are plotted for the 50 images taken by the camera in the 5 seconds, corresponding to 10 averaged spectrometer spectra. a) is an example of a good reading, b) is the typical histogram of imaging inside a bubble, and c) is the obtained spectrum when a small bubble is present (the spike at the low RGB values indicates a dark bubble edge being detected)*

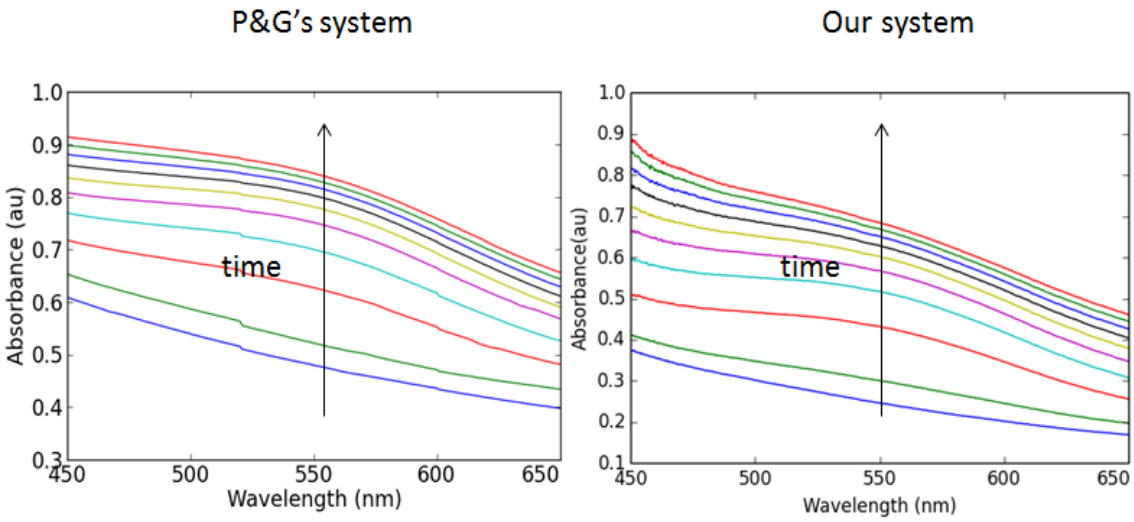


Figure 6.12: *Absorbance spectra over a 9 minute period (with readings at one minute intervals) for a sample of blonde hair dye (Wella Illumina 9/-)*

intensity values as there are more dark pixels (as shown in Figure 6.11(c). Thus, a limit to the number of pixels with an intensity value lower than, say 50, is set as a threshold for rejecting images, and therefore readings. Larger bubbles which fill the channel, however, may not be detected this way; Figure 6.11(b), which was obtained for air in the channel, looks very similar to that of a good reading, as shown in Figure 6.11(a).

We may further distinguish between good and poor readings via analysis of the standard deviation of all pixels in an image. It can be seen that in all the histograms there is a peak number of pixels at an intensity value of around 150, and this peak is, in general, higher for good images, due to the non-uniform nature of the diluted hair dye. This leads to a lower standard deviation in the intensity values for good readings, and thus we may set a maximum threshold for image rejection, which in this case was set to 28, thus leading to rejection of the reading corresponding to histogram (b) in Figure 6.11, with a standard deviation of 29.6.

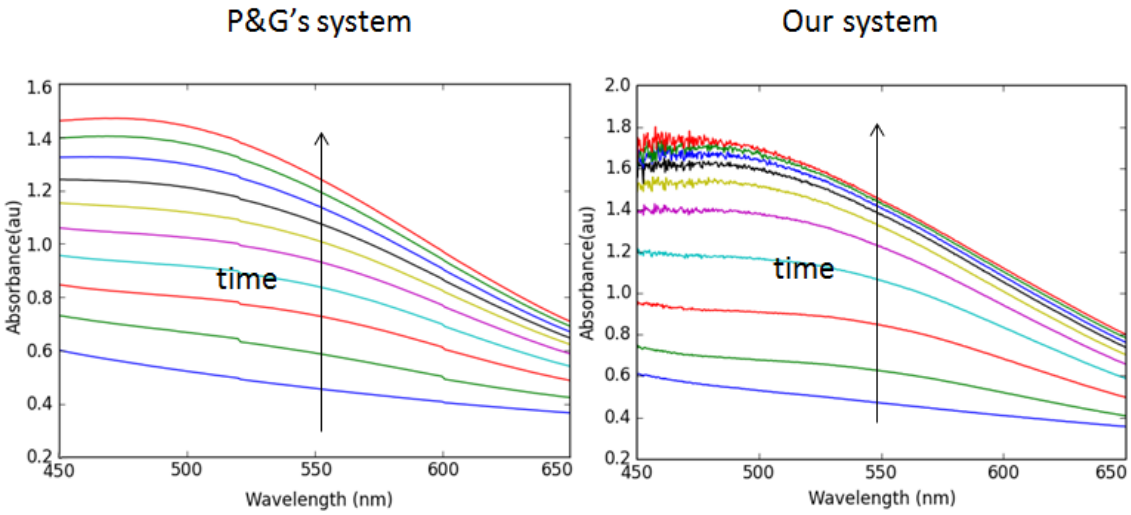


Figure 6.13: *Absorbance spectra over a 9 minute period (with readings at one minute intervals) for a sample of brown hair dye (Wella Illumina 5/-)*

## 6.6 Results and Discussions

### 6.6.1 Rate constant calculation for the P&G 'replica' setup

Figures 6.12 and 6.13 show the results obtained by Proctor and Gamble's in house spectrophotometer compared to our simple spectrometer system for one drop of activated hair dye solution. We can see that the blonde and brown spectra absorb more strongly in the blue than in the red, which we would expect from the varying shades of brown found in hair dye. The brown hair dye also absorbs more strongly overall than the blonde shade, which again is what we might expect. Our results are slightly different to those of P&G's, which we might expect due to the different light sources used; P&G use a tungsten light source whereas we use an LED, the typical spectrum of which is shown in Figure 6.14.

A white light LED produces white light via photoluminescence; a thin phosphorus layer is applied on top of a blue LED, and the blue light excites this layer producing yellow light. A white light LED spectrum is therefore a mixture of narrowband blue light and wider band yellow light, which we see as white light; however this is not broadband light as there is a distinctive 'dip' at around 500

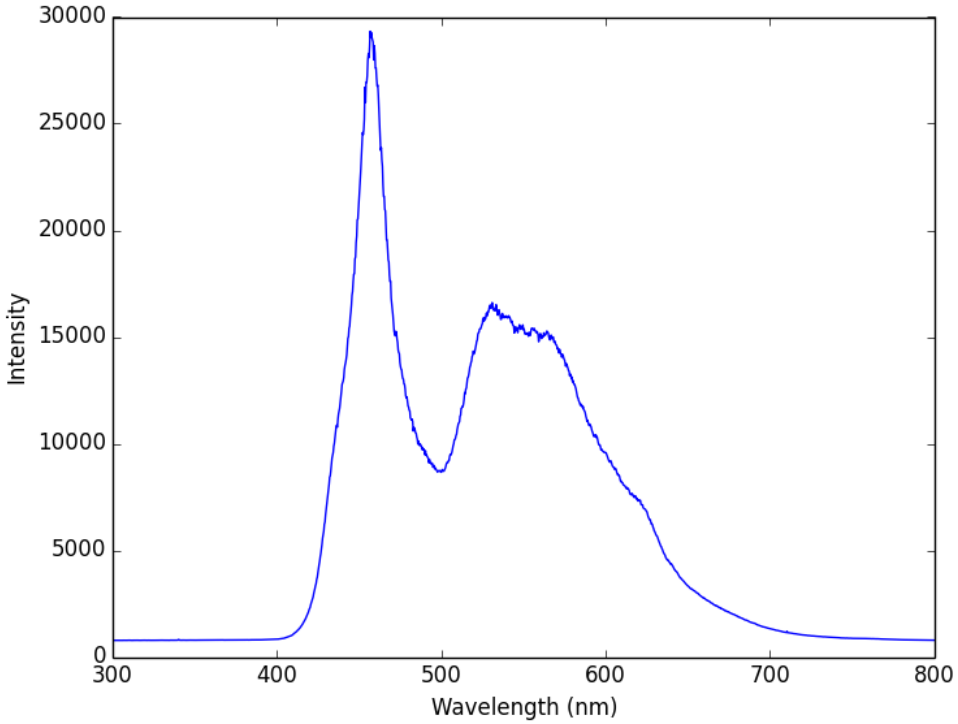


Figure 6.14: *Typical spectrum of the white light LED used in this experiment*

nm in the spectrum.

The rate constants for the reaction were calculated using the method in equation 6.2.4 and are shown plotted against wavelength in Figure 6.15 for both the P&G system and our system. Comparing our results to the standard obtained by P&G, the plots show more agreement at longer wavelengths, most likely due to the light source used. The difference in results is also likely to be due to the path length not being regulated in the replica system; the one drop spectrometer has a defined path length whereas we pipette a drop onto a sample plate. Therefore, in this case we can say that our system models the P&G system reasonably well at longer wavelengths given the differences in instrumentation. Given that we will be using a substantially smaller but constant path length in the microfluidic system, along with a different reference (air), it is likely that new standards will need to be defined.

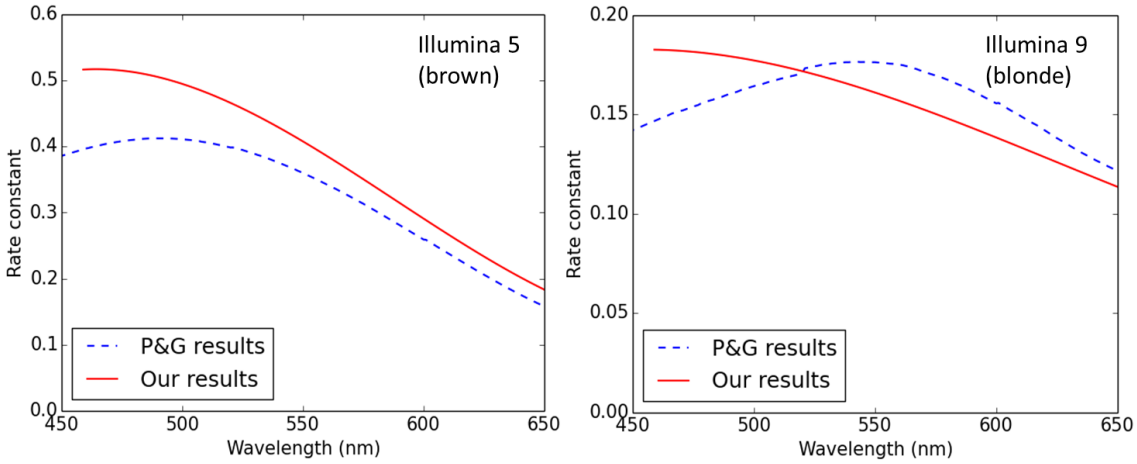


Figure 6.15: *Rate constants for brown hair dye (left) and blonde hair dye (right). The red lines indicate the obtained results by our setup; the blue lines indicate P&G's results*

### 6.6.2 Rate constant calculation in the microfluidic channel

Figure 6.16 shows two separate absorbance measurements taken over time with the confocal setup. From this it is clear that the bubbles present a major issue in obtaining results. While occasionally we may get good results, as shown on the right in Figure 6.16, if a bubble is present in a reading we get incorrect results, which are clearly visible as not having the correct absorbance values over the wavelength range; these are rejected by the bubble rejection program, which can also tell us if a reading has been partly obscured by bubbles or poor mixing. It was found that bubbles were a much more serious issue in blonde dye shades than in darker shades, which is most likely a side effect due to the differing chemistry of the reaction.

It is necessary to define a new standard for the relationship between rate constant and wavelength, as the rate constant will have changed both due to using water as a reference (whereas P&G use air as a reference) and from decreasing the path length significantly. Figure 6.17 is plot of the relationship between absorbance and log time for a single reading at both 450 nm and 650 nm, for a brown shade with no bubbles present in the system. We can see that the absorbance at each wavelength follows an approximately linear relationship in relation to log

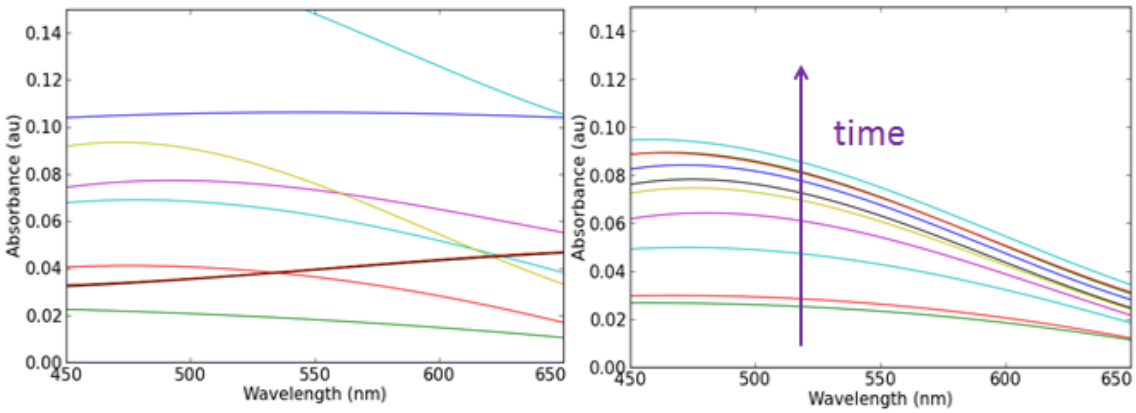


Figure 6.16: *An example of a) Poor absorbance-wavelength plots obtained over time due to bubbles, b) A better example of the absorbance-wavelength relation over time showing the overall increase in absorbance. Results have been smoothed for clarity*

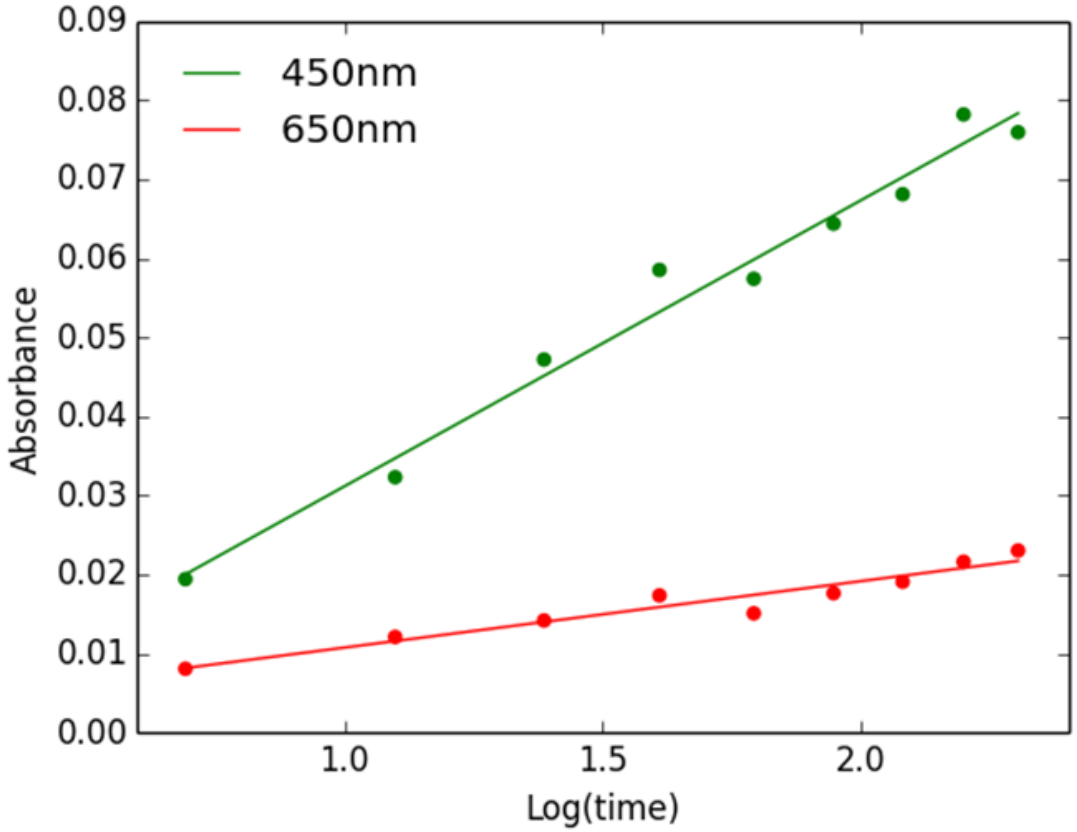


Figure 6.17: *Plot of absorbance vs log time for a sample of brown hair dye (without bubbles) and the corresponding fits*

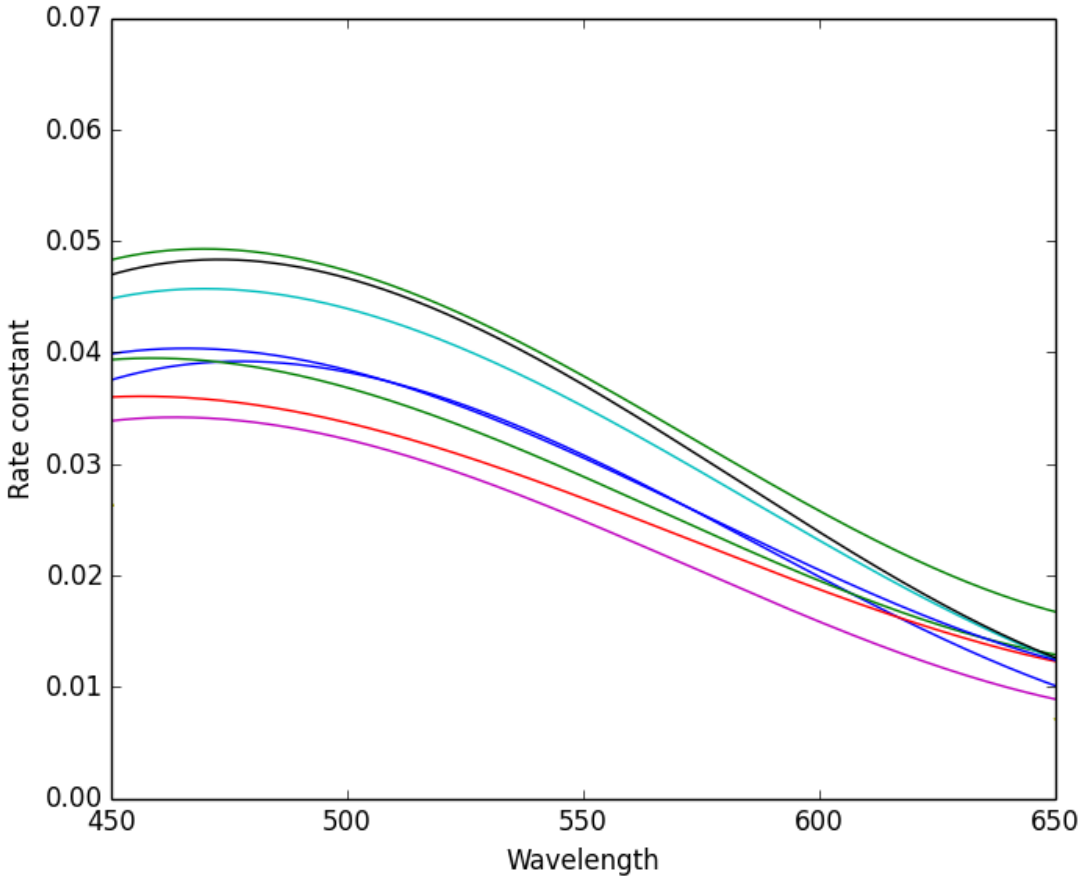


Figure 6.18: *Rate constant plotted against wavelength for 8 samples of the same brown hair dye shade*

time, as before. Through least squares fitting, the slopes of the lines were calculated for each wavelength, which were the rate constants. We would expect to still obtain a straight line relationship with our current setup, as before, as the only thing which has changed is the reference medium, which retains the same light absorbance properties over time. The slope of the line of best fit (the rate constant) against wavelength for all wavelengths was then plotted for 8 samples of the same hair dye shade, and the relation shown in Figure 6.18 was obtained.

Figure 6.18 shows the rate constants obtained for a range of readings from the same tube of brown hair dye. These plots show a basic resemblance to that of Figure 6.15 and have the same basic shape, showing that using water as a reference does not cause significant changes to the shape of the rate constant-wavelength

relation. However, there is still some variation in the results. This is most likely due to lowered signal to noise, and also possibly to human error in the mixing, which is much more of a problem at small scales. However, it is reasonable to conclude that with increased signal to noise, possibly through the use of a wider channel, the technique could be much improved as the absorbance values would be much larger due to a larger path length.

## 6.7 Future work

The main issues with the current system are the low signal to noise and the production of bubbles. This could be improved substantially through the use of channels with a larger path length; giving larger absorbance values over the wavelength range and increasing the total channel volume in relation to the size of the bubbles; alternatively rectangular capillaries could be used. This conversely would require more compound to be used. Another method other than syringe pumps, which were available at the time, could also contribute to reducing the bubble formation through syringe pump micro-oscillations. Finally, chemical methods such as reducing the amount of peroxide-catalyst added to the solution could be used to chemically reduce the amount of bubbles formed, though this would also reduce the rate of the reaction. The system could also be improved in the 500 nm region through the use of an extra blue/green LED in the system.

The imaging system itself is designed to be part of a larger system, in which dyes are mixed from scratch from several components and mixed with the developer in situ. This allows for greater automation of the hair dye testing process, reducing user input and errors, and uses smaller sample volumes thus reducing waste. This would be achieved through the use of gas pressure driven pumping (using an inert gas) to flow a combination of several different hair dye components through the system. These would be mixed before a valve, possibly using a microfluidic mixer channel to mix the components. This would then be mixed with the catalyst-peroxide mixture, the flow of which would be controlled by a second

valve, and the combined mixture would be flown through the absorbance spectroscopy analysis channel. By varying the flow rate of the solution, it may even be possible to reduce the time necessary to take measurements, as measurements could be taken at several points along the channel.

# Chapter 7

# Conclusions

Optical methods naturally lend themselves to the investigation of high volume consumer products, due to their speed and non-invasive nature. In this thesis, Raman optical tweezing has been implemented to investigate the reactions in a dishwasher, while optical spectroscopy was used to investigate both clothes detergents and hair dye; microfluidic channels and 96 well plates providing the platforms on which to undertake the reactions.

Raman tweezing has previously shown its usefulness as a tool for the analysis of microscopic objects. However, processes in a dishwasher are complex. It has been shown that while the reactions which take place can be modelled in a microfluidic environment, analysis is made more complicated through the unforeseen effects of these reactions on trapping and analysis, such as trap instability, small analyte volumes and obscuring of the samples. Similarly, the chemical reactions involved in the colour development of hair dye cause the formation of air bubbles, which are a nuisance. However, it is possible to compensate for some of these flaws, for example through the use of a camera to monitor the air bubbles in hair dye solution, or through predicting the effects that flow may have on optically trapped species.

The possibility of alternative tracking methods or experimental background subtraction methods have been discussed, showing how they could be used to improve

the miniature dishwasher analysis tool. There is also the possibility of approaching the problem from a different angle, which has been touched upon. For example, hyperspectral analysis of the channel surface proved to be a powerful tool for detection of crystals. While cost and time could be issues, it is possible that this could be carried out on any microfluidic surface thin enough to allow for high resolution spectral imaging, for example glass, PMMA or polystyrene. Another promising technique which has very recently [104] been developed at Oxford University has involved the use of remote reimaging to allow for confocal analysis of trapped particles. This involves the reimaging of the focal plane at a distance, allowing for the trapping objective to remain stationary, preventing any disturbance of the trapping laser. This could prove very useful for detecting crystallisation on the surface of trapped species, and further development of this technique to increase the speed at which microscope objectives can be moved could lead to higher time resolutions for which 3D images can be acquired.

This technique was, however, partly implemented to image bubbles in hair dye while simultaneously taking absorbance spectra of the solution to monitor its colour. Microfluidic monitoring of hair dye has potential as a technique, and with the use of longer path length channels and lower concentrations of the developer chemicals, the problems created by the bubbles could be almost completely eliminated, making this a suitable technique to integrate into a constant chemical flow environment. The miniature stain analysis spectrometer for fabrics also has potential; with more time more stains could be analysed and a library built up of many transmission and reflection spectra for stain and detergent combinations; this will also lead to improved principal components. It was found that the principal components highlighted the important aspects of stains that lead to the quantification of their effects on fabrics (their greasiness and their colour). With further work, this could be used to analyse the effects of detergents on both greasiness and colour simultaneously, and hence deduce if detergents are better for removing grease or colours.

Optical techniques are thus promising tools for analysing and advancing the chemical reactions which dominate our daily lives, and may thus play an important part in the development of products used in homes in the future.

# Bibliography


[1] Hamamatsu website. http://www.hamamatsu.com/eu/en/technology/innovation/lcos-slm/index.html. Accessed: 12-12-2014.

[2] A.L. Jenkins and R.A. Larsen. Gemstone Identification Using Raman Spectroscopy. *Spectroscopy*, 19(4):20–25, 2004.

[3] A.C. De Luca. *Phase-sensitive detection in Raman Tweezers: biological applications*. PhD thesis, Universitá Di Napoli Federico II, 2007.

[4] J.M. Watkins, L.C. Nielsen, F.J. Ryerson, and D.J. DePaolo. The influence of kinetics on the oxygen isotope composition of calcium carbonate. *Earth and Planetary Science Letters*, 375:349–360, 2013.

[5] M. Holcomb, A.L. Cohen, R.I. Gabitov, and J.L. Hutter. Compositional and morphological features of aragonite precipitated experimentally from seawater and biogenically by corals. *Geochimica et Cosmochimica Acta*, 73:4166–4179, 2009.

[6] Q. Hu, J. Zhang, H. Teng, and U. Becker. Growth process and crystallographic properties of ammonia-induced vaterite. *American Mineralogist*, 97:1437–1445, 2012.

[7] P&G Beauty and Grooming: Hair Structure. http://pgbeautyscience.com/hair-structure.php. Accessed: 03-01-2015.

[8] Using Hair for Identification. http://www.ecobyte.com.au/using.html. Accessed: 03-01-2015.

[9] Department of Energy and Climate Change. *Energy Efficiency Statistical Summary*. 2012.

[10] R. Stamminger. *Synergy Potential of Smart Appliances*. 2008. Technical Report.

[11] C.P. Richter. Usage of dishwashers: observation of consumer habits in the domestic environment. *International Journal of Consumer Studies*, 35:180–186, 2011.

[12] F.R. Spellman. *Handbook of Water and Wastewater Treatment Plant Operations, Second Edition*. CRC Press, 2008.

[13] J.W.Gibbs. On the equilibrium of heterogeneous substances. Part II. *Transactions of the Connecticut Academy of Arts and Sciences*, 3:343–524, 1878.

[14] A. Ashkin. Acceleration and trapping of particles by radiation pressure. *Physical Review Letters*, 24(4):156–159, 1970.

[15] A. Ashkin. Forces of a single-beam gradient laser trap on a dielectric sphere in the ray optics regime. *Biophysical Journal*, 61(2):569–582, 1992.

[16] T.A. Nieminen, G. Knöner, N.R. Heckenberg, and H. Rubinsztein-Dunlop. Physics of optical tweezers. *Methods In Cell Biology*, 82(06):207–236, 2007.

[17] R.K. Montange, M.S. Bull, E.R. Shanblatt, and T.T. Perkins. Optimizing bead size reduces errors in force measurements in optical traps. *Optics Express*, 21(1):39–48, 2013.

[18] K.T. Gahagan and G.A. Swartzlander. Trapping of low-index microparticles in an optical vortex. *Journal of the Optical Society of America B*, 15(2):524–534, 1998.

[19] M.D. Wang, H. Yin, R. Landick, J. Gelles, and S.M. Block. Stretching DNA with optical tweezers. *Biophysical Journal*, 72(3):1335–1346, 1997.

[20] K. Svoboda and S.M. Block. Force and Velocity Measured for Single Kinesin Molecules. *Cell*, 77:773–784, 1994.

[21] W.M. Lee, P.J. Reece, R.F. Marchington, N.K. Metzger, and K. Dholakia. Construction and calibration of an optical trap on a fluorescence optical microscope. *Nature Protocols*, 2:3226–3238, 2007.

[22] H. Tang, H. Yao, G. Wang, Y. Wang, Y.Q. Li, and M. Feng. NIR Raman spectroscopic investigation of single mitochondria trapped by optical tweezers. *Optics Express*, 15(20):12708–12716, 2007.

[23] P. Jordan, J. Cooper, G. McNay, F.T. Docherty, D. Graham, W.E. Smith, G. Sinclair, and M.J. Padgett. Surface-enhanced resonance Raman scattering in optical tweezers using co-axial second harmonic generation. *Optics Express*, 13(11):4148–4153, 2005.

[24] E.R. Dufresne and D.G. Grier. Optical tweezer arrays and optical substrates created with diffractive optics. *Review of Scientific Instruments*, 69(5):1974–1977, 1998.

[25] S.D. Coomber, C.D. Cameron, J.R. Hughes, D.T. Sheerin, C.W. Slinger, M.A. Smith, and M. Stanley. Optically addressed spatial light modulators for replaying computer-generated holograms. In *Proc. SPIE*, volume 4457, pages 9–19, 2001.

[26] P. Madec. Overview of deformable mirror technologies for adaptive optics and astronomy. In *Proc. SPIE*, volume 8447, pages 844705–844705, 2012.

[27] C. Radzewicz, P. Wasylczyk, W. Wasilewski, and J.S. Krasiski. Piezo-driven deformable mirror for femtosecond pulse shaping. *Optics Letters*, 29(2):177–179, 2004.

[28] Forth Dimension Displays introduces QXGA-R9-AUX. http://optics.org/products/P000020407. Accessed: 12-12-2014.

[29] J. Leach, K. Wulff, G. Sinclair, P. Jordan, J. Courtial, L. Thomson, G. Gibson, K. Karunwi, J. Cooper, Z.J. Laczik, and M. Padgett. Interactive approach to optical tweezers control. *Applied Optics*, 45(5):897–903, 2006.

[30] G.M. Gibson, R.W. Bowman, A. Linnenberger, M. Dienerowitz, D.B. Phillips, D.M. Carberry, M.J. Miles, and M.J. Padgett. A compact holographic optical tweezers instrument. *Review of Scientific Instruments*, 83:113107, 2012.

[31] N.B. Simpson, L. Allen, and M.J. Padgett. Optical tweezers and optical spanners with Laguerre-Gaussian modes. *Journal of Modern Optics*, 43:2485–2491, 1996.

[32] R. Dasgupta, S. Ahlawat, R.S. Verma, and P.K. Gupta. Optical orientation and rotation of trapped red blood cells with Laguerre-Gaussian mode. *Optical Society of America*, 19(8):7680–7688, 2011.

[33] R. Brown. A brief account of microscopical observations made on the particles contained in the pollen of plants. *Edinburgh New Philosophical Journal*, 5:358–371, 1828.

[34] A. Einstein. Über die von der molekularkinetischen Theorie der Wärme geforderte Bewegung von in ruhenden Flüssigkeiten suspendierten Teilchen. *Annalen der Physik*, 17(8):549–560, 1905.

[35] C.D. Saunter, G.D. Love, M. Johns, and J. Holmes. FPGA technology for high-speed low-cost adaptive optics. *Proc SPIE*, 6018:429–435, 2005.

[36] K. Berg-Sörensen and H. Flyvbjerg. Power spectrum analysis for optical tweezers. *Review of Scientific Instruments*, 75(3):594, 2004.

[37] R.M. Simmons, J.T. Finer, S. Chu, and J.A. Spudich. Quantitative Measurements of Force and Displacement Using an Optical Trap. *Biophysical Journal*, 70:1813–1822, 1996.

[38] I. Tinoco, P.T.X. Li, and C. Bustamante. Determination of thermodynamics and kinetics of RNA reactions by force. *Quarterly Reviews of Biophysics*, 39(4):325–360, 2006.

[39] A. Smekal. Zur Quanthentheorie der Dispersion. *Naturwissenschaften*, 43:873–875, 1923.

[40] D.A. Long. *The Raman Effect: A Unified Treatment of the Theory of Raman Scattering by Molecules*. John Wiley and Sons, 2002.

[41] W. Demtröder. *Laser Spectroscopy: Basic Concepts and Instrumentation*. Springer Science and Business Media, 2003.

[42] H.N. Rutt and J.H. Nicola. Raman spectra of carbonates of calcite structure. *Journal of Physics C*, 7:4522–4528, 1974.

[43] S. Gunasekaran, G. Anbalagan, and S. Pandi. Raman and infrared spectra of carbonates of calcite structure. *Journal of Raman Spectroscopy*, 382:163–169, 2006.

[44] N. Buzgar and A.I. Apopei. The Raman Study of Certain Carbonates. *Analele Ştiintifice Ale Universităţii "Al. I. Cuza" Iaşi Geologie*, 55:97–112, 2009.

[45] J.C. Carls, G. Moncivais, and J.R. Brock. Time-resolved Raman spectroscopy from reacting optically levitated microdroplets. *Applied Optics*, 29(19):2913–2918, 1990.

[46] J.W. Chan. Recent advances in laser tweezers Raman spectroscopy (LTRS) for label-free analysis of single cells. *Journal of Biophotonics*, 6(1):36–44, 2013.

[47] A. Bankapur, E. Zachariah, S. Chidangil, M. Valiathan, and D. Mathurmail. Raman Tweezers Spectroscopy of Live, Single Red and White Blood Cells. *PLoS ONE*, 5(4):e10427, 2010.

[48] R.D. Snook, T.J. Harvey, E. Correia Faria, and P. Gardner. Raman tweezers and their application to the study of singly trapped eukaryotic cells. *Integrative Biology*, 1(1):43–52, 2009.

[49] C. Xie, J. Mace, M.A. Dinno, Y.Q. Li, W. Tang, R.J. Newton, and P.J. Gemperline. Identification of Single Bacterial Cells in Aqueous Solution Using Confocal Laser Tweezers Raman Spectroscopy. *Analytical Chemistry*, 77:4390–4397, 2005.

[50] E. Urlaub, M. Lankers, I. Hartmann, J. Popp, M. Trunk, and W. Kiefer. Raman investigation of styrene polymerization in single optically trapped emulsion particles. *Chemical Physics Letters*, 231(4-6):511–514, 1994.

[51] M. Trunk, J. Popp, I. Hartmann, M. Lankers, Urlaub E., and W. Kiefer. Chemical composition and reaction analysis of single aerosol particles. *Fresenius Journal of Analytical Chemistry*, 355:354–356, 1996.

[52] J. Chen and L. Xiang. Controllable synthesis of calcium carbonate polymorphs at different temperatures. *Journal of Powder Technology*, 189:64–69, 2009.

[53] L. Brečević and D. Kralj. On Calcium Carbonates: from Fundamental Research to Application. *Croatica Chemica Acta*, 80:467–484, 2007.

[54] K. Sawada. The mechanisms of crystallization and transformation of calcium carbonates. *Pure and Applied Chemistry*, 69(5):921–928, 1997.

[55] G. Stokes. On the Effect of the Internal Friction of Fluids on the Motion of Pendulums. *Transactions of the Cambridge Philosophical Society*, 9:8–106, 1851.

[56] O. Reynolds. An experimental investigation of the circumstances which determine whether the motion of water shall be direct or sinuous, and of the law of resistance in parallel channels. *Philosophical Transactions of the Royal Society*, 174:935–982, 1883.

[57] M. Moscovici, W. Chien, M. Abdelgawad, and Y. Sun. Electrical power free, low dead volume, pressure-driven pumping for microfluidic applications. *Biomicrofluidics*, 4(4):046501, 2010.

[58] X. Zhu, N. Phadke, J. Chang, B. Cho, D. Huh, and S. Takayama. Gravity-Driven Micropump with a Steady Flow Rate. In *Micro Total Analysis Systems 2002*, pages 151–153. Springer Netherlands, 2002.

[59] X. Wang, C. Cheng, S. Wang, and S. Liu. Electroosmotic pumps and their applications in microfluidic systems. *Microfluid Nanofluidics*, 6(2):145, 2009.

[60] V. Miralles, A. Huerre, F. Malloggi, and M.C. Jullien. A Review of Heating and Temperature Control in Microfluidic Systems: Techniques and Applications. *Diagnostics*, 3:33–67, 2013.

[61] R.M Guijt, A. Dodge, G.W. van Dedem, N.F. de Rooij, and E. Verpoorte. Chemical and physical processes for integrated temperature control in microfluidic devices. *Lab on a Chip*, 3(1):1–4, 2003.

[62] J.J. Shah, S.G. Sundaresan, J. Geist, D.R. Reyes, J.C. Booth, M.V Rao, and M. Gaitan. Microwave dielectric heating of fluids in an integrated microfluidic device. *Journal of Micromechanics and Microengineering*, 17:2224–2230, 2007.

[63] S.A. Silburn, C.D. Saunter, J.M. Girkin, and G.D. Love. Multidepth, multiparticle tracking for active microrheology using a smart camera. *Review of Scientific Instruments*, 82(3):033712, 2011.

[64] J. K. Wilmshurst and H. J. Bernstein. The Infrared and Raman Spectra of Toluene, Toluene-$\alpha$-$d_3$, m-Xylene, and m-Xylene-$\alpha\alpha$-$d_6$. *Canadian Journal of Chemistry*, 35(8):911–925, 1957.

[65] X. Xu. Stimulated Raman spectrum threshold in poly(methyl methacrylate) optical fibers. *Optics Communications*, 199:89–93, 2001.

[66] G.E. Walrafen and E. Pugh. Raman Combinations and Stretching Overtones from Water, Heavy Water, and NaCl in Water at Shifts to ca. 7000 $cm^{-1}$. *Journal of Solution Chemistry*, 33(1):81–97, 2003.

[67] F.L. Galeener. Band limits and the vibrational spectra of tetrahedral glasses. *Physical Review B*, 19(8):4292–4297, 1979.

[68] J. Zhao, H. Lui, D.I. McLean, and H. Zeng. Automated autofluorescence background subtraction algorithm for biomedical Raman spectroscopy. *Applied Spectroscopy*, 61(11):1225–1232, 2007.

[69] B.D. Beier and A.J. Berger. Method for automated background subtraction from Raman spectra containing known contaminants. *Analyst*, 134:1198–1202, 2009.

[70] P. Matousek, M. Towrie, A Stanley, and A.W. Parker. Efficient Rejection of Fluorescence from Raman Spectra Using Picosecond Kerr Gating. *Applied Spectroscopy*, 53(12):1485–1489, 1999.

[71] S.T. McCain, R.M. Willett, and D.J. Brady. Multi-excitation Raman spectroscopy technique for fluorescence rejection. *Optics Express*, 16(15):10975–10991, 2008.

[72] G. Rusciano, A.C. De Luca, A. Sasso, and G. Pesce. Enhancing Raman tweezers by phase-sensitive detection. *Analytical Chemistry*, 79(10):3708–3715, 2007.

[73] N. Néve, J.K. Lingwood, J. Zimmerman, S.S. Kohles, and D.C. Tretheway. The PIVOT: An Integrated Particle Image Velocimeter and Optical Tweezers Instrument for Microenvironment Investigations. *Measurement Science and Technology*, 19(9):095403, 2008.

[74] D.W. Allan. Statistics of atomic frequency standards. *Proceedings of the IEEE*, 54(2):221–230, 1966.

[75] L. Galleani and P. Tavella. Characterization of atomic clock anomalies in the dynamic Allan variance domain. In *European Frequency and Time Forum International Frequency Control Symposium (EFTF/IFC), 2013 Joint*, pages 645–648, 2013.

[76] S. Kunze, S. Wolf, and G. Rempe. Measurement of fast frequency fluctuations: Allan variance of a grating-stabilized diode laser. *Optics Communications*, 128:269–274, 1996.

[77] F. Czerwinski, A.C. Richardson, and L.B. Oddershede. Quantifying Noise in Optical Tweezers by Allan Variance. *Optics Express*, 17(15):13255–13269, 2009.

[78] M. Andersson, F. Czerwinski, and L.B. Oddershede. Optimizing active and passive calibration of optical tweezers. *Journal of Optics*, 13(4):044020–6, 2011.

[79] G.M. Gibson, J. Leach, S. Keen, A.J. Wright, and M.J. Padgett. Measuring the accuracy of particle position and force in optical tweezers using high-speed video microscopy. *Optics Express*, 16(19):405–412, 2008.

[80] A. Einstein. *Investigations of the Theory of Brownian Movement*. Dover, 1956.

[81] A. Melling. Tracer particles and seeding for particle image velocimetry. *Measurement Science and Technology*, 8(12):1406, 1997.

[82] J. Huisken, J. Swoger, F. Del Bene, J. Wittbrodt, and E.H.K. Stelzer. Optical Sectioning Deep Inside Live Embryos by Selective Plane Illumination Microscopy. *Science*, 305(5686):1007–1009, 2004.

[83] J. Mathieu and J. Scott', editors. *An Introduction to Turbulent Flow*. Cambridge University Press, 2000.

[84] J. Leach, H. Mushfique, S. Keen, R. Di Leonardo, G. Ruocco, J.M Cooper, and M.J. Padgett. Comparison of Faxen's correction for a microsphere translating or rotating near a surface. *Physical Review E*, 79:026301, 2009.

[85] N.N. de Mevergnies. *The MicroPIVOT : an Integrated Particle Image Velocimeter and Optical Tweezers Instrument for Microscale Investigations*. PhD thesis, Portland State University, 2010.

[86] A.F. Chrimes. Microfluidics and Raman microscopy: current applications and future challenges. *Chemical Society Review*, 42:5880–5906, 2013.

[87] Y. Zhang, H. Hong, and W. Cai. Imaging with Raman spectroscopy. *Current Pharmaceutical Biotechnology*, 11(6):654–661, 2010.

[88] S. Park, N. Mohanty, J. W. Suk, A. Nagaraja, J. An, R. D. Piner, W. Cai, D. R. Dreyer, V. Berry, and R. S. Ruoff. Biocompatible, Robust Free-Standing Paper Composed of a TWEEN/Graphene Composite. *Advanced Materials*, 22:1–5, 2010.

[89] K. Berg-Sörensen, L. Oddershede, E. Florin, and H. Flyvbjerg. Unintended filtering in a typical photodiode detection system for optical tweezers. *Journal of Applied Physics*, 93(6):3167–3176, 2003.

[90] P. Bartlett, S.I. Henderson, and S.J. Mitchell. Measurement of the hydrodynamic forces between two polymer-coated spheres. *Philosophical Transactions of the Royal Society A*, 359:883–895, 2001.

[91] A. van der Horst and N.R. Forder. Power spectral analysis for optical trap stiffness calibration from high-speed camera position detection with limited bandwidth. *Optical Society of America*, 18(8):7670–7677, 2010.

[92] W.P. Wong and K. Halvorsen. The effect of integration time on fluctuation measurements: calibrating an optical trap in the presence of motion blur. *Optics Express*, 14(25):12517–12531, 2006.

[93] P.F. Lawton, J.M. Girkin, and C.D. Saunter. Combining optical trapping in a microfluidic channel with simultaneous micro-Raman spectroscopy and motion detection. In *Proc. SPIE*, page 89760V, 2014.

[94] E. Kiskinis, W. Suter, and A. Hartmann. High throughput Comet assay using 96-well plates. *Mutagenesis*, 17(1):37–43, 2002.

[95] W.C. Lee and B.E. Khoo. Forensic Light Sources for Detection of Biological Evidences in Crime Scene Investigation: A Review. *Malaysian Journal of Forensic Sciences*, 1:17–27, 2010.

[96] M.A. Turk and A.P. Pentland. Face recognition using eigenfaces. In *Computer Vision and Pattern Recognition, 1991. Proceedings CVPR '91., IEEE Computer Society Conference on*, pages 586–591, 1991.

[97] C. Rodarmel and J. Shan. Principal Component Analysis for Hyperspectral Image Classification. *Surveying and Land Information Systems*, 62(2):115–123, 2002.

[98] I.T. Joliffe. *Principal Component Analysis*. Springer, 2002.

[99] S. Lê, J. Josse, and F. Husson. FactoMineR: An R Package for Multivariate Analysis. *Journal of Statistical Software*, 25(1):1–18, 2008.

[100] Private Communication with Proctor and Gamble Hair dye department, Frankfurt. May 2014.

[101] T. Clausen, A. Schwan-Jonczyk, G. Lang, W. Schuh, K.D. Liebscher, C. Springob, M. Franzke, W. Balzer, S. Imhoff, G. Maresch, and R. Bimczok. *Hair Preparations*. Wiley-VCH Verlag GmbH and Co. KGaA, 2000.

[102] U. Kubitscheck, editor. *Fluorescence Microscopy: From Principles to Biological Applications*. Wiley-Blackwell, 2013.

[103] E.J. Botcherby, R. Juškaitis, M.J. Booth, and T. Wilson. Aberration-free optical refocusing in high numerical aperture microscopy. *Optics Letters*, 32(14):2007–2009, 2007.

[104] A. Curran, S. Tuohy, D.G.A.L. Aarts, M. Booth, T. Wilson, and R.P.A. Dullens. 3D imaging and optical manipulation through a single objective. Presentation at Photon 14 Conference, London, September 2014.

# Appendix A

# Equipment specifications

## A.1 Spectral response of the LUPA 300 camera sensor

Figure A.1 shows the response of the CMOS smart camera sensor at wavelengths from 400-1000 nm. The LED used in the experiment was chosen to have a wavelength lower than the Raman excitation beam (peak at 450nm), so simultaneous Raman tweezing and imaging could take place; however the camera is only running at half efficiency, so it is important to use a bright light source. Longer wavelengths were not chosen as these are harder to filter from the Raman signal; the use of a Raman edge filter was found to remove most if not all of the blue light from the Raman spectrum.